Spring 2020

An Asymptotic Self-Sustaining Process Theory for Uniform Momentum Zones and Internal Interfaces in Unbounded Couette Flow

Brandon Montemuro
University of New Hampshire, Durham

AN ASYMPTOTIC SELF-SUSTAINING PROCESS THEORY FOR UNIFORM MOMENTUM ZONES AND INTERNAL INTERFACES IN UNBOUNDED COUETTE FLOW

BY

BRANDON MONTEMURO

BS, Aerospace Engineering, Pennsylvania State University, Pennsylvania , 2010

DISSERTATION

Submitted to the University of New Hampshire
in Partial Fulfillment of
the Requirements for the Degree of

Doctor of Philosophy

in

Applied Mathematics

May 2020

This dissertation has been examined and approved in partial fulfillment of the requirements for the degree of Doctor of Philosophy in Applied Mathematics by:

Dissertation Director, Gregory P. Chini,
Professor of Mechanical Engineering

Christopher White,
Associate Professor of Mechanical Engineering

John Gibson,
Associate Professor of Mathematics & Statistics

Joseph Klewicki,
Professor of Mechanical Engineering, University of Melbourne

Beverley McKeon,
Professor of Aeronautics, California Institute of Technology

Date: July 24, 2019

Original approval signatures are on file with the University of New Hampshire Graduate School.

This work is dedicated to my family and friends.

ACKNOWLEDGMENTS

I would like to thank my advisor Dr. Greg Chini who helped guide me through graduate school and the past six years of my academic career. His patience and support have been instrumental in the scope and quality of the research culminating in the writing of this dissertation. His guidance and notes while I taught Thermodynamics were much appreciated.

Additionally, I want to thank my committee members, Beverley McKeon, Chris White, John Gibson, and Joe Klewicki, for their assistance and guidance throughout this process. Without Joe, I would not have come to the University of New Hampshire. Their helpful comments and suggestions on my dissertation are also greatly appreciated.

I also want to thank Scott and Gina for their technical support over the years. I additionally would like to thank Lauren and Tracy form the Mechanical Engineering department as well as Jan and Jennifer from the Mathematics department for their assistance, and Sheri Millette who helped with some payment snafus over the years.

A huge thank you to the members of my family, who supported me throughout this work. My cohort of graduate students in the IAM Program and Mechanical Engineering Department who provided suggestions in research and pushed me along were crucial to getting through. Additionally, many thanks to all the members of the numerous intramural teams, hiking trips, and ski trips that might have prolonged my time here but kept me sane.

Lastly, support from the UNH CEPS Fellowship, UNH Summer TA Fellowship, and National Science Foundation CBET grant 1437851 is gratefully acknowledged. Portions of this work have been published in the Philosophical Transactions of the Royal Society A (Chini *et al.*, 2017) and in a manuscript entitled 'A self-sustaining process theory for uniform momentum zones and internal shear layers in high Reynolds number shear flows' being considered for publication in the Journal of Fluid Mechanics.

TABLE OF CONTENTS

Page

ACKNOWLEDGMENTS . . . . . **v**

NOMENCLATURE . . . . . **viii**

LIST OF TABLES . . . . . **x**

LIST OF FIGURES . . . . . **xi**

ABSTRACT . . . . . **xvi**

CHAPTER

1. INTRODUCTION **1**

1.1 Background 1
1.2 Quasi-Coherent Structures in Turbulent Wall Flows 3
1.3 Modern Dynamical Systems View of Turbulent Wall Flows 6
1.4 Vortex-Wave Interaction Theory 7
1.5 Challenges and Objectives 10
1.6 Hypothesis 14
1.7 Summary 17

2. LARGE REYNOLDS NUMBER AND LARGE WAVENUMBER ASYMPTOTIC ANALYSIS **20**

2.1 Introduction 20
2.2 Uniform Momentum Zones 22
2.3 Vortical Fissures 27

2.3.1 Viscous Mean Dynamics: Childress Cell Problem 29
2.3.2 Inviscid Fluctuation Dynamics: Rayleigh, Eikonal and Amplitude Equations 33

2.4 Critical Layers 42

2.4.1 Mean Equations 42

2.4.2 Fluctuation Equations 44

2.5 Roll-Flow Energy Budget 49
2.6 Summary 54

3. NUMERICAL METHODS 59

3.1 Introduction 59
3.2 Uniform Momentum Zones 59
3.3 Vortical Fissures 62

3.3.1 Mean Fields 63
3.3.2 Fluctuation Fields 64
3.3.3 Caustics 68

3.4 Critical Layers 68
3.5 Roll-Flow Energy Budget 68
3.6 Summary 69

4. RESULTS 72

4.1 Introduction 72
4.2 Numerical Reconstruction of ECS 73

4.2.1 Uniform Momentum Zones 74
4.2.2 Vortical Fissures 75

4.3 Parameter Study 76
4.4 Upper and Lower Branch States 79
4.5 Summary 82

5. CONCLUSIONS AND FUTURE WORK 83

BIBLIOGRAPHY 89

APPENDICES

A. SCALING OF FISSURE THICKNESS 93
B. FREDHOLM ALTERNATIVE 94
C. SIMPLIFICATION OF COEFFICIENTS IN AMPLITUDE EQUATION 95
D. CAUSTICS 100
E. CONVOLUTION 107
F. ECS SOLUTION ALGORITHM 108
G. TABLE OF ACRONYMS 109

NOMENCLATURE

α	True streamwise wavenumber
$\breve{\alpha}$	$O(1)$ True streamwise wavenumber
$\tilde{\alpha}$	$O(1)$ Streamwise wavenumber scaled by $\overline{\Omega}_c$
$\tilde{\beta}$	$O(1)$ Spanwise wavenumber scaled by $\overline{\Omega}_c$
$\overline{\Omega}_c$	$O(1)$ Homogenized value of x-mean vorticity
Δ	Width of internal shear layer
$\tilde{\Delta}$	Width of internal shear layer scaled by $\overline{\Omega}_c$
δ	Width of critical layer
$\tilde{\delta}$	Width of critical layer scaled by $\overline{\Omega}_c$
L_z	Roll-cell width
y	UMZ wall–normal coordinate
$\mathcal{Y}$	Rescaled wall–normal coordinate within vortical fissure
Y	Rescaled wall–normal coordinate within critical layer
$\overline{u}$	Mean streamwise velocity in uniform momentum zone
$\overline{\mathcal{U}}$	Mean streamwise velocity in vortical fissure
$\mathcal{U}'$	Fluctuating streamwise velocity in vortical fissure
$\mathcal{U}'_r$	Rotated streamwise velocity fluctuation in vortical fissures following Squire's transformation
$\overline{U}$	Mean streamwise velocity in critical layer
U'	Fluctuating streamwise velocity in critical layer
$\overline{v}$	Mean wall–normal velocity in uniform momentum zone
$\tilde{v}$	Mean wall–normal velocity in uniform momentum zone scaled by $\overline{\Omega}_c$

$\overline{\mathcal{V}}$	Mean wall–normal velocity in vortical fissure
$\tilde{\mathcal{V}}$	Mean wall–normal velocity in vortical fissure scaled by $\overline{\Omega}_c$
$\mathcal{V}'$	Fluctuating wall–normal velocity in vortical fissure
$\overline{V}$	Mean wall–normal velocity in critical layer
$\tilde{V}$	Mean wall–normal velocity in critical layer scaled by $\overline{\Omega}_c$
V'	Fluctuating wall–normal velocity in critical layer
$\overline{w}$	Mean spanwise velocity in uniform momentum zone
$\tilde{w}$	Mean spanwise velocity in uniform momentum zone scaled by $\overline{\Omega}_c$
$\overline{\mathcal{W}}$	Mean spanwise velocity in vortical fissure
$\tilde{\mathcal{W}}$	Mean spanwise velocity in vortical fissure scaled by $\overline{\Omega}_c$
$\mathcal{W}'$	Fluctuating spanwise velocity in vortical fissure
$\mathcal{W}'_r$	Rotated spanwise velocity fluctuation in vortical fissure following Squire's transformation
$\overline{W}$	Mean spanwise velocity in critical layer
$\tilde{W}$	Mean spanwise velocity in critical layer scaled by $\overline{\Omega}_c$
W'	Fluctuating spanwise velocity in critical layer
$\overline{p}$	Mean pressure in uniform momentum zone
$\tilde{p}$	Mean pressure in uniform momentum zone scaled by $\overline{\Omega}_c^2$
$\overline{\mathcal{P}}$	Mean pressure in vortical fissure
$\tilde{\mathcal{P}}$	Mean pressure in vortical fissure scaled by $\overline{\Omega}_c^2$
$\mathcal{P}'$	Fluctuating pressure in vortical fissure
Π'	Fluctuating pressure in vortical fissure following Squire's transformation
$\overline{P}$	Mean pressure in critical layer
$\tilde{P}$	Mean pressure in critical layer scaled by $\overline{\Omega}_c^2$
P'	Fluctuating pressure in critical layer

LIST OF TABLES

Table **Page**

1.1 Magnitude ordering and scaling behaviors associated with the four-layer structure of the mean momentum equation for turbulent channel flow. Note that the layer IV properties are asymptotically attained as $Re_\tau \to \infty$. PG: mean pressure gradient, TI: Turbulent inertia, and MV: mean viscous force. (Adapted from Klewicki (2013*b*).) 11

2.1 Summary of the scalings of the mean and fluctuation fields and the dominant terms arising in the relevant force balances in each of the three subdomains: UMZ = uniform momentum zone; VF = vortical fissure (internal shear layer); and CL = critical layer. ECS component: S = streak; R = roll; and F = fluctuation. Forces: NI = nonlinear inertia; LI = linearized inertia; PG = pressure gradient; VNF = viscous normal force; and RSD = Reynolds stress divergence. As demonstrated by the analysis performed in chapter 2, the dimensionless VF thickness $\Delta = Re^{-1/4}$, while the CL thickness $\delta = Re^{-1/2}$. E.S.T. = exponentially small terms. 22

2.2 Summary of the scalings of the mean and fluctuation fields in each of the three fissure-normal subdomains: UMZ = Uniform Momentum Zone; VF = Vortical Fissure / Internal Shear Layer; and CL = Critical Layer. 56

3.1 Summary of the discretization used in the numerical solution of (3.5) for $\overline{u}_0(y, z)$ regularized by the inclusion of Laplacian diffusion $\tilde{\Delta} = O(10^{-4})$. 62

3.2 Summary of the discretization used for solving Rayleigh's (eigenvalue) stability equation within the VF domain. 63

LIST OF FIGURES

Figure **Page**

1.1 (a) Hydrogen-bubble flow visualization of streamwise velocity in a streamwise-spanwise (x–z) plane revealing near-wall streaks in a flat-plate turbulent boundary layer (Kline *et al.*, 1967). (b) Instantaneous streamwise velocity in an x–z plane from a direct numerical simulation (Pirozzoli & Bernardini, 2012) of a flat-plate turbulent boundary layer showing outer (inertial) region streaks. 3

1.2 Uniform momentum zones (UMZs) and internal shear layers (or *vortical fissures*, VFs) are ubiquitous in the inertial region of turbulent wall flows at sufficiently large values of the friction Reynolds number Re_τ. (a) Instantaneous (solid line) versus mean (dashed) streamwise velocity profiles taken from the boundary-layer measurements of de Silva *et al.* (2016) at $Re_\tau \approx 8000$ illustrating the staircase-like arrangement of UMZs and VFs. (b) Two-dimensional streamwise velocity contour with the solid black line representing the instantaneous profile shown in (a) (de Silva *et al.*, 2016). 5

1.3 Conditionally-averaged streamwise velocity (a) and its wall-normal derivative (b) through vortical fissures in the inertial region of a turbulent BL flow (at $Re_\tau \approx 6000$) in the UNH FPF. y_i indicates the wall-normal location of the VF; u_{core} is the streamwise velocity at the center of the VF; and angle brackets indicate a conditional average, where the conditioning is based on a spanwise vorticity threshold equal to $3\sqrt{Re_\tau}(u_\tau/h)$. The various distinct conditionally-averaged profiles are obtained by segregating the instantaneous profiles into 10 contiguous wall-normal bins (all located within the inertial domain) spanning the measurement field of view. 6

1.4 (a) Sketches of the rolls, streaks, and streak instabilities that drive the SSP. (b) Schematic depiction of the SSP feedback loop for a generic wall-bounded shear flow proposed by Waleffe (1995). Weak [$O(R^{-1})$, where here the Reynolds number $R \equiv U_0 H_0/\nu$ and U_0 and H_0 are characteristic velocity and length scales of the shear flow] streamwise rolls redistribute the imposed background shear creating $O(1)$ streaks. Strong spanwise inflectional instabilities lead to $O(R^{-1})$ streamwise-varying Rayleigh instability waves, which nonlinearly interact to sustain the $O(R^{-1})$ spanwise rolls. (Images from Waleffe (2005).) 8

1.5 Bifurcation diagram reproduced from Wang *et al.* (2007) depicting how various streamwise Fourier modes of the velocity field associated with the ECS designated 'EQ1' in plane Couette flow scale with Reynolds number. The different lines represent the $streak$: $\hat{u}_0 = O(1)$ in green; $roll$: ($\hat{v}_0$,$\hat{w}_0$) $= O(R^{-1})$ in blue; $fundamental\ x\ mode$: $\hat{\mathbf{u}}_1 = O(R^{-0.9})$ in red; and $higher\ x\ harmonics$: $\hat{\mathbf{u}}_n = o(R^{-1})$, $n > 1$ in magenta and tan. 9

1.6 Singular nature of the TBL. (a) Plot showing the ratio of the mean viscous force (MV) to turbulent inertia (TI), i.e. to the Reynolds stress gradient, in turbulent channel flow at four different values of Re_τ; data taken from the water channel experiments by Elsnab *et al.* (2017). The mean viscous force is significant in a volume-averaged sense only in a near-wall domain of size $O(\sqrt{Re_\tau})$ in viscous (or 'plus') units, corresponding to a domain of size $O(h/\sqrt{Re_\tau})$ in outer units. Outboard of the peak in the Reynolds stress (where the force ratio tends to plus or minus infinity), the volume-averaged mean viscous force is negligible. (b) Schematic illustrating the concentration of spanwise vorticity within VFs that, at large Re_τ, become increasingly widely separated with increasing distance from the wall. (Adapted from Klewicki (2013*a*,*b*).) The new SSP theory developed herein targets UMZs and VFs located in the inertial domain, as highlighted in blue and green, respectively. 12

1.7 Streamwise- and spanwise-averaged streamwise velocity for 'EQ2', an upper-branch equilibrium ECS in plane Couette flow, at two Reynolds numbers $Re = U_w h/\nu$, where U_w is the wall velocity, separated by a decade (at fixed domain size). Data courtesy of J. Gibson. 14

1.8 Proposed flow configuration in which sufficiently strong rolls in the y–z plane redistribute the imposed background shear in the streamwise velocity profile (here taken to be unbounded Couette flow) yielding the staircase-like UMZ/VF profile. 15

1.9 Schematic diagram of the hypothesized three-region asymptotic structure in the fissure-normal direction centred on a fissure located at $y = 0$ (cf. highlighted region in figure 1.6(b)) 16

1.10 Growth rate curves obtained from an Orr-Sommerfeld linear stability analysis using an error-function background streamwise velocity profile. Here, α is the streamwise wavenumber, σ is the real growth rate, and ε is a small parameter characterizing the thickness of the shear layer in the imposed background streamwise velocity profile. As expected for (largely) inviscid shear instabilities, α for both the fastest-growing and non-zero neutral mode increases as $\varepsilon \to 0$. 17

2.1 Schematic of UMZs and VFs spanning a TBL showing excised domain. (Adapted from Priyadarshana *et al.* (2007).) 21

2.2 Differential homogenization of a background Couette flow (a,b) by the stacked counter-rotating pattern of steady rolls (vector plot in (a), obtained from (2.11)–(2.12)) leading to the emergence of UMZs and an internal shear layer (b); i.e. an embedded VF. This process is realized only for sufficiently large values of the *effective* Reynolds number $\bar{a}Re$, where the roll amplitude $\bar{a}(Re) \to 0$ as $Re \to \infty$. For example, in the Fourier–Chebyshev pseudospectral computations used to generate these results, $\bar{a}Re \approx 10^4$. 23

2.3 Dimensionless VF thickness as a function of Re calculated from the steady-state numerical solution of the advection–diffusion equation (2.2) for $\overline{u}(y, z, T)$, regularized by the inclusion of Laplacian diffusion $(\bar{a}Re)^{-1}\nabla_\perp^2 \overline{u}$ on the right hand side, for $L_z = 2$. 24

2.4 Formulation of Childress cell problem, as adapted from Chini & Cox (2009). (a) Contour plot of $\overline{u}_0(y, z)$. (b) Corresponding multi-region asymptotic structure of a steady roll cell as $Re \to \infty$. The white region is the dynamically inviscid vortex core. The light grey regions indicate the $O(\Delta)$ thick VFs as well as $O(\Delta)$ thick positive and negative streamwise jets. The streamwise-averaged streamwise velocity is passively advected through the outer corner regions also indicated by the light grey shading. (The viscous inner corner regions highlighted in dark grey also are dynamically passive.) ζ is a stretched arc-length coordinate running around the cell perimeter, and η is a scaled coordinate measuring distance normal to the VFs and jets. 31

2.5 The real (Re) and imaginary (Im) parts of the function Yi(s) for real s. (Adapted from Balmforth *et al.* (1997).) 46

2.6 Schematic diagram of a mechanistic self-sustaining process for UMZs and VFs in the inertial domain of turbulent wall flows. The feedback loop shown indicates that rolls having $O(Re^{-1/2})$ circulation strength redistribute the background shear flow to induce an $O(1)$ inflected streamwise flow. The counter-rotating and stacked rolls are sufficiently strong to differentially homogenize the background flow, thereby creating and maintaining both UMZs and internal shear layers (VFs). The wall-normal (y) inflections in the streamwise-mean streamwise velocity support an $O(Re^{-3/4})$ Rayleigh (inviscid shear) instability mode that has a streamwise (x) wavelength $2\pi/\alpha \ll 1$ that is commensurate with the VF thickness. Consequently, the Rayleigh mode is confined to the VF, where it is refracted and rendered three-dimensional by the comparably slow spanwise variation in the fissure thickness, and the resulting ECS are inherently multiscale. The 3D Rayleigh mode suffers a critical-layer singularity, causing the magnitude of the x-varying spanwise velocity component to be amplified to $O(Re^{-1/2})$. The resulting nonlinear self-interaction of the Rayleigh mode within the CL drives the roll motions in the UMZs through a modulational (i.e. slow spanwise) Reynolds stress divergence involving this velocity component. 55

3.1 Schematic demonstrating how homogeneous Dirichlet boundary conditions are implemented in a Chebyshev discretization method, resulting in the zeroing of certain rows and columns (adapted from Trefethen (2000)). 61

3.2 Normalized streak-induced shear $\tilde{\lambda}(z) \equiv \partial_y \overline{\mathcal{U}}_0(0, z)$ at the mid-plane of the VF obtained from the solution of the Childress cell problem (i.e. in the limit $Re \to \infty$, solid curve) and from the numerical solution of the full advection–diffusion equation (2.19) [or, equivalently, (3.5)] for finite Re (dotted curve). 64

4.1 3D numerical reconstruction of inertial layer ECS supporting VFs coupled to adjacent UMZs. Input parameters are $\mathcal{A} = 5$, $\breve{\alpha} = 0.576$ and $L_z = 2$. ($Re = 1.36 \times 10^7$ for computation of the streak velocity field.) Color indicates the streamwise-averaged streamwise flow speed in the y–z and x–y planes and the fissure-normal fluctuation velocity, scaled by $O(\Delta^3)$, in the exposed x–z plane. Arrows show in-plane velocity vectors. 73

4.2 Reconstruction of inertial ECS exhibiting VFs coupled to adjacent UMZs in unbounded plane Couette flow: Mean velocity field in the fissure-normal/spanwise-plane. Color indicates the value of the streamwise-averaged streamwise velocity component while arrows show the roll velocity field. Parameter values are given in the figure 4.1 caption. 74

4.3 Reconstruction of inertial ECS exhibiting VFs coupled to adjacent UMZs in unbounded plane Couette flow: Fissure-normal fluctuation velocity component in a streamwise/spanwise plane within the VF near $y = 0$. Color indicates the value of this component normalized by Δ^3. The solid black lines indicate caustics, which partition the plane into an illuminated region ($-0.75 \lesssim z \lesssim 0.75$) and shadow zones ($|z| \gtrsim 0.75$). Parameter values are given in the figure 4.1 caption. 75

4.4 (a) Streamlines within the VF associated with an inertial-ECS solution computed for $\mathcal{A} = 5$, $\breve{\alpha} = 0.576$ and $L_z = 2$ (with $Re = 1.36\text{x}10^7$) showing a fine-scale Kelvin's cat's-eyes vortex pattern in the streamwise/wall-normal plane $z = -0.6738$ on which the spanwise fluctuation velocity vanishes. (b) Schematic taken from Adrian *et al.* (2000) showing fine-scale hairpin and 'cane' vortices (in yellow) separating boluses of large-scale streamwise flow having quasi-uniform momentum (in grey). 76

4.5 The homogenized value of the roll vorticty $\overline{\Omega}_c$ normalized by $\mathcal{A}^{6/7}$ versus the true streamwise wavenumber normalized by $\mathcal{A}^{3/14}$ for $L_z = 2$. The different curves correspond to different values of $\mathcal{A}$. 77

4.6 The homogenized value of the roll vorticty $\overline{\Omega}_c$ normalized by $\mathcal{A}^{6/7}$ versus the roll wavelength L_z. In (a), the different curves correspond to different constant values of the input wavenumber $\tilde{\alpha}$, while in (b), the various curves indicate different constant values of the 'true' streamwise wavenumber $\breve{\alpha}$. 78

4.7 The homogenized value of the roll vorticty $\overline{\Omega}_c$ normalized by $\mathcal{A}^{6/7}$ (a) plotted versus the input wavenumber $\tilde{\alpha}$, where the different curves correspond to different constant values of the roll wavelength L_z, and (b) plotted versus the 'true' streamwise wavenumber $\breve{\alpha}$ normalized by $\mathcal{A}^{3/14}$, where the different curves again correspond to different constant values of the roll wavelength L_z. 79

4.8 The input streamwise wavenumber $\tilde{\alpha}$ plotted versus the 'true' streamwise wavenumber $\breve{\alpha}$ to demonstrate the nonlinear relationship between them that yields upper and lower branch inertial ECS. The different curves correspond to different values of the roll wavelength. 80

4.9 Fissure-normal fluctuation velocity in an x–z plane near the CL for a lower-branch ECS computed at $\mathcal{A} = 1$, $L_z = \pi/5$, and $\tilde{\alpha} = 1.02$. Colors indicate velocities normalized by $\tilde{\Delta}^3$. $Re = 10^{11}$: top; $Re = 10^{13}$: middle; $Re = 10^{15}$: bottom. 81

5.1 Schematic diagram of a mechanistic self-sustaining process for UMZs and VFs in the inertial domain of turbulent wall flows. The feedback loop shown in (a) indicates that rolls having $O(Re^{-1/2})$ circulation strength redistribute the background shear flow to induce $O(1)$ streamwise streaks. As depicted in (b), the counter-rotating and stacked rolls are sufficiently strong to differentially homogenize the background flow, thereby creating and maintaining both UMZs (highlighted in yellow) and internal shear layers (VFs, indicated in blue). The wall-normal (y) inflections in the streak velocity support an $O(Re^{-3/4})$ Rayleigh (inviscid shear) instability mode that has a streamwise (x) wavelength $2\pi/\alpha \ll 1$ that is commensurate with the VF thickness. Consequently, the Rayleigh mode is confined to the VF, where it is refracted and rendered three-dimensional by the comparably slow spanwise variation in the fissure thickness (not depicted), and the resulting ECS are inherently multiscale. The 3D Rayleigh mode suffers a critical-layer singularity, causing the magnitude of the x-varying spanwise velocity component to be amplified to $O(Re^{-1/2})$. The resulting nonlinear self-interaction of the Rayleigh mode within the CL drives the roll motions in the UMZs through a modulational (i.e. slow spanwise) Reynolds stress divergence involving this velocity component. 84

ABSTRACT

An Asymptotic Self-Sustaining Process Theory for Uniform Momentum Zones and Internal Interfaces in Unbounded Couette Flow

by

Brandon Montemuro

University of New Hampshire, May, 2020

Meinhart & Adrian (Phys. Fluids, vol. 7, 1995, p 694) were the first investigators to document that the wall-normal (y) structure of the instantaneous streamwise velocity in the turbulent boundary layer exhibits a staircase-like profile: regions of quasi-uniform momentum are separated by internal shear layers across which the streamwise velocity jumps by an O(1) amount when scaled by the friction velocity u_τ. This sharply-varying instantaneous profile differs dramatically from the well-known long-time mean profile, which is logarithmic over much of the boundary layer, and prompted Klewicki (Proc. IUTAM, vol. 9, 2013, p. 69–78) to propose that the turbulent boundary layer is singular in two distinct ways. Firstly, spanwise vorticity and mean viscous forces are concentrated in a near-wall region of thickness $O(h/\sqrt{Re_\tau})$, where Re_τ is the friction Reynolds number and h is the boundary-layer height. Secondly, in a turbulent boundary layer, spanwise vorticity and viscous forces are also significant away from the wall (outboard of the peak in the Reynolds stress), but *only* in spatially-localized regions, i.e. within the internal shear layers. This interpretation accords with Klewicki's multiscale similarity analysis of the mean momentum balance for turbulent wall flows (J. Fluid Mech., vol. 522, 2005, pp. 303–327). The objective of the present investigation is to probe the governing Navier–Stokes equations in the limit of large Re_τ in search of a mechanistic self-sustaining process (SSP) that (i) can account for the emergent staircase-like profile of streamwise velocity in the inertial region and (ii) is compatible with the singular nature of turbulent wall flows.

Plausible explanations for the formation and persistence of sharply-varying instantaneous streamwise velocity profiles all implicate quasi-coherent turbulent flow structures including streamwise roll motions that induce a cellular flow in the transverse (i.e. spanwise/wall-normal) plane. One

proposal is that the large-scale structures result from the spontaneous concatenation of smaller–scale structures, particularly hairpin and cane vortices and vortex packets. A competing possibility, explored here, is that these large–scale motions may be *directly* sustained via an inertial–layer SSP that is broadly similar to the near-wall SSP.

The SSP theory derived in this investigation is related to the SSP framework developed by Waleffe (Stud. Appl. Math, vol. 95, 1995, p. 319) and, especially, to the closely-related vortex-wave interaction (VWI) theory derived by Hall & Smith (J. Fluid Mech., vol. 227, 1991, pp. 641–666) and Hall & Sherwin (J. Fluid Mech., vol. 661, 2010, pp. 178–205) in that a rational asymptotic analysis of the instantaneous Navier–Stokes equations is performed. Nevertheless, in this dissertation, it is argued that these theories cannot account for organized motions in the inertial domain, essentially because the roll motions are predicted to be viscously dominated even at large Re_τ. The target of the present investigation is an inherently multiscale SSP, in which inviscid streamwise rolls differentially homogenize an imposed background shear flow, thereby generating uniform momentum zones and an embedded internal shear layer (or interface), and are sustained by Rayleigh instability modes having asymptotically smaller streamwise and spanwise length scales. The Rayleigh mode is supported by the inflectional wall-normal profile of the streamwise–averaged streamwise velocity. Because the thickness of the internal shear layer varies comparably slowly in the spanwise direction, the Rayleigh mode is refracted and rendered fully three–dimensional. This three–dimensional mode is singular, necessitating the introduction of a critical layer inside the shear layer within which the mode is viscously regularized. As in VWI theory, a jump in the spanwise Reynolds stress is induced across the critical layer, which ultimately drives the roll motions. This multiscale and three–region asymptotic structure is efficiently captured using a complement of matched asymptotic and WKBJ analysis. The resulting reduced equations require the numerical solution of both ordinary differential eigenvalue and partial differential boundary-value problems, for which pseudospectral and spectral collocation methods are employed. Crucially, in contrast to Waleffe's SSP and to VWI theory, the rolls are sufficiently strong to differentially homogenize the background shear flow, thereby providing a plausible mechanistic explanation for the formation and maintenance of both UMZs and interlaced internal shear layers.

CHAPTER 1

INTRODUCTION

1.1 Background

Improved understanding of the basic properties of fluid motion – that is, of fluid dynamics – is crucial for the advancement of science and of various technologies. Generically, fluid flows are categorized into two regimes. Of these, the laminar flow regime is by far the better understood: the fluid moves in an orderly pattern of layers, or lamina. Conversely, turbulent flows are defined by the seemingly chaotic motions of small volumes of fluid. Most engineered and naturally-occurring flows are, in fact, turbulent. Crucially, turbulent fluid motions can enhance mixing of heat, mass, and momentum by approximately a factor of 1000 relative to the mixing accomplished by the same flow were it to remain in the laminar regime. The enhanced mixing can be beneficial or detrimental depending upon the situation. In heat transfer applications (e.g., cooling a room), turbulence will drive far more rapid temperature changes than would be realized by thermal diffusion alone. In contrast, the undesirable increase in drag on airplane wings and in oil pipelines results from the increased turbulent mixing of the momentum of the air and oil, respectively. These latter flows are prime examples of turbulent wall flows, i.e., the turbulence that results from fluid flow past solid surfaces. Such flows are ubiquitous in both natural and engineered systems and therefore are of prime societal importance. Developing improved quantitative and physical understanding of wall turbulence is the overarching aim of this investigation.

Fluid turbulence frequently is described as the greatest unsolved problem of classical physics (Sreenivasan, 1999). Although the mathematical equations governing fluid motion were derived almost 200 years ago (in 1822), few analytical solutions to the resulting Navier-Stokes (NS) equations are known because the solutions can be chaotic; known analytic solutions correspond to

laminar flows. Consequently, fluid dynamicists often utilize a combination of laboratory experiments and computer simulations to study turbulent flows. Computer models of turbulent flows that faithfully replicate the detailed dynamics are referred to as direct numerical simulations (DNS). In DNS, the flow is discretized (i.e., divided) in space and time to enable numerical approximations to the solution of the governing partial differential (NS) equations; the finer the spatiotemporal discretization, the more accurate and reliably predictive the resulting numerical simulation, but also the greater the computational expense as measured in memory and time requirements. Although DNS has progressed to the point of being feasible for certain engineering applications, these 'brute-force' simulations of the NS equations would require years of computing time for the vast majority of turbulent flows in realistic parameter regimes (e.g., to simulate the airflow around a commercial airliner), even using the world's fastest and most powerful supercomputers (Davidson, 2004). Through the use of specially-designed facilities, such as the wind tunnel in the UNH Flow Physics Facility (FPF), laboratory experiments can be performed in more realistic parameter regimes. In isolation, however, these experiments lack the predictive capability that is crucial for advances in scientific understanding and engineering design.

Given the limitations of both DNS and experiments, systematically simplified (or 'reduced') mathematical models that retain a clear physical connection to the governing NS equations while simultaneously allowing for feasible computer simulations in realistic parameter regimes are desirable. Simplification is possible because experimental evidence suggests that, although chaotic, turbulent wall flows exhibit a certain level of spontaneous self-organization or flow structure. Indeed, the tendency of fluids to self-organize has captured the imagination of people throughout history. Scientists including Leonardo da Vinci took note of a fluid's ability to form coherent structures as early as the 1500s. Da Vinci made a sketch of water exiting from a square hole into a pool in which he depicted eddies (swirling motions) forming in the pool. This illustration is one of the earliest known examples of flow visualization as a scientific tool. Moreover, in his notes on this sketch, da Vinci describes a 'principal current' and another of 'random and reverse motion' (Gad-El-Hak, 1998), reminiscent of the notion of a Reynolds decomposition.

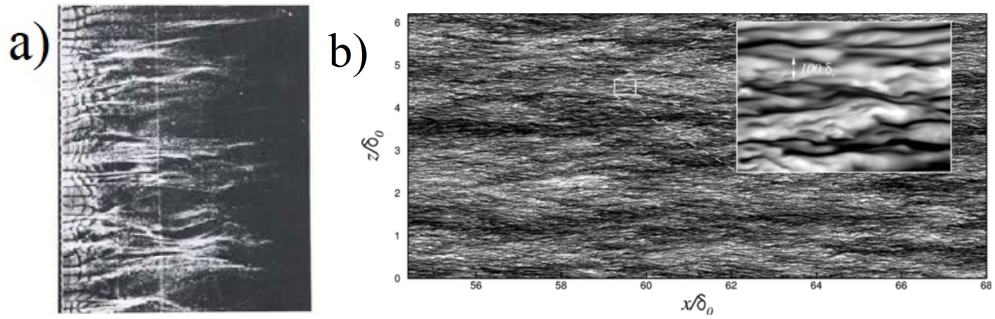

Figure 1.1: (a) Hydrogen-bubble flow visualization of streamwise velocity in a streamwise-spanwise (x–z) plane revealing near-wall streaks in a flat-plate turbulent boundary layer (Kline *et al.*, 1967). (b) Instantaneous streamwise velocity in an x–z plane from a direct numerical simulation (Pirozzoli & Bernardini, 2012) of a flat-plate turbulent boundary layer showing outer (inertial) region streaks.

1.2 Quasi-Coherent Structures in Turbulent Wall Flows

Quasi-coherent flow structures in the form of space-filling streamwise vortices and streaks (figure 1.1a) have long been observed in the near-wall region of turbulent wall flows in both laboratory experiments (Kline *et al.*, 1967) and DNS (Jiménez & Moin, 1991). These observations prompted mathematical and computational studies to explain their existence and persistence in flows in which the structures are not directly forced [Nagata (1990), Waleffe (1997), Hall & Smith (1991), Hall & Sherwin (2010), Beaume *et al.* (2015), Schoppa & Hussain (2002), Farrell & Ioannou (2012)]. Indeed, in the near-wall region (i.e., wallward of the peak in the turbulent Reynolds stress, corresponding to layers II and III of the four-layer flow regime described in table 1.1 (Klewicki, 2013*b*)), the interaction among viscous streamwise streaks and rolls has been shown to give rise to a self-sustaining process (SSP) capable of maintaining the turbulence on scales of $O(100)$ viscous units ν/u_τ, where ν is the kinematic viscosity and u_τ is the wall friction velocity (Hamilton *et al.*, 1995). At sufficiently large (friction) Reynolds number $Re_\tau \equiv u_\tau h/\nu$, where h is an appropriate outer length scale, quasi-coherent structures also have been observed in the inertial region (i.e., beyond the Reynolds stress peak, corresponding to layer IV in table 1.1) of the boundary layer. These outer-region structures, including large-scale motions (LSMs), very large-scale motions (VLSMs),

and superstructures (Hwang & Bengana, 2016), have been investigated using both laboratory experiments and DNS. In addition, they have length scales much larger than 100 viscous units and penetrate into or exist wholly within the inertial region (i.e., layer IV). Certain superstructures have been shown to extend for roughly $5-15h$ in the streamwise (henceforth, the x) direction (Hutchins & Marusic, 2007). Turbulent superstructures are significant physically because they carry a major fraction of the total turbulent kinetic energy of the flow. Moreover, these inertial-layer flow structures have been shown to leave a footprint on the near-wall structures, as shown in figure 1.1b [Hwang *et al.* (2016), Pirozzoli & Bernardini (2012)]. Despite their probable physical importance to turbulent dynamics, the origin of these inertial layer structures is not clearly understood. For example, it has been argued that LSMs and VLSMs arise from the spontaneous organization of attached and/or detached hairpin and cane vortices and hairpin and cane vortex packets (Adrian *et al.*, 2000). In this dissertation, however, a complementary thesis is investigated; namely, that the large-scale flow structures can be *directly* driven.

Meinhart & Adrian (1995) were the first investigators to document that the wall-normal (y) structure of the instantaneous streamwise velocity in the turbulent boundary layer (TBL) exhibits a staircase-like profile: zones of quasi-uniform momentum (UMZs) are separated by internal shear layers across which the streamwise velocity jumps by an $O(1)$ amount when scaled by u_τ (see figures 1.2 and 1.3). In the literature, these internal shear layers are sometimes referred to as *vortical fissures* (VFs). Recent investigations [Eisma *et al.* (2015), de Silva *et al.* (2016)] have confirmed and extended our understanding of the UMZ/VF structure. For example, de Silva *et al.* (2016) have shown that the number of UMZs (and VFs) increases logarithmically with increasing Reynolds number. Klewicki (2013*a*,*b*) has proposed a kinematic description of the spanwise (z) vorticity associated with this staircase UMZ/VF structure that is consistent both with the mean momentum equation and with the intriguing notion that the TBL comprises logarithmically many internal layers. Klewicki argues that the TBL is singular in two ways:

1) Like the singularity of a laminar boundary layer, near the wall there exists large spanwise vorticity and significant mean viscous forces;

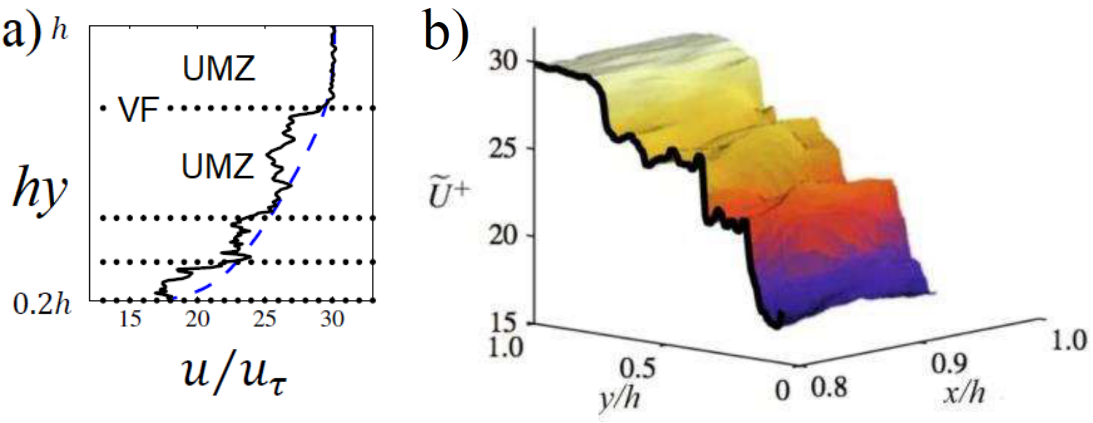

Figure 1.2: Uniform momentum zones (UMZs) and internal shear layers (or *vortical fissures*, VFs) are ubiquitous in the inertial region of turbulent wall flows at sufficiently large values of the friction Reynolds number Re_τ. (a) Instantaneous (solid line) versus mean (dashed) streamwise velocity profiles taken from the boundary-layer measurements of de Silva *et al.* (2016) at $Re_\tau \approx 8000$ illustrating the staircase-like arrangement of UMZs and VFs. (b) Two-dimensional streamwise velocity contour with the solid black line representing the instantaneous profile shown in (a) (de Silva *et al.*, 2016).

2) Unlike laminar BLs, there exists significant spanwise vorticity and viscous forces but only within thin spatially-segregated internal layers (VFs).

This singular behavior suggests the paradigm that there are logarithmically many viscous (if not laminar) 'boundary layers' within *the* TBL. In support of this notion, Bautista *et al.* (2019) demonstrate that the logarithmic profile and other, higher-order statistical features associated with the mean streamwise flow can be recovered by ensemble averaging staircase-like streamwise velocity profiles. A master staircase-like profile of the instantaneous streamwise velocity is constructed by incorporating VFs and UMZs with the wall-normal locations of the VFs and the associated increments in the streamwise flow speed specified in accord with the similarity reduction of the mean momentum equation performed by Klewicki and collaborators (Wei *et al.*, 2005). The fissures are then randomly displaced and the resulting profiles ensemble averaged over sufficiently many realizations. The recovered turbulent statistics agree remarkably well with those acquired from DNS of turbulent channel flow at large Re_τ, supporting the 'boundary layers within *the* boundary layer' paradigm. Given the likely fundamental dynamical role played by UMZ/VF structures in the

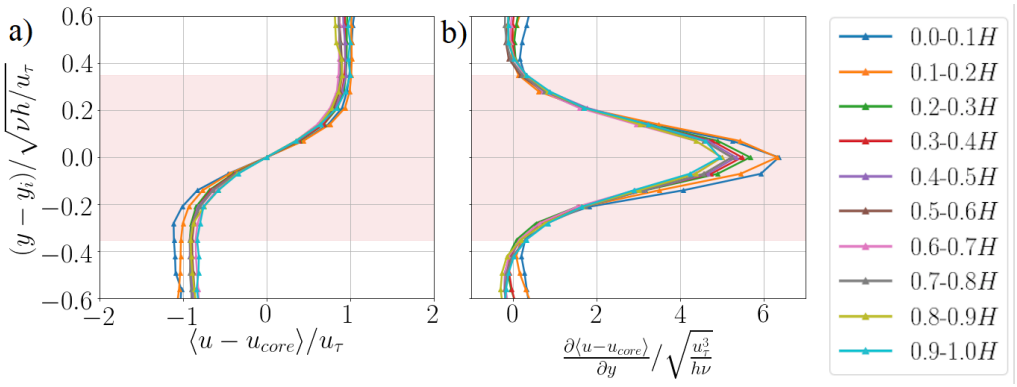

Figure 1.3: Conditionally-averaged streamwise velocity (a) and its wall-normal derivative (b) through vortical fissures in the inertial region of a turbulent BL flow (at $Re_\tau \approx 6000$) in the UNH FPF. y_i indicates the wall-normal location of the VF; u_{core} is the streamwise velocity at the center of the VF; and angle brackets indicate a conditional average, where the conditioning is based on a spanwise vorticity threshold equal to $3\sqrt{Re_\tau}(u_\tau/h)$. The various distinct conditionally-averaged profiles are obtained by segregating the instantaneous profiles into 10 contiguous wall-normal bins (all located within the inertial domain) spanning the measurement field of view.

inertial region of turbulent wall flows, a theoretical study of an idealized (uniformly-distributed) arrangement of VFs and UMZs is described in chapter 2.

1.3 Modern Dynamical Systems View of Turbulent Wall Flows

The structural, rather than statistical, analysis of turbulence has been given a firm mathematical basis via modern dynamical systems theory. Motivated by the spontaneous emergence of quasi-coherent near-wall flow features, Aubry *et al.* (1988) developed low-dimensional dynamical systems models of the turbulent boundary layer using proper orthogonal decomposition (POD) to identify the most energetic structures. Following the identification of these structures, Galerkin projection of the NS equations was employed to derive the equations of motion for the modal amplitudes. The resulting models qualitatively reproduced important dynamical features of the boundary layer. Instead of seeking a low-dimensional reduction of the NS equations, Gibson *et al.* (2008) extracted invariant solutions from fully-resolved numerical discretizations of the NS equations, in essence treating DNS as a faithful, very-high dimensional dynamical-systems representation of the governing partial differential equations. Although generally dynamically unstable,

these three-dimensional (3D) *exact coherent states* (ECS) are reminiscent of observed coherent flow structures and are believed to provide a scaffold in phase space for the turbulent dynamics. Gibson (2014) has compiled a database of invariant solutions for plane Couette flow for a range of Reynolds numbers and domain sizes.

The aim of the present investigation is to propose a mechanistic explanation for the emergence of UMZs and VFs by deriving directly from the governing Navier–Stokes equations a new, multi-scale self-sustaining process that supports ECS exhibiting these two flow features. To date, there are arguably two distinct first-principles SSP theories that can account for ECS in constant-density wall-bounded parallel shear flows. Most germane to the present investigation is the classical self-sustaining process theory introduced by Waleffe (1997) and the closely related asymptotic vortex–wave interaction (VWI) formalism developed earlier by Hall & Smith (1991) and subsequently applied to ECS in wall-bounded shear flows by Hall & Sherwin (2010). In both Waleffe's SSP and in VWI (the latter may be viewed as the infinite Reynolds number limit of the former), the nonlinear self-interaction of a streamwise-varying instability 'wave' drives the roll motions that advect the base shear flow to generate streaks. Since the streak profile is inflectional, an inviscid Rayleigh instability mode is excited. Thus, SSP theory provides a mechanistic approach for understanding the creation and persistence of coherent structures. This approach, introduced by Waleffe, is illustrated by the feedback loop shown in figure 1.4.

1.4 Vortex-Wave Interaction Theory

As the Reynolds number is increased at fixed domain size, many ECS develop a well-defined asymptotic structure. Figure 1.5, reproduced from Wang *et al.* (2007), shows how the various streamwise Fourier modes comprising the velocity field associated with the exact solution of the NS equations designated 'EQ1' in plane Couette flow scale with the Reynolds number R based on the channel half-width, channel wall speed, and kinematic viscosity. The various curves plotted in figure 1.5 represent the

$streak$: $\hat{u}_0 = O(1)$ in green;
$roll$: $(\hat{v}_0,\hat{w}_0) = O(R^{-1})$ in blue;

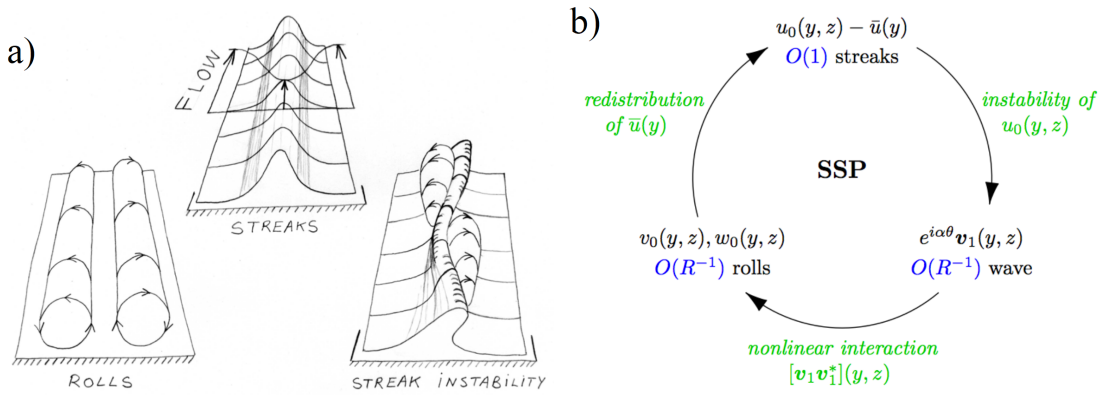

Figure 1.4: (a) Sketches of the rolls, streaks, and streak instabilities that drive the SSP. (b) Schematic depiction of the SSP feedback loop for a generic wall-bounded shear flow proposed by Waleffe (1995). Weak [$O(R^{-1})$, where here the Reynolds number $R \equiv U_0 H_0/\nu$ and U_0 and H_0 are characteristic velocity and length scales of the shear flow] streamwise rolls redistribute the imposed background shear creating $O(1)$ streaks. Strong spanwise inflectional instabilities lead to $O(R^{-1})$ streamwise-varying Rayleigh instability waves, which nonlinearly interact to sustain the $O(R^{-1})$ spanwise rolls. (Images from Waleffe (2005).)

$$
\begin{aligned}
&\textit{fundamental } x \textit{ mode}\text{: } \hat{\mathbf{u}}_1 = O(R^{-0.9}) \text{ in red; and} \\
&\textit{higher } x \textit{ harmonics}\text{: } \hat{\mathbf{u}}_n = o(R^{-1}),\ n > 1 \text{ in magenta and tan,}
\end{aligned}
$$

where the velocity field $\boldsymbol{u}(x,y,z) = \sum_n \hat{\boldsymbol{u}}_n(y,z) e^{i\left(\frac{2n\pi x}{L_x}\right)}$ and L_x is the (fixed) domain length in the streamwise (x) direction. The scaling of these lower-branch solutions of the full NS equations accords with those underlying the elegant and independently-developed asymptotic theory derived by Hall and collaborators [Hall & Smith (1991), Hall & Sherwin (2010)], who employ the terminology vortex–wave interaction or VWI theory.

In the VWI formalism, comparably weak [$O(1/R)$] streamwise vortices, sustained by Reynolds stress divergences concentrated in a critical layer, induce a strong [$O(1)$] streaky streamwise flow. The velocity components in VWI theory are expanded in asymptotic series as follows:

$$
\begin{aligned}
u(x,y,z,t;R) &\sim \bar{u}(y,z) + R^{-5/6}\hat{u}(y,z)e^{i\alpha(x-ct)} + c.c. + \cdots, \\
v(x,y,z,t;R) &\sim R^{-1}\bar{v}(y,z) + R^{-7/6}\hat{v}(y,z)e^{i\alpha(x-ct)} + c.c. + \cdots, \\
w(x,y,z,t;R) &\sim R^{-1}\bar{v}(y,z) + R^{-5/6}\hat{w}(y,z)e^{i\alpha(x-ct)} + c.c. + \cdots,
\end{aligned}
\tag{1.1}
$$

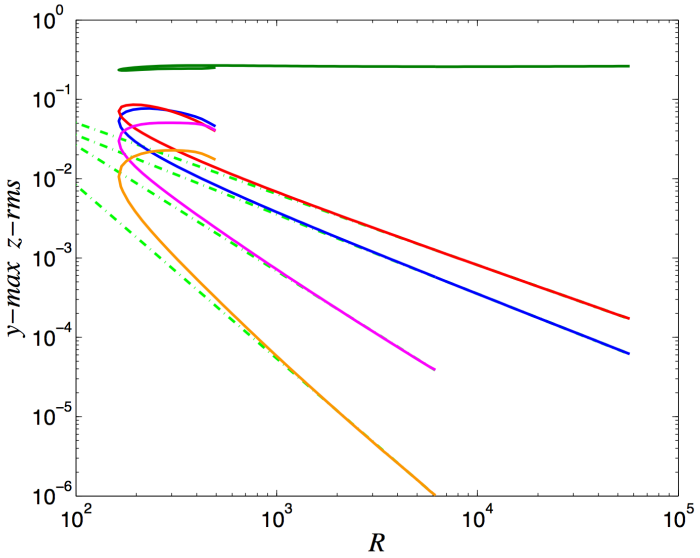

Figure 1.5: Bifurcation diagram reproduced from Wang *et al.* (2007) depicting how various streamwise Fourier modes of the velocity field associated with the ECS designated 'EQ1' in plane Couette flow scale with Reynolds number. The different lines represent the $streak$: $\hat{u}_0 = O(1)$ in green; $roll$: $(\hat{v}_0,\hat{w}_0) = O(R^{-1})$ in blue; $fundamental\ x\ mode$: $\hat{\mathbf{u}}_1 = O(R^{-0.9})$ in red; and $higher\ x\ harmonics$: $\hat{\mathbf{u}}_n = o(R^{-1})$, $n > 1$ in magenta and tan.

presuming a planar (wall-parallel) critical layer. Here (u, v, w) are the streamwise, wall-normal and spanwise velocity, respectively, and an overbar denotes a streamwise average; (x, y, z) are the streamwise, wall-normal and spanwise coordinates; t is the time variable; $2\pi/\alpha$ is the streamwise wavelength of the single x-varying Fourier mode; c is the real phase speed; and $c.c.$ denotes complex conjugate. Given these expansions, the x-varying fluctuation fields satisfy 'quasilinear' equations with respect to the leading-order streak velocity. The 3D linearized NS equations for the fluctuations then can be collapsed into the two-dimensional (2D) generalized Rayleigh equation for the Fourier coefficient $\hat{p}(y, z)$ of the fluctuation pressure field. Within a critical layer, where $\bar{u}(y, z) = c$, the x-varying Rayleigh mode is singular, and the nonlinear self-interaction of the amplified spanwise fluctuation velocity forces a jump in the x-averaged x-vorticity, thereby driving roll motions outside the critical layer.

Blackburn *et al.* (2013) and Eckhardt & Zammert (2018) have demonstrated that VWI states can exist on ever smaller spatial scales as the Reynolds number is increased. Specifically, when the

streamwise and spanwise wavenumbers are increased such that their ratio remains fixed, the ECS adopt a self-similar form in which the coherent structure becomes localised in the wall-normal direction within a 'production' layer having a thickness comparable to the inverse spanwise (or streamwise) wavenumber. More recently, Hall (2018) extended VWI theory to encompass an array of vortex-wave interactions in which streak and roll pairs are stacked in the wall-normal direction. For a linear background velocity profile (as in unbounded Couette flow), the VWI states are equispaced in y, while the only nonlinear velocity profile that proves admissible is logarithmic, corresponding to a logarithmic spacing of the VWI states.

1.5 Challenges and Objectives

As asserted in section 1.3, ECS are believed to provide a scaffold in phase space for turbulent dynamics. Nevertheless, to date, the relevance of ECS has been convincingly established only for modest Re_τ (i.e., transitional) flows and for the near-wall cycle of turbulent flows, which is dominated by the dynamics of the small-scale streamwise streaks and vortices for which the *effective* Reynolds number is modest. The existence (or not) of an inertial-layer SSP supporting the formation and evolution of turbulent superstructures remains a subject of ongoing investigation. In particular, a quantitative SSP theory accounting for these outer-region structures has not been developed to the same degree that one has been for their near-wall counter-parts (Hwang & Cossu, 2010); indeed, development of such a theory is a primary objective of this dissertation. Elucidation of the intrinsic nonlinear dynamics and structure of the inertial layer is a prerequisite for increased understanding of 'inner–outer' interactions, which in turn may be leveraged for the design of improved flow control strategies and could enable systematically-reduced numerical simulations of turbulent wall-flows at high-Re_τ that are not yet tractable via DNS.

A fundamental tenet of the SSP theory derived in this investigation is that viscous forces are subdominant (on average) in the inertial layer; hence, viscous diffusion must be, upon suitable averaging, asymptotically small there. This assertion is supported by the analysis of Wei *et al.* (2005) employing the mean momentum balance (MMB). To derive the MMB, e.g., for fully devel-

Physical layer	Magnitude ordering	Δy increment	$\Delta\langle U\rangle$ increment
I	$\|\text{PG}\| \cong \|\text{MV}\| \gg \|\text{TI}\|$	$O(\nu/u_\tau)$ (≤ 3)	$O(u_\tau)$ (≤ 3)
II	$\|\text{MV}\| \cong \|\text{TI}\| \gg \|\text{PG}\|$	$O(\sqrt{\nu h/u_\tau})$ ($\cong 1.6$)	$O(U_\infty)$ ($\cong 0.5$)
III	$\|\text{PG}\| \cong \|\text{MV}\| \cong \|\text{TI}\|$	$O(\sqrt{\nu h/u_\tau})$ ($\cong 1.0$)	$O(u_\tau)$ ($\cong 1$)
IV	$\|\text{PG}\| \cong \|\text{TI}\| \gg \|\text{MV}\|$	$O(h)$ ($\to 1$)	$O(U_\infty)$ ($\to 0.5$)

Table 1.1: Magnitude ordering and scaling behaviors associated with the four-layer structure of the mean momentum equation for turbulent channel flow. Note that the layer IV properties are asymptotically attained as $Re_\tau \to \infty$. PG: mean pressure gradient, TI: Turbulent inertia, and MV: mean viscous force. (Adapted from Klewicki (2013*b*).)

oped channel flow, a long-time average of the x-momentum equation is taken, after decomposing $u = \langle U\rangle(y) + u'(x, y, z, t)$ and similarly for other variables. Here, the angle brackets indicate the long-time average and the prime denotes a fluctuation about that mean. The resulting MMB is

$$\underbrace{\mu\partial_y^2\langle U\rangle}_{MV} + \underbrace{\partial_y(-\rho\langle u'v'\rangle)}_{TI} = \underbrace{\partial_x\langle p\rangle}_{PG}, \tag{1.2}$$

where MV denotes the mean viscous force, TI turbulent inertia (i.e., the gradient of the Reynolds stress), and PG the mean pressure gradient, and μ and ρ are the dynamic viscosity and the fluid density, respectively. Figure 1.6a shows the ratio of the mean viscous force to turbulent inertia (MV/TI) in turbulent channel flow (Elsnab *et al.*, 2017). At large Re_τ, four distinct regions emerge. Table 1.1 summarizes the dominant force balances in each layer, the sizes of the different layers, and the $\Delta\langle U\rangle$ increment for each layer. In layers I, II, and III, the mean viscous force contributes to the leading order balance. In layer IV, the focus of this investigation, the mean viscous force is subdominant. This diminution is consistent with the kinematic pattern of UMZs and VFs: the bulk of the flow is homogenized, with strong gradients and, hence, viscous forces being relegated to thin regions of the instantaneous flow. Indeed, Klewicki (2013*b*) has shown that the fissure width scales as $Re_\tau^{-1/2}$. Accordingly, the predicted dependence of the fissure thickness on Re_τ is a distinguishing feature of this inertial layer SSP.

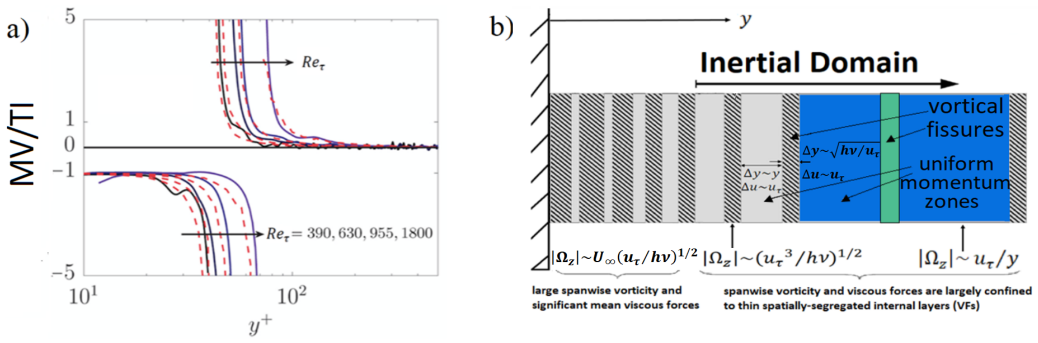

Figure 1.6: Singular nature of the TBL. (a) Plot showing the ratio of the mean viscous force (MV) to turbulent inertia (TI), i.e. to the Reynolds stress gradient, in turbulent channel flow at four different values of Re_τ; data taken from the water channel experiments by Elsnab *et al.* (2017). The mean viscous force is significant in a volume-averaged sense only in a near-wall domain of size $O(\sqrt{Re_\tau})$ in viscous (or 'plus') units, corresponding to a domain of size $O(h/\sqrt{Re_\tau})$ in outer units. Outboard of the peak in the Reynolds stress (where the force ratio tends to plus or minus infinity), the volume-averaged mean viscous force is negligible. (b) Schematic illustrating the concentration of spanwise vorticity within VFs that, at large Re_τ, become increasingly widely separated with increasing distance from the wall. (Adapted from Klewicki (2013*a*,*b*).) The new SSP theory developed herein targets UMZs and VFs located in the inertial domain, as highlighted in blue and green, respectively.

The four-layer structure implied by the MMB imposes important restrictions on any attempt to extend existing mechanistic SSP theories to account for large-scale roll and streak structures in the inertial domain (i.e., in layer IV). In particular, if the streamwise streaks $[\bar{u} = O(1)]$ are sustained by streamwise rolls $[(\bar{v}, \bar{w}) = O(1/Re_\tau)]$ as in Hall *et al.* [Hall & Smith (1991), Hall & Sherwin (2010)] and Waleffe (1995, 1997), then necessarily the *effective* Reynolds number is $O(1)$. To support this assertion, the velocity field can be decomposed into an x-averaged component, denoted by an overbar, plus an x-dependent fluctuation denoted by a prime. For a shear flow without a mean pressure gradient, the x-mean x-momentum equation then becomes

$$\partial_t \bar{u} + \bar{v}\partial_y \bar{u} + \bar{w}\partial_z \bar{u} = \frac{1}{Re_\tau}(\partial_y^2 + \partial_z^2)\bar{u} + \text{H.O.T.}, \tag{1.3}$$

where H.O.T. denotes higher-order terms as $Re_\tau \to \infty$. Upon rescaling such that $\bar{u} \sim \bar{u}_0$ and $(\bar{v}, \bar{w}) \sim \frac{1}{Re_\tau}(\bar{v}_1, \bar{w}_1)$, and omitting the H.O.T., (1.3) becomes

$$\partial_t \bar{u}_0 + \bar{v}_1 \partial_y \bar{u}_0 + \bar{w}_1 \partial_z \bar{u}_0 = (\partial_y^2 + \partial_z^2)\bar{u}_0, \tag{1.4}$$

which clearly shows that the effective Reynolds number is unity with this scaling. Consequently, neither Waleffe's SSP theory nor Hall & Smith's VWI formalism can directly apply to outer-region superstructures.

The first difficulty with these theories is evident upon consideration of dominant balance of forces in layer IV. From inspection of (1.4) it is clear the *streaks*[1] *(and, in fact, the rolls) are viscously dominated* throughout the spatial region they occupy whenever the effective Reynolds number is $O(1)$. This dominant balance directly conflicts with the defining characteristic of the inertial layer: namely, viscous forces are subdominant on average in layer IV, hence viscous diffusion must be (again upon suitable averaging) asymptotically small there. To ensure mean diffusion is asymptotically small in the proposed inertial-layer SSP, the strength of the roll motion satisfies $O(1/Re_\tau) \ll (\bar{v}, \bar{w}) \ll O(1)$.

The second limitation of both VWI and Waleffe's SSP theory is that, even in the limit of infinite Reynolds number, the x-averaged streaky streamwise flow varies smoothly across the flow domain. This absence of anything akin to a jump in flow speed across a VF is consistent with the effective Reynolds number for the x-mean flow being $O(1)$ (see, e.g., Beaume *et al.* (2015)). To illustrate this point, figure 1.7 shows the streamwise- and spanwise-averaged streamwise velocity for 'EQ2', an *upper-branch* equilibrium ECS in plane Couette flow, at two Reynolds numbers separated by a decade (at fixed domain size). Although this velocity profile superfically resembles part of a staircase, the upper and lower 'fissures' do not show any Reynolds number dependence. Thus, even at large Reynolds number, the profile will remain smooth and no singular shear layer will form.

[1] Strictly, *streak* refers to the difference between the streamwise- and horizontally-averaged streamwise flow: $\bar{u} - \overline{u}^{xz}$, where $\overline{(\cdot)}^{xz}$ denotes a horizontal average. Here, however, we loosely refer to a streak simply as $\bar{u}$. Noting that the essential attribute of a streak is the *inflectional velocity anomaly* induced at its flanks that supports a streamwise-varying instability, this less restrictive definition seems more appropriate for flows with UMZs and VFs, for which the emergent $\overline{u}^{xz}$ profile itself may be inflectional and inviscidly unstable (cf. figure 2.2b).

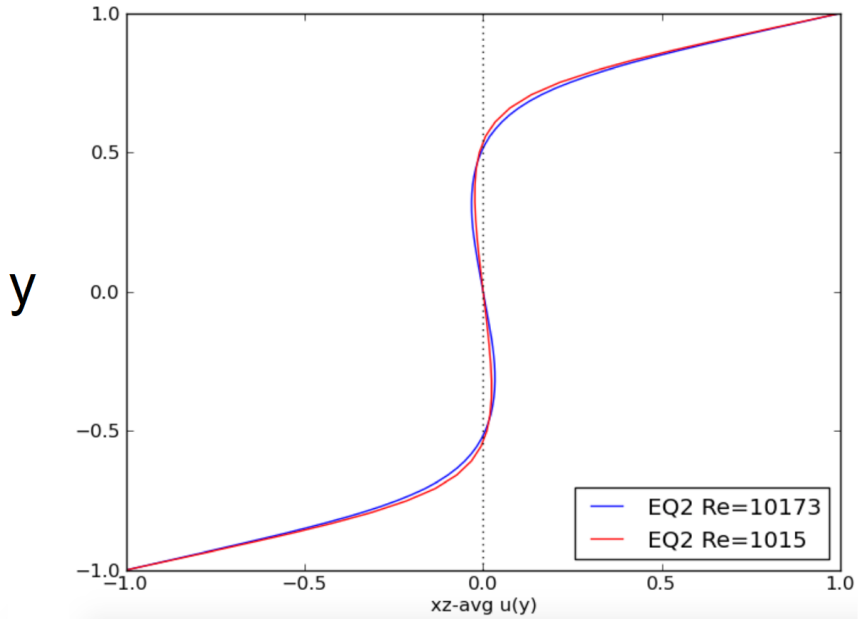

Figure 1.7: Streamwise- and spanwise-averaged streamwise velocity for 'EQ2', an upper-branch equilibrium ECS in plane Couette flow, at two Reynolds numbers $Re = U_w h/\nu$, where U_w is the wall velocity, separated by a decade (at fixed domain size). Data courtesy of J. Gibson.

In light of the limitations of existing SSP/VWI theories, the overarching objective of this dissertation is to seek a mechanistic SSP-like explanation for the emergence and sustenance of staircase-like profiles of instantaneous streamwise velocity in the inertial region of turbulent wall flows via an asymptotic ECS construction as $Re_\tau \to \infty$.

1.6 Hypothesis

The central hypothesis to be investigated is whether counter-rotating streamwise rolls stacked in the fissure-normal direction, as shown in figure 1.8, can differentially homogenize an imposed background shear flow *and* be sustained by an instability of the emergent shear layer. More specifically, infinitely many copies of the counter-rotating roll pattern depicted are imagined to be stacked in the y-direction in unbounded plane Couette flow (for which the background shear $U_b(y) = y$ in the domain $-\infty < y < \infty$), an imperfect but useful surrogate for the inertial domain of turbulent wall flows. Streamwise rolls and the streaks they induce are key components of equilibrium, traveling-wave and periodic-orbit exact coherent states arising in incompressible wall-bounded shear flows

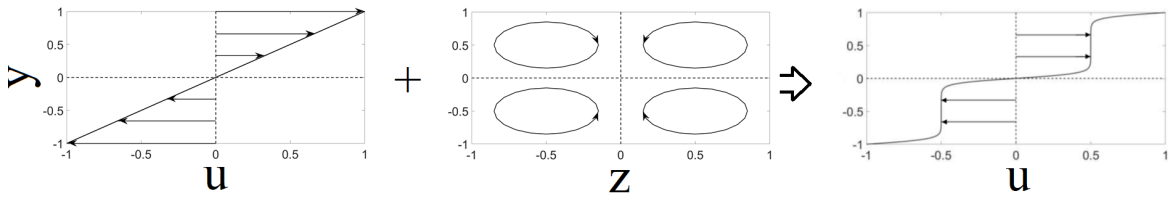

Figure 1.8: Proposed flow configuration in which sufficiently strong rolls in the y–z plane redistribute the imposed background shear in the streamwise velocity profile (here taken to be unbounded Couette flow) yielding the staircase-like UMZ/VF profile.

(Waleffe, 1997; Faist & Eckhardt, 2003; Wedin & Kerswell, 2004; Nagata, 1990; Duguet *et al.*, 2008; Gibson *et al.*, 2008; Duguet *et al.*, 2010). ECS necessarily are self-sustaining since, by construction, they are *invariant* solutions of the NS equations. Accordingly, we seek a mechanistic explanation for the occurrence of VFs and UMZs by deriving from the NS equations an asymptotic SSP formalism whose ECS solutions exhibit these flow features.

There are three primary elements that distinguish this hypothesis from that underlying Waleffe's SSP and Hall's VWI theory. First, the homogenizing action of large-scale streamwise vortices, with $\bar{v}, \bar{w} = O(\varepsilon)$, where $1/Re \ll \varepsilon \ll 1$ as $Re \to \infty$ and Re is a suitably defined Reynolds number, induces $O(1)$ UMZs in a sheared flow. Hence, the streamwise vortices, while still comparably weak relative to the $O(1)$ streaks, are asymptotically stronger than those in classical SSP/VWI theory. Secondly, in the limit $Re \to \infty$ with $\bar{u} = O(1)$ and $O(1/Re) \ll (\bar{v}, \bar{w}) \ll O(1)$, a three-region (rather than two-region) asymptotic structure emerges in the fissure-normal (y) direction. As shown in figure 1.9, the bulk of the spatial domain is occupied by UMZs. Singularities arising in the effectively-inviscid roll/streak flow within the UMZs are viscously regularized within *emergent* internal shear layers (VFs) of dimensionless thickness $O(\Delta)$, where $\Delta(Re) \to 0$ as $Re \to \infty$. Within each fissure, the fissure-normal inflectional shear supports an inviscid (i.e., Rayleigh) instability. The Rayleigh mode, being marginally-stable, exhibits a singularity that is viscously regularized within an even thinner critical layer (CL) of dimensionless thickness $O(\delta)$, with $\delta/\Delta \to 0$ as $Re \to \infty$, embedded within each fissure; see figure 1.9. Thirdly, the Rayleigh-

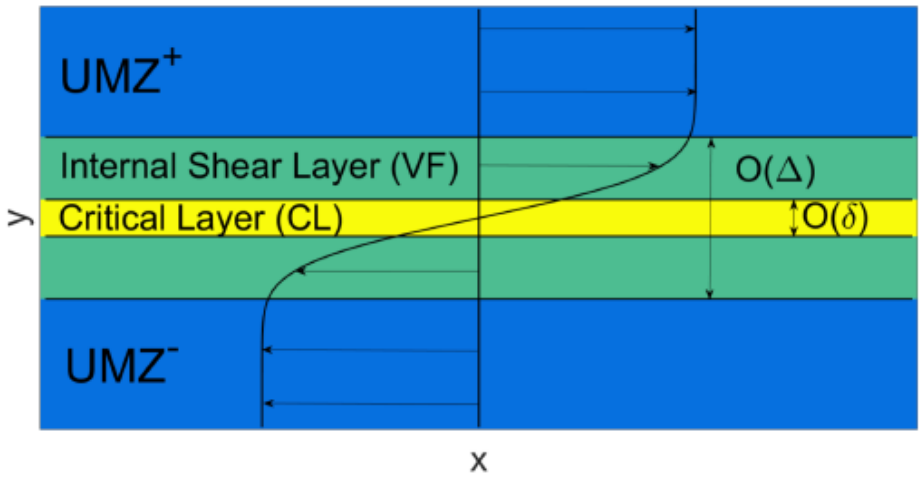

Figure 1.9: Schematic diagram of the hypothesized three-region asymptotic structure in the fissure-normal direction centred on a fissure located at $y = 0$ (cf. highlighted region in figure 1.6(b))

.

mode streamwise wavenumber $\alpha = \breve{\alpha}/\Delta$, with $\breve{\alpha} = O(1)$; in contrast, $\alpha = O(1)$ in VWI theory. Moreover, since here $\alpha \gg 1$ (see below), the Rayleigh mode is confined to the VF, as the fluctuation fields decay exponentially with distance from the fissures and at asymptotically large Re (whence $\Delta \to 0$), therefore are transcendentally small within the UMZs. This short streamwise-wavelength neutral Rayleigh mode riding on an internal shear layer of thickness $O(\Delta)$ is rendered three-dimensional by the slow spanwise (z) variation of the streak velocity field within the VF, and the refraction of the mode induces a commensurately short spanwise wavelength.

Motivation for the large streamwise wavenumber approximation is provided by the growth-rate curve shown in figure 1.10, obtained by performing an Orr-Sommerfeld linear stability analysis using the background velocity profile

$$\bar{U}_b(y) = \text{erf}\left(\frac{y}{\varepsilon}\right). \tag{1.5}$$

This specification yields a step-like profile for the streamwise velocity similar to that depicted in figure 1.9. The linear stability analysis was performed in an unbounded domain in y for three

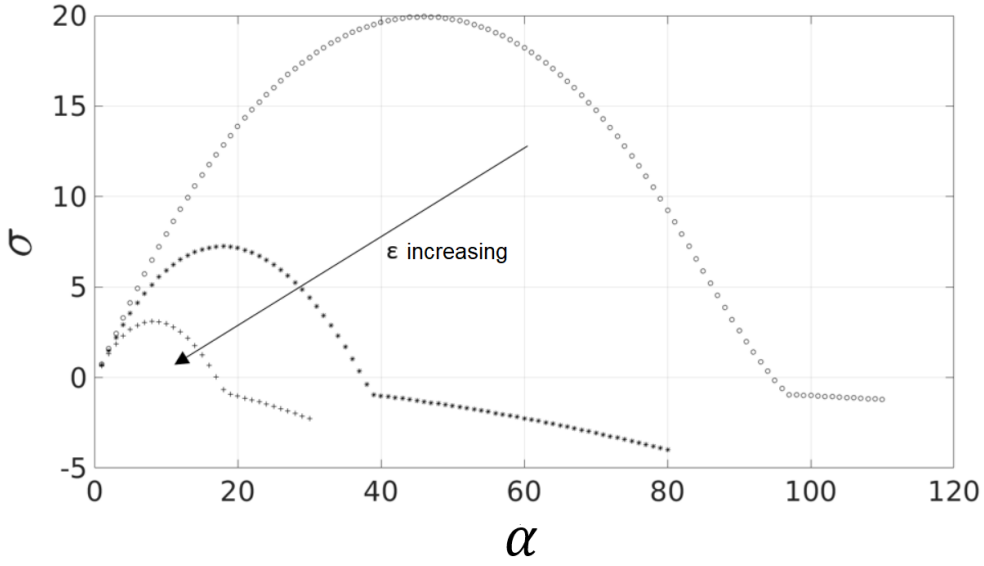

Figure 1.10: Growth rate curves obtained from an Orr-Sommerfeld linear stability analysis using an error-function background streamwise velocity profile. Here, α is the streamwise wavenumber, σ is the real growth rate, and ε is a small parameter characterizing the thickness of the shear layer in the imposed background streamwise velocity profile. As expected for (largely) inviscid shear instabilities, α for both the fastest-growing and non-zero neutral mode increases as $\varepsilon \to 0$.

values of $\varepsilon = (0.01, 0.025, 0.05)$ and for a Reynolds number equal to $\varepsilon^{-2} = (10000, 1600, 400)$. Figure 1.10 clearly indicates that, as the shear is confined to ever thinner regions, both the fastest-growing mode and the neutral mode having non-zero wavenumber are shifted to larger values of α. With the thickness of the fissure empirically scaling like $Re_\tau^{-1/2}$, it is natural then to seek a solution for which α is asymptotically large.

1.7 Summary

Generically, fluid flows can be categorized into two regimes, laminar and turbulent. Most naturally occurring flows are turbulent. Turbulent motions are not completely disordered; rather turbulent wall flows are dominated both energetically and dynamically by spontaneously-occurring coherent structures in the form of streamwise rolls and streaks. Quasi-coherent flow structures have long been observed in the near-wall region, but more recently they have been observed on a hierarchy of scales including outside the buffer layer. Meinhart & Adrian (1995) were the first to document that,

away from the wall, the instantaneous streamwise velocity exhibits a staircase-like profile, with regions of quasi-uniform momentum separated by internal shear layers termed vortical fissures. These profiles have since been observed and their properties quantified by several other research groups.

Canonical turbulent wall flows exhibit a four-layer structure with distinct dominant force balances in the mean momentum equation being used to define each layer. Crucially, in the inertial domain (in layer IV), on average, viscous forces are subdominant. In the near-wall region (i.e., layers I and II), Waleffe's SSP and Hall's VWI theories can account for the existence and sustenance of rolls and streaks. In both theories, the feedback loop shown in figure 1.4 is operative. Weak streamwise rolls redistribute the background shear creating $O(1)$ streaks. Strong spanwise inflectional instabilities of the streaks support $O(R^{-1})$ instability waves that nonlinearly interact to drive the $O(R^{-1})$ spanwise rolls. An immediate consequence is that the effective Reynolds number governing the streak and roll motions is $O(1)$, implying these key components of the turbulence are viscously dominated. Viscous rolls and streaks are not apt candidates for coherent structures in layer IV because:

1. Volume-mean viscous forces then will be significant within this inertial domain; and

2. The streak flow will be smoothly-varying, precluding the formation of UMZs and VFs.

In this dissertation, the NS equations are examined in the limit of large Reynolds number to assess whether a new, multiple-scale SSP formalism can explain the formation and sustenance of UMZs and interlaced VFs, arguably the primal coherent structures in the outer part (layer IV) of turbulent wall flows. Specifically, the question to be addressed is whether counter-rotating streamwise rolls, stacked in the fissure-normal direction, can differentially homogenize an imposed background shear flow, and thereby induce VFs, while a small-scale instability of the VFs simultaneously sustains the rolls?

To this end, unbounded plane Couette flow is analyzed. Chapter 2 details the required asymptotic analysis. In chapter 3, the numerical methods used to solve the resulting asymptotically-

reduced PDEs and to obtain the key results, including numerical reconstructions of the ECS fields, are described. These results are presented in chapter 4, and the associated conclusions and physical implications are summarized in chapter 5.

CHAPTER 2

LARGE REYNOLDS NUMBER AND LARGE WAVENUMBER ASYMPTOTIC ANALYSIS

2.1 Introduction

In this chapter, a large Reynolds number and large streamwise wavenumber analysis of the NS equations is performed in an effort to derive a reduced set of equations and associated SSP that can explain the observed staircase-like profile of streamwise velocity. The analysis is intended to apply qualitatively to a portion of the flow domain that has been excised sufficiently far away from the wall (i.e. in layer 4), as shown schematically in figure 2.1. As noted in chapter 1, unbounded plane Couette flow is utilized here as an imperfect, but more tractable surrogate configuration.

We choose to scale velocities by the friction velocity u_τ, since the jump in streamwise flow speed across each fissure is a few times u_τ (figures 1.2a and 1.3a), and lengths by l_y, the dimensional distance between adjacent – and, in this construction, equispaced – VFs. The governing incompressible Navier–Stokes equations then can be expressed in dimensionless form,

$$\partial_t \mathbf{u} + \mathbf{u} \cdot \nabla \mathbf{u} = -\nabla p + \frac{1}{Re} \nabla^2 \mathbf{u}, \tag{2.1}$$

where $\mathbf{u} = (u, v, w)$ and p are the velocity vector and pressure, respectively, and incompressibility requires $\nabla \cdot \mathbf{u} = 0$. $Re \equiv u_\tau l_y / \nu$ is a Reynolds number defined using l_y rather than the outer length scale h; that is, $Re \neq Re_\tau$, a point we return to later. Given this non-dimensionalisation, the imposed background plane Couette flow $u = y$, where $-\infty < y < \infty$. Recently, Hall (2018) constructed asymptotic ECS comprising an infinite wall-normal array of VWI states, each with a planar critical layer, firstly in unbounded Couette flow and subsequently in background shear flows with logarithmic profiles. The theory we develop shares certain commonalities with the

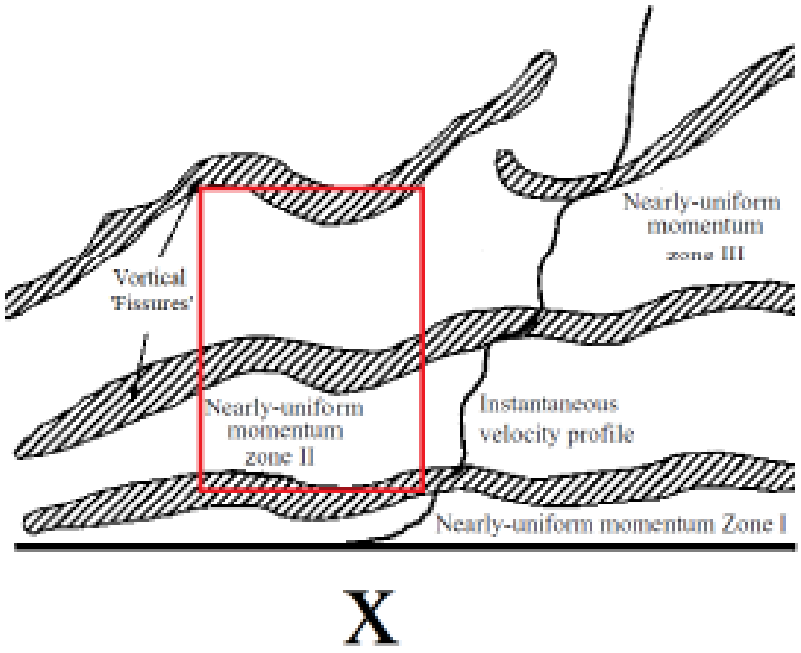

Figure 2.1: Schematic of UMZs and VFs spanning a TBL showing excised domain. (Adapted from Priyadarshana *et al.* (2007).)

former construction but, as discussed further in chapter 5, the distinctions highlighted in section 1.5 remain apt.

As in VWI and related theories (Beaume *et al.*, 2015; Chini *et al.*, 2017), we decompose all flow fields into an x-mean plus a fluctuation about that mean to separate the streamwise-averaged roll and streak flow from the streamwise-varying instability mode. Because the wavelength of the instability mode is small relative to the roll diameter and because the mode is refracted, a short scale not only in x but also in z is induced. This rapid spanwise variation of the fluctuation is captured using a Wentzel–Kramers–Brillouin–Jeffreys (WKBJ) formalism introduced in section 2.3 Accordingly, we replace the streamwise average with an averaging operation that removes all variation in x and fast variability both in time and in the spanwise direction. Nevertheless, we continue to denote mean fields with overbars and fluctuation fields with primes.

In the following sections, we first analyze the flow within the UMZs adjacent to the VF centered on $y = 0$ and subsequently analyze the VF, itself, and its embedded CL (see figure 1.9). Table 2.1

Domain		Dominant Contributions		ECS Component		
Region	**Size**	**Mean Terms**	**Fluctuations**	**S**	**R**	**F**
UMZ	$O(1)$	NI,PG	E.S.T.	$O(1)$	$O(\Delta^2)$	E.S.T.
VF	$O(\Delta)$	NI,VNF,PG	LI,PG	$O(1)$	$O(\Delta^2)$	$O(\Delta^3)$
CL	$O(\delta)$	VNF,RSD	LI,VNF,PG	$O(\Delta)$	$O(\Delta^2)$	$O(\Delta^2)$

Table 2.1: Summary of the scalings of the mean and fluctuation fields and the dominant terms arising in the relevant force balances in each of the three subdomains: UMZ = uniform momentum zone; VF = vortical fissure (internal shear layer); and CL = critical layer. ECS component: S = streak; R = roll; and F = fluctuation. Forces: NI = nonlinear inertia; LI = linearized inertia; PG = pressure gradient; VNF = viscous normal force; and RSD = Reynolds stress divergence. As demonstrated by the analysis performed in chapter 2, the dimensionless VF thickness $\Delta = Re^{-1/4}$, while the CL thickness $\delta = Re^{-1/2}$. E.S.T. = exponentially small terms.

summarizes the scalings of the leading-order fields and highlights the dominant force balances arising in each of the three sub-regions for both the mean and fluctuating flow components.

2.2 Uniform Momentum Zones

The dynamics within the UMZs is governed by the two-dimensional (2D) but three-component (i.e. x-independent) NS equations, since the streamwise-varying fluctuation fields are exponentially small there. Thus, the momentum equations reduce to

$$\partial_t \overline{u} + (\overline{\mathbf{v}}_\perp \cdot \nabla_\perp)\,\overline{u} \;=\; \frac{1}{Re}\nabla_\perp^2 \overline{u}, \tag{2.2}$$

$$\partial_t \overline{\mathbf{v}}_\perp + (\overline{\mathbf{v}}_\perp \cdot \nabla_\perp)\,\overline{\mathbf{v}}_\perp \;=\; -\nabla_\perp \overline{p} \,+\, \frac{1}{Re}\nabla_\perp^2 \overline{\mathbf{v}}_\perp, \tag{2.3}$$

where the $\perp$ subscript refers to the y–z plane and the perpendicular (i.e. roll) velocity vector $\bar{\mathbf{v}}_\perp = (\bar{v}, \bar{w})$. From (2.2)–(2.3), it is clear that the mean streamwise velocity acts as a passive scalar within the UMZs, being advected by the rolls and diffused. The rolls are not directly forced within the UMZs and would therefore decay in the absence of the forcing localized within the bounding VFs. An immediate and significant physical implication is that the internal layers (sometimes referred to as 'interfaces' in the literature, e.g. see de Silva *et al.* (2017)) are not dynamically

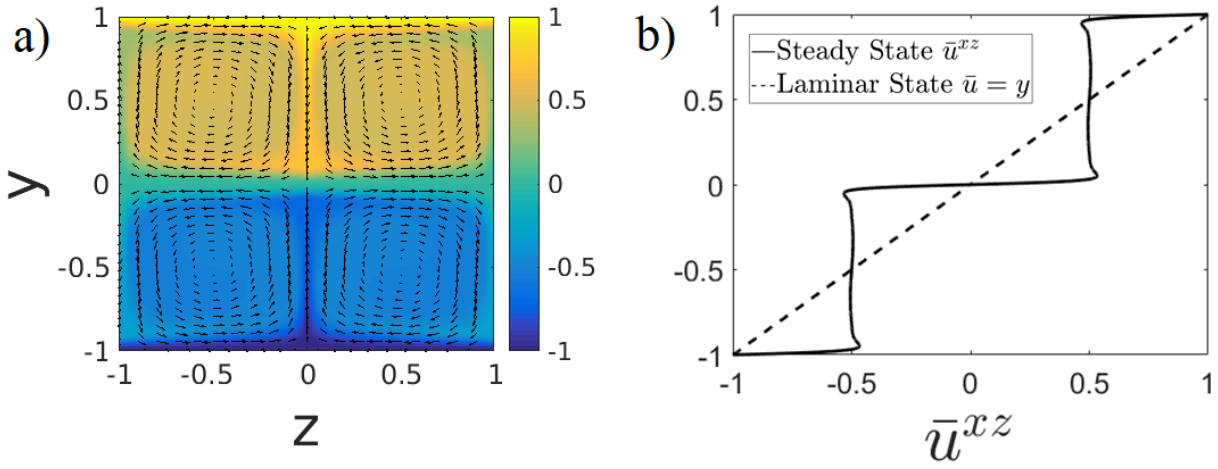

Figure 2.2: Differential homogenization of a background Couette flow (a,b) by the stacked counter-rotating pattern of steady rolls (vector plot in (a), obtained from (2.11)–(2.12)) leading to the emergence of UMZs and an internal shear layer (b); i.e. an embedded VF. This process is realized only for sufficiently large values of the *effective* Reynolds number $\bar{a}Re$, where the roll amplitude $\bar{a}(Re) \to 0$ as $Re \to \infty$. For example, in the Fourier–Chebyshev pseudospectral computations used to generate these results, $\bar{a}Re \approx 10^4$.

passive; rather, the driving agency for the staircase-like profiles of streamwise velocity is confined within the regions of concentrated spanwise vorticity.

As noted in section 1.5, we insist that the *dynamical* influence of viscosity on the streak and roll flow is weak, at least in a volume-averaged sense. In particular, the size of the roll flow is denoted by $\bar{a}$, where $\bar{a}(Re) \to 0$ as $Re \to \infty$ (implying that the rolls are weak compared to the $O(1)$ streamwise streak flow), then we require that the *effective* Reynolds number $\bar{a}Re$ governing the dynamics of the rolls and streaks within the UMZs becomes unbounded in the large-Re limit. It is well-known that in the presence of a steady cellular (2D) velocity field a passive scalar will be homogenized in the limit of large Peclet number (Rhines & Young, 1983). Since $\bar{a}Re \to \infty$, and given that we seek stacked ECS with steady rolls, the passive streak velocity field $\bar{u}$ therefore is differentially homogenized within regions of closed streamlines of the roll flow.

This process is clearly depicted in figure 2.2. The right-hand plot shows the initial and steady-state spanwise-averaged streamwise velocity profiles $\overline{u}^{xz}(y)$. These profiles are obtained by nu-

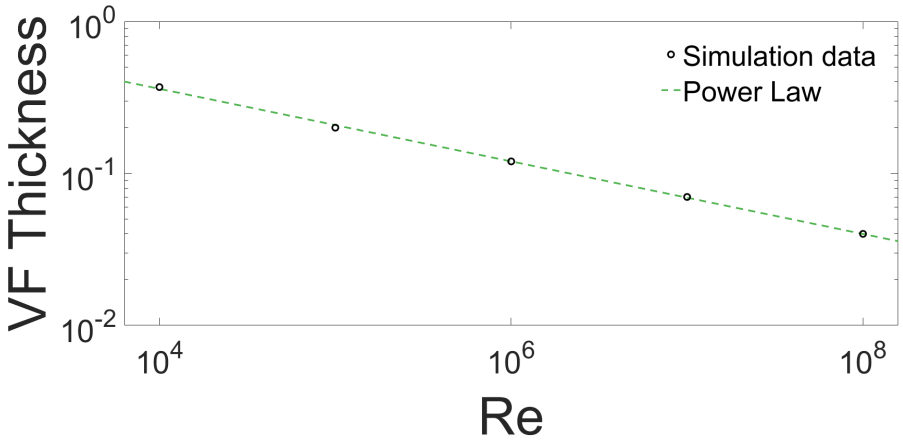

Figure 2.3: Dimensionless VF thickness as a function of Re calculated from the steady-state numerical solution of the advection–diffusion equation (2.2) for $\overline{u}(y, z, T)$, regularized by the inclusion of Laplacian diffusion $(\bar{a}Re)^{-1}\nabla_\perp^2\overline{u}$ on the right hand side, for $L_z = 2$.

merically integrating (2.2) using a Fourier–Chebyshev pseudospectral algorithm with the prescribed steady, spanwise-periodic roll velocity field given below in (2.11)–(2.12) and plotted in figure 2.2(a), for an effective Reynolds number $\bar{a}Re \approx 10^4$, a dimensionless core vorticitiy $\bar{\Omega}_c \approx 7.35$, and a prescribed roll spatial-period $L_z = 2$. Of particular note is the emergence of an internal shear layer centered on the plane $y = 0$. Figure 2.3 shows that [given $O(1/Re) \ll (\bar{v}, \bar{w}) \ll O(1)$] the thickness of the fissure is a function of Re with an approximate power-law exponent found to be -0.24 (at least for $L_z = 2$). Here, it should be recalled that $Re \neq Re_\tau$; in fact, when proper account is taken that $l_y = l_y(Re_\tau)$, our inertial-layer SSP theory predict that the geometric-mean VF scaling $Re^{-1/4}$ corresponds to $Re_\tau^{-7/16} \approx Re_\tau^{-1/2}$. See appendix A for further details.

Rhines & Young (1983) demonstrate that if the evolution is laminar (e.g. driven by a strictly steady 2D cellular velocity field acting on a scalar field exhibiting a uniform gradient at some initial time, say $t = 0$), scalar homogenization in the large Peclet number (Pe) limit generically occurs in two stages. During a time $t = O(Pe^{1/3})$, shear-augmented dispersion acts to homogenize the scalar field along streamlines. The subsequent homogenization of the scalar field across streamlines occurs over a much longer time $t = O(Pe)$. Crucially, diffusion is a leading-order process only during the first stage. In the present context, advection dominates perturbations due to diffusion,

'locking' contours of constant $\overline{u}$ to the streamline pattern induced by the rolls, throughout the second phase as well as in the final steady state. Plausibly, the time scale for homogenization may be reduced by turbulent mixing processes, but here no judgment is made regarding the time taken for a turbulent trajectory to visit the neighborhood of the steady ECS we construct. Nevertheless, we emphasize that within the UMZs viscous diffusion is weak relative to roll-induced advection for these ECS, in accord with the mean momentum balance outboard of the Reynolds stress peak (figure 1.6).

For *steady* rolls and streaks within the homogenized core of the UMZs, the following asymptotic expansions accordingly are posited:

$$u(x,y,z,t;Re) \sim \overline{u}_0(y,z) + E.S.T., \tag{2.4}$$

$$v(x,y,z,t;Re) \sim \bar{a}\bar{v}_2(y,z) + \ldots, \tag{2.5}$$

$$w(x,y,z,t;Re) \sim \bar{a}\bar{w}_2(y,z) + \ldots, \tag{2.6}$$

$$p(x,y,z,t;Re) \sim \overline{a}^2\overline{p}_4(y,z) + \ldots, \tag{2.7}$$

The numeric subscripts refer to $a\ posteriori$ determined powers of the small parameter Δ defining $\bar{a}$, and $E.S.T.$ denotes terms that are exponentially small in Re. These terms include the x-varying fluctuation fields within the UMZs and transcendentally small corrections to the homogenized field. Substituting the expansions into the governing equations, the leading-order steady equations are

$$(\overline{\mathbf{v}}_{2\perp}\cdot\nabla_\perp)\,\overline{u}_0 = \frac{1}{\overline{a}Re}\nabla_\perp^2\overline{u}_0, \tag{2.8}$$

$$(\overline{\mathbf{v}}_{2\perp}\cdot\nabla_\perp)\,\overline{\mathbf{v}}_{2\perp} = -\nabla_\perp\overline{p}_4 + \frac{1}{\overline{a}Re}\nabla_\perp^2\overline{\mathbf{v}}_{2\perp}. \tag{2.9}$$

Note that, in accord with the Prandtl–Batchelor theorem (Batchelor, 1956), the steady x-mean x-vorticity $\bar{\Omega}$ also is uniform within regions foliated by steady closed streamlines on which viscous diffusion is weak relative to advection. Hassan & Mezić (2019) recently extended the Prandtl-

Batchelor theorem from steady 2D flows to 2D flows with quasiperiodic time-dependence. Consequently,

$$\overline{\Omega} \equiv \partial_y \bar{w} - \partial_z \bar{v} \sim \nabla_\perp^2 (\overline{a}\overline{\psi}_2) \sim \overline{a}\overline{\Omega}_c + E.S.T., \tag{2.10}$$

where the (rescaled) roll streamfunction $\overline{\psi}_2(y,z)$ is defined such that ($\overline{v}_2$,$\overline{w}_2$)=($-\partial_z\overline{\psi}_2$,$\partial_y\overline{\psi}_2$). Unlike the constant core value of the x-mean streamwise velocity, which by symmetry must satisfy $\overline{u}_0 \sim 1/2$ for $0 < y < 1$ and $\overline{u}_0 = -1/2$ for $-1 < y < 0$, the (rescaled) homogenized value of the x-mean x-vorticity $\bar{\Omega}_c$, which fixes the precise value of the roll-induced circulation, is a primary unknown to be determined as part of the asymptotic analysis: effectively, $\bar{\Omega}_c$ is a nonlinear eigenvalue that will be shown to couple information from the various subdomains of the flow. Nonetheless, as demonstrated in Chini (2008), (2.10) is readily solved analytically on a rectangular domain of (asymptotically) known dimensions one unit in y and $L_z/2$ units in z, where L_z is the prescribed spanwise periodicity length of the rolls, subject to $\overline{\psi}_2(y,z) \to 0$ as the rectangular cell boundaries are approached. Using the given notation,

$$\overline{v}_2 = \bar{\Omega}_c \sum_{n=1,odd}^{\infty} \frac{2L_z}{(n\pi)^2} \left[\frac{\cosh[(2n\pi/L_z)(1/2-y)]}{\cosh(n\pi/L_z)} - 1 \right] \cos\left(\frac{2n\pi z}{L_z}\right), \tag{2.11}$$

$$\overline{w}_2 = \bar{\Omega}_c \sum_{n=1,odd}^{\infty} \frac{2L_z}{(n\pi)^2} \left[\frac{\sinh[(2n\pi/L_z)(1/2-y)]}{\cosh(n\pi/L_z)} \right] \sin\left(\frac{2n\pi z}{L_z}\right). \tag{2.12}$$

To avoid the need for iteration in the subsequent solution algorithm, and noting that $\bar{\Omega}_c = O(1)$, it proves useful here to introduce the slightly modified small parameter $\tilde{\Delta} = \bar{\Omega}_c^{-1/4}\Delta$ and rescaled mean fields $\bar{v} = \bar{\Omega}_c\tilde{v}$, $\bar{w} = \bar{\Omega}_c\tilde{w}$ and $\bar{p} = \bar{\Omega}_c^2\tilde{p}$, where *all* fields are (re-)expanded in asymptotic series in powers of $\tilde{\Delta}$ rather than Δ. With the new scaling the asymptotic expansions become

$$u(x,y,z,t;Re) \sim \overline{u}_0(y,z,T) + E.S.T., \tag{2.13}$$

$$v(x,y,z,t;Re) \sim \overline{a}\overline{\Omega}_c\tilde{v}_2(y,z,T) + E.S.T., \tag{2.14}$$

$$w(x,y,z,t;Re) \sim \overline{a}\overline{\Omega}_c\tilde{w}_2(y,z,T) + E.S.T., \tag{2.15}$$

$$p(x,y,z,t;Re) \sim \overline{a}^2\overline{\Omega}_c^2\tilde{p}_4(y,z,T) + E.S.T., \tag{2.16}$$

hence

$$\tilde{v}_2 = \sum_{n=1,odd}^{\infty} \frac{2L_z}{(n\pi)^2}\left[\frac{\cosh[(2n\pi/L_z)(1/2-y)]}{\cosh(n\pi/L_z)} - 1\right]\cos\left(\frac{2n\pi z}{L_z}\right), \tag{2.17}$$

$$\tilde{w}_2 = \sum_{n=1,odd}^{\infty} \frac{2L_z}{(n\pi)^2}\left[\frac{\sinh[(2n\pi/L_z)(1/2-y)]}{\cosh(n\pi/L_z)}\right]\sin\left(\frac{2n\pi z}{L_z}\right). \tag{2.18}$$

Moreover (2.8)–(2.9) reduce to

$$(\tilde{\mathbf{v}}_{2\perp}\cdot\nabla_\perp)\,\overline{u}_0 = \tilde{\Delta}^2\nabla_\perp^2\,\overline{u}_0, \tag{2.19}$$

$$(\tilde{\mathbf{v}}_{2\perp}\cdot\nabla_\perp)\,\tilde{\mathbf{v}}_{2\perp} = -\nabla_\perp\tilde{p}_4 + \tilde{\Delta}^2\nabla_\perp^2\,\tilde{\mathbf{v}}_{2\perp}. \tag{2.20}$$

Thus, the steady roll velocity field within the UMZs is known (with the understanding that $\bar{\Omega}_c$ is a to-be-determined constant), a key simplification.

2.3 Vortical Fissures

In the asymptotic limit $Re \to \infty$, the differential homogenization of $\bar{\Omega}$ leads to jump discontinuities in this field across the separatrices between adjacent roll cells. Moreover, in addition to the jumps in $\bar{u}$ induced between stacked cells, streamwise velocity anomalies in the form of narrow jets are driven between neighboring roll pairs at each fixed y away from the fissures. These discontinuities are smoothed by viscous forces and torques that act on the mean fields within asymptotically thin regions along the periphery of each cell. Here, we focus on the emergent shear layer centered on $y = 0$, but analogous considerations apply to all other VFs (located at $y = n$, for integer $n = \pm1, \pm2\ldots$). Similar scalings also apply to the narrow jets centered on $z = mL_z/2$, for integer $m = 0, \pm1, \pm2\ldots$, albeit with the roles of y and z interchanged and with the important distinction that, unlike the VFs, the jets are dynamically passive since in the present theory the x-varying fluctuations are exponentially small there.

The thickness of each VF follows from the usual laminar-BL scaling in which normal diffusion is balanced with advection, *viz.* $\tilde{\Delta} = (\bar{a}\bar{\Omega}_c Re)^{-1/2}$. For the VF centered on $y = 0$, we therefore

introduce a rescaled y coordinate $\mathcal{Y} \equiv y/\tilde{\Delta}$, and we decompose all field variables into mean plus slowly-modulated fluctuation components:

$$\begin{bmatrix} u(x,y,z,t;Re) \\ v(x,y,z,t;Re) \\ w(x,y,z,t;Re) \\ p(x,y,z,t;Re) \end{bmatrix} \sim \begin{bmatrix} \overline{\mathcal{U}}_0(\mathcal{Y},z) \\ \bar{a}\tilde{\Delta}\overline{\mathcal{V}}_3(\mathcal{Y},z) \\ \bar{a}\,\overline{\mathcal{W}}_2(\mathcal{Y},z) \\ \bar{a}^2\overline{\mathcal{P}}_4(\mathcal{Y},z) \end{bmatrix} + a'\mathcal{A} \begin{bmatrix} \hat{\mathcal{U}}_3(\mathcal{Y};z) \\ \hat{\mathcal{V}}_3(\mathcal{Y};z) \\ \hat{\mathcal{W}}_3(\mathcal{Y};z) \\ \hat{\mathcal{P}}_3(\mathcal{Y};z) \end{bmatrix} A(z)\mathrm{e}^{i\left[\alpha(x-ct)+\theta(z/\tilde{\Delta})\right]} + c.c. \tag{2.21}$$

where $c.c.$ denotes complex conjugate. In these expansions, the fluctuations, which have a to-be-determined asymptotic size $a'(Re)$ and $O(1)$ z-varying amplitude $\mathcal{A}A(z)$, are represented using a WKBJ approximation in which the fast phase $\theta(z/\tilde{\Delta}) \equiv \Theta(z)/\tilde{\Delta}$, and the rescaled spanwise wavenumber $\tilde{\beta} \equiv \partial_z\Theta = O(1)$. We also define the $O(1)$ streamwise wavenumber $\tilde{\alpha} = \alpha\tilde{\Delta}$ and, for subsequent reference, note that $\breve{\alpha} = \tilde{\alpha}\bar{\Omega}_c^{1/4}$, i.e. the $O(1)$ streamwise wavenumber scaled by Δ rather than by $\tilde{\Delta}$. The $O(1)$ phase speed c is strictly real for neutral Rayleigh modes implicated in a steady SSP and vanishes only for the VF at $y = 0$. Although the real scalar $\mathcal{A}$ could be absorbed into the definition of the amplitude function $A(z)$, it proves convenient to explicitly retain this factor as a control parameter. (That is, we take $\mathcal{A}$ and the rescaled, $O(1)$ streamwise wavenumber $\breve{\alpha}$ as control parameters for the Rayleigh mode and self-consistently determine the slowly-varying spanwise wavenumber $\tilde{\beta}(z)$ and amplitude function $A(z)$.) To disentangle $\mathcal{A}$ from $A(z)$, we normalize the latter such that $A(0) = 1$. An additional normalization condition will be specified below to distinguish the $\mathcal{Y}$- and z-varying eigenfunction from the amplitude, thereby rendering the decomposition of the fluctuation fields in (2.21) unique.

The scaling of the mean streamwise and spanwise velocity components in (2.21) ensures smooth matching with the flow in the adjacent UMZs is possible, while the scaling of the mean fissure-normal velocity follows from incompressibility. In the proposed configuration, no physical (i.e. no-slip) boundary exists along the horizontal planes separating rows of stacked counter-rotating rolls. Consequently, the leading-order mean spanwise velocity component within the VF is not sheared; i.e. $\partial_{\mathcal{Y}}\overline{\mathcal{W}}_2 = 0$, hence $\overline{\mathcal{W}}_2 = \overline{\mathcal{W}}_2(z)$, only. Through the mean incompressibility

condition, this ansatz implies that within the fissure $\overline{\mathcal{V}}_3(\mathcal{Y}, z)$ varies linearly with the normal coordinate $\mathcal{Y}$. A second immediate consequence is that the roll vorticity will have the same asymptotic size, namely $O(\bar{a})$, within the VF and adjacent UMZs, ensuring smooth matching of this field is possible. To close the global vorticity budget, however, a $\mathcal{Y}$-dependent correction $\bar{a}\tilde{\Delta}\overline{\mathcal{W}}_3(\mathcal{Y}, z)$ must be appended to the expansion for the mean spanwise velocity component in (2.21); see Harper (1963). Finally, in contrast to the mean fields, the fluctuations are isotropic within the fissure and thus each fluctuation field has the same asymptotic size a'. (We find that $a' \leq \bar{a}$ as $Re \to \infty$ for sensible physical balances to be realized in the mean equations.) Recalling that the streamwise wavelength of the fluctuation fields is commensurate with $\tilde{\Delta}$, the VF thickness, the fluctuations consequently decay exponentially away from the center of the fissure.

2.3.1 Viscous Mean Dynamics: Childress Cell Problem

Substituting (2.21) into the incompressibility condition and the NS equations, applying the streamwise/fast-phase averaging operation and collecting terms at leading order in $\tilde{\Delta}$ yields

$$\partial_{\mathcal{Y}}\tilde{\mathcal{V}}_3 + \partial_z\tilde{\mathcal{W}}_2 = 0, \tag{2.22}$$

$$\tilde{\mathcal{V}}_3\partial_{\mathcal{Y}}\overline{\mathcal{U}}_0 + \tilde{\mathcal{W}}_2\partial_z\overline{\mathcal{U}}_0 = \partial_{\mathcal{Y}}^2\overline{\mathcal{U}}_0, \tag{2.23}$$

$$\partial_{\mathcal{Y}}\tilde{\mathcal{P}}_4 = 0, \tag{2.24}$$

$$\tilde{\mathcal{W}}_2\partial_z\tilde{\mathcal{W}}_2 = -\partial_z\tilde{\mathcal{P}}_4, \tag{2.25}$$

$$\tilde{\mathcal{V}}_3\partial_{\mathcal{Y}}\left(\partial_{\mathcal{Y}}\tilde{\mathcal{W}}_3\right) + \tilde{\mathcal{W}}_2\partial_z\left(\partial_{\mathcal{Y}}\tilde{\mathcal{W}}_3\right) = -\frac{\partial_{\mathcal{Y}}^2\left(\overline{\mathcal{V}_3'\mathcal{W}_3'}\right)}{\bar{\Omega}_c^2} + \partial_{\mathcal{Y}}^2\left(\partial_{\mathcal{Y}}\tilde{\mathcal{W}}_3\right), \tag{2.26}$$

where $(\overline{\mathcal{V}}_3, \overline{\mathcal{W}}_{2,3}) = \bar{\Omega}_c(\tilde{\mathcal{V}}_3, \tilde{\mathcal{W}}_{2,3})$ and $\overline{\mathcal{P}}_4 = \bar{\Omega}_c^2\tilde{\mathcal{P}}_4$. The key simplification to the mean flow equations in this region is that asymptotic matching enables the leading-order roll flow $(\tilde{\mathcal{V}}_3, \tilde{\mathcal{W}}_2)$ to be obtained by extrapolating the UMZ roll solution to the VF. Specifically, the tangential component of the roll flow within the fissure is obtained simply by evaluating (2.18) at $y = 0$. Using the incompressiblity constraint (2.22) and the symmetry condition $\tilde{\mathcal{V}}_3(\mathcal{Y} = 0, z) = 0$ to determine a constant of integration, the normal flow component $\tilde{\mathcal{V}}_3$ also can be determined, yielding

$$\tilde{\mathcal{V}}_3(\mathcal{Y},z) = -\mathcal{Y}\sum_{n=1,odd}^{\infty}\left(\frac{4}{n\pi}\right)\tanh\left(\frac{n\pi}{L_z}\right)\cos\left(\frac{2n\pi z}{L_z}\right), \tag{2.27}$$

$$\tilde{w}_2(y=0,z) = \tilde{\mathcal{W}}_2(z) = \sum_{n=1,odd}^{\infty}\left(\frac{2L_z}{(n\pi)^2}\right)\tanh\left(\frac{n\pi}{L_z}\right)\sin\left(\frac{2n\pi z}{L_z}\right). \tag{2.28}$$

The leading-order roll flow within the VF, (2.27)–(2.28), satisfies the mean equations (2.22), (2.24) and (2.25), with $\tilde{\mathcal{P}}_4(z) = \tilde{p}_4(y{=}0,z)$ for matching with the adjacent UMZs.

Given (2.27)–(2.28), the ($\perp$) velocity field that advects the leading-order streak flow ($\overline{\mathcal{U}}_0$) and x-vorticity ($\partial_{\mathcal{Y}}\tilde{\mathcal{W}}_3$) within the fissure is known, and the equations for these fields effectively linearize. Analogous considerations apply to the viscous jet regions around the remainder of the roll-cell periphery. By choosing to scale $a' = \tilde{\Delta}\overline{a}$, the torque provided by the gradient of the fluctuation-induced Reynolds stress divergence $-\partial_{\mathcal{Y}}(\overline{\mathcal{V}_3'\mathcal{W}_3'})$ arises consistently in (2.26) and seemingly has the potential to drive x-vorticity within the VF and, thence, roll motions within the UMZ. Subsequently, however, it is confirmed that $\mathcal{V}_3'$ and $\mathcal{W}_3'$ are out of phase for a (3D) neutral Rayleigh mode. Consequently, this correlation vanishes and no driving of the rolls is realized. Instead, as in VWI theory, the driving to sustain the roll motions arises from a critical-layer phenomenon (see section 2.4 and section 2.5).

The vorticity equation (2.26) must be solved subject to the matching condition $\partial_{\mathcal{Y}}\tilde{\mathcal{W}}_3 \to -1$ as $\mathcal{Y} \to \infty$ (e.g. for matching with the upper UMZ over $0 \le z \le L_z/2$). The appropriate boundary condition for this vorticity component as $\mathcal{Y} \to 0^+$ is not obvious *a priori*, but will be determined in section 2.4. Indeed, in the absence of driving from the Reynolds stress term in (2.26), this boundary condition will be shown to give rise to the forcing that sustains the rolls, revealing that the CL plays a key role in maintaining the staircase-like profile of streamwise velocity in the proposed asymptotic SSP.

The mean streamwise momentum equation (2.23) must be solved subject to the symmetry conditions $\overline{\mathcal{U}}_0 \to 1/2$ as $\mathcal{Y} \to \infty$ (for the UMZ located in $0 < y < 1$) and $\overline{\mathcal{U}}_0 \to 0$ as $\mathcal{Y} \to 0$. Identical equations and boundary conditions apply within the VF centered on $y = 1$ upon replacing $\tilde{\Delta}\mathcal{Y} \to 1 - \tilde{\Delta}\mathcal{Y}$ and $z \to L_z/2 - z$. The same steady advection–diffusion equation

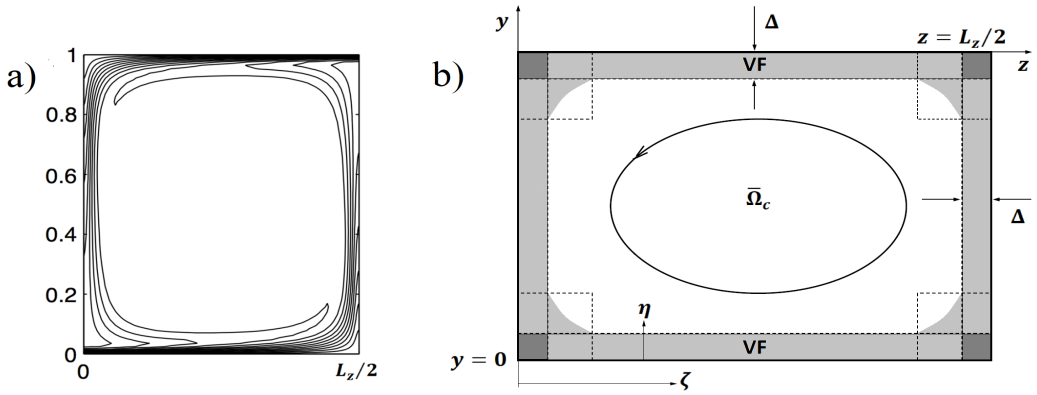

Figure 2.4: Formulation of Childress cell problem, as adapted from Chini & Cox (2009). (a) Contour plot of $\overline{u}_0(y,z)$. (b) Corresponding multi-region asymptotic structure of a steady roll cell as $Re \to \infty$. The white region is the dynamically inviscid vortex core. The light grey regions indicate the $O(\Delta)$ thick VFs as well as $O(\Delta)$ thick positive and negative streamwise jets. The streamwise-averaged streamwise velocity is passively advected through the outer corner regions also indicated by the light grey shading. (The viscous inner corner regions highlighted in dark grey also are dynamically passive.) ζ is a stretched arc-length coordinate running around the cell perimeter, and η is a scaled coordinate measuring distance normal to the VFs and jets.

also applies within the streamwise jets centered on $z = 0$ and $z = L_z/2$, with the roles of y and z (and $\tilde{\mathcal{V}}_3$ and $\tilde{\mathcal{W}}_2$) interchanged. The resulting problem for $\overline{\mathcal{U}}_0$ is formally identical to that for the temperature field in steady 2D Rayleigh-Bénard convection (RBC) in the limit of asymptotically large Rayleigh number. This observation provides an interesting and potentially useful connection between coherent structures arising in strongly nonlinear convection and wall-bounded shear flows. (Of course, in RBC, the cellular flow is driven by buoyancy torques acting within vertical plumes, while in the proposed SSP, the roll flow is driven by Reynolds stresses arising from the nonlinear interaction of a streamwise-varying shear instability mode confined to the horizontal fissures.) As demonstrated in Chini & Cox (2009), the advected and diffused scalar field can be determined by formulating a *Childress cell problem*, in which the fissures and jets (or thermal boundary layers and plumes in the RBC context) around each cell are stitched together to form a connected domain wherein $\overline{\mathcal{U}}_0$ is governed by the single equation

$$\tilde{\mathcal{V}}_N \partial_{\mathcal{N}} \overline{\mathcal{U}}_0 + \tilde{\mathcal{V}}_s \partial_s \overline{\mathcal{U}}_0 = \partial_{\mathcal{N}}^2 \overline{\mathcal{U}}_0; \tag{2.29}$$

see figure 2.4. Here, $\mathcal{N}$ and s are coordinates normal to and tangent to the cell boundary; within the VF centered at $y = 0$, for example, these coordinates are equal to $\mathcal{Y}$ and z, respectively. The required suturing exploits the fact that the scalar field is merely passively advected through each corner region.

By making a suitable change of variables, $\overline{\mathcal{U}}_0(s, \mathcal{N}) = \overline{\mathrm{U}}(\zeta, \eta)$, with the so-called Crocco or Von Mises coordinates

$$\zeta = \int_0^s \tilde{\mathcal{V}}_s(\hat{s}) d\hat{s}, \quad \eta = \frac{1}{2} \int_0^{\mathcal{N}} \tilde{\mathcal{V}}_s(s) d\hat{\mathcal{N}}, \tag{2.30}$$

the advection-diffusion equation (2.29) can be transformed into the diffusion equation

$$\partial_\zeta \overline{\mathrm{U}} = \frac{1}{4} \partial_\eta^2 \overline{\mathrm{U}}. \tag{2.31}$$

Equation (2.31) is solved subject to the boundary conditions

$$\begin{aligned}
\overline{\mathrm{U}}(\zeta, 0) &= 0 \text{ on } 0 < \zeta < l_1, && (2.32)\\
\partial_\eta \overline{\mathrm{U}}(\zeta, 0) &= 0 \text{ on } l_1 < \zeta < l_2, && (2.33)\\
\overline{\mathrm{U}}(\zeta, 0) &= 1 \text{ on } l_2 < \zeta < (2l_1 + l_2), && (2.34)\\
\partial_\eta \overline{\mathrm{U}}(\zeta, 0) &= 0 \text{ on } (2l_1 + l_2) < \zeta < L \equiv 2(l_1 + l_2), && (2.35)
\end{aligned}$$

where l_1 and l_2 are the lengths of the fissure-parallel and fissure-normal cell edges, respectively, measured in the coordinate ζ, and subject to the periodicity condition

$$\overline{\mathrm{U}}(\zeta + nL, \eta) = \overline{\mathrm{U}}(\zeta, \eta), \qquad n = 1, 2, 3, \cdots \tag{2.36}$$

in the time-like coordinate ζ. As first shown by Jiménez & Zufiria (1987), exploiting this periodicity requirement enables the formal solution of the Childress cell problem to be expressed as

$$\overline{\mathrm{U}}(\zeta, \eta) = \frac{\eta}{\sqrt{\pi}} \int_0^\infty \frac{\mathrm{U}_w(\zeta - p)}{p^{3/2}} e^{-\eta^2/p} dp. \tag{2.37}$$

An integral equation for the unknown function $\mathrm{U}_w(\zeta) \equiv \overline{\mathrm{U}}(\zeta, \eta = 0)$ arising in the integrand of (2.37) is obtained by setting $\partial_\eta \overline{\mathrm{U}}(\zeta, 0) = 0$ on the two fissure-normal cell edges. Accurate numerical solution of the resulting integral equation requires careful treatment of the singular behavior of $\overline{\mathrm{U}}$ in the corner regions and specialized acceleration techniques to evaluate numerous slowly converging infinite summations; see Chini & Cox (2009) for details. Here, we simply lift the key results from their investigation. In particular, solution of the Childress cell problem yields the shear $\tilde{\lambda}(z) \equiv \partial_{\mathcal{Y}} \overline{\mathcal{U}}_0(\mathcal{Y} = 0, z)$ induced by the mean streamwise velocity component at the center of the fissure.

2.3.2 Inviscid Fluctuation Dynamics: Rayleigh, Eikonal and Amplitude Equations

Recalling the WKBJ ansatz in (2.21), the leading-order equations for the fluctuation fields within the VF are

$$
\begin{aligned}
i\tilde{\alpha}\hat{\mathcal{U}}_3 + \partial_{\mathcal{Y}}\hat{\mathcal{V}}_3 + i\tilde{\beta}\hat{\mathcal{W}}_3 &= 0, && (2.38)\\
i\tilde{\alpha}\left(\overline{\mathcal{U}}_0 - c\right)\hat{\mathcal{U}}_3 + \hat{\mathcal{V}}_3\partial_{\mathcal{Y}}\overline{\mathcal{U}}_0 + i\tilde{\alpha}\hat{\mathcal{P}}_3 &= 0, && (2.39)\\
i\tilde{\alpha}\left(\overline{\mathcal{U}}_0 - c\right)\hat{\mathcal{V}}_3 + \partial_{\mathcal{Y}}\hat{\mathcal{P}}_3 &= 0, && (2.40)\\
i\tilde{\alpha}\left(\overline{\mathcal{U}}_0 - c\right)\hat{\mathcal{W}}_3 + i\tilde{\beta}\hat{\mathcal{P}}_3 &= 0. && (2.41)
\end{aligned}
$$

From (2.38)–(2.41), it can be deduced that $\hat{\mathcal{V}}_3$ and $\hat{\mathcal{W}}_3$ are $\pi/2$ out of phase, confirming that the correlation $\overline{\mathcal{V}_3'\mathcal{W}_3'} = 0$ in (2.26). A crucial aspect of this leading-order system is that the fluctuations satisfy 'quasilinear' equations with respect to the leading-order streak velocity. One consequence is that Squire's transformation can be use to reduce (2.38)–(2.41) to a 2D system. Specifically, adding $\tilde{\alpha}$x(2.39) to $\tilde{\beta}$x(2.41) and dividing the sum by $\tilde{\alpha}$ yields

$$
\begin{aligned}
i\tilde{k}\hat{\mathcal{U}}_{3r} + \partial_{\mathcal{Y}}\hat{\mathcal{V}}_3 &= 0, && (2.42)\\
i\tilde{k}\left(\overline{\mathcal{U}}_0 - c\right)\hat{\mathcal{U}}_{3r} + \hat{\mathcal{V}}_3\partial_{\mathcal{Y}}\overline{\mathcal{U}}_0 + i\tilde{k}\hat{\Pi}_3 &= 0, && (2.43)\\
i\tilde{k}\left(\overline{\mathcal{U}}_0 - c\right)\hat{\mathcal{V}}_3 + \partial_{\mathcal{Y}}\hat{\Pi}_3 &= 0, && (2.44)
\end{aligned}
$$

along with a decoupled, but important equation for $\hat{\mathcal{W}}_{3r}$,

$$\hat{\mathcal{W}}_{3r} = \frac{1}{i\tilde{k}}\frac{\tilde{\beta}}{\tilde{\alpha}}\frac{\hat{\mathcal{V}}_3 \partial_{\mathcal{Y}} \overline{\mathcal{U}}_0}{\overline{\mathcal{U}}_0 - c}, \tag{2.45}$$

where

$$\begin{aligned} \tilde{k} = \sqrt{\tilde{\alpha}^2 + \tilde{\beta}^2}, \qquad & \tilde{k}\hat{\mathcal{P}}_3 = \tilde{\alpha}\hat{\Pi}_3, \\ \tilde{k}\hat{\mathcal{U}}_{3r} = \tilde{\alpha}\hat{\mathcal{U}}_3 + \tilde{\beta}\hat{\mathcal{W}}_3 \qquad \Longleftrightarrow \qquad & \tilde{k}\hat{\mathcal{U}}_3 = \tilde{\alpha}\hat{\mathcal{U}}_{3r} - \tilde{\beta}\hat{\mathcal{W}}_{3r}, \\ \tilde{k}\hat{\mathcal{W}}_{3r} = \tilde{\alpha}\hat{\mathcal{W}}_3 - \tilde{\beta}\hat{\mathcal{U}}_3 \qquad \Longleftrightarrow \qquad & \tilde{k}\hat{\mathcal{W}}_3 = \tilde{\beta}\hat{\mathcal{U}}_{3r} + \tilde{\alpha}\hat{\mathcal{W}}_{3r}. \end{aligned} \tag{2.46}$$

The equation relating $\tilde{k}$ to $\tilde{\alpha}$ and $\tilde{\beta}$ in 2.46 is the *Eikonal equation*. The horizontal wavenumber $\tilde{k}$ is a function of $\tilde{\lambda}$, hence the Eikonal equation relates the specified streamwise wavenumber, the slowly-varying spanwise wavenumber, and thickness of the shear layer itself. Using a streamfunction (ϕ) and vorticity formulation to eliminate the fluctuation pressure, (2.42)–(2.44) can be further simplified, yielding

$$\partial^2_{\mathcal{Y}}\phi - \frac{\partial^2_{\mathcal{Y}}\overline{\mathcal{U}}_0}{\left(\overline{\mathcal{U}}_0 - c\right)}\phi = \tilde{k}^2\phi, \tag{2.47}$$

where $\hat{\mathcal{V}}_3 = -i\phi$ and $\hat{\mathcal{U}}_{3r} = \partial_{\mathcal{Y}}\phi/\tilde{k}$.

Equation (2.47) is Rayleigh's stability equation, albeit here with a base flow $\overline{\mathcal{U}}_0$ that depends parametrically on the spanwise coordinate z. Since a neutral mode is sought and the associated wave phase speed is set by symmetry considerations (i.e. $c = n$ for the VF centered at $y = n$, where $n = 0, \pm 1, \pm 2 \ldots$), the total horizontal wavenumber $\tilde{k}^2$ may be taken as the eigenvalue. Once $\tilde{k}^2$ is determined, the spanwise wavenumber $\tilde{\beta}$ may be evaluated. Note that this 1D eigenvalue problem must be solved over the domain $z \in [-L_z/2, L_z/2]$, since the streak field $\overline{\mathcal{U}}_0$ varies (slowly) with z. The shape of the resulting neutral mode is given by the eigenfuction. To determine the slowly z-varying amplitude, however, the fluctuation equations must be analyzed at higher order.

In analogy with (2.21), the following ansatz is made for the higher-order fluctuation fields:

$$\begin{bmatrix} \mathcal{U}_4' \\ \mathcal{V}_4' \\ \mathcal{W}_4' \\ \mathcal{P}_4' \end{bmatrix} = B(x,z) \begin{bmatrix} \hat{\mathcal{U}}_4(\mathcal{Y};z) \\ \hat{\mathcal{V}}_4(\mathcal{Y};z) \\ \hat{\mathcal{W}}_4(\mathcal{Y};z) \\ \hat{\mathcal{P}}_4(\mathcal{Y};z) \end{bmatrix} \mathrm{e}^{i\left[\alpha(x-ct)+\theta(z/\tilde{\Delta})\right]} + c.c.,$$

where $B(x,z)$ is the $x-$ and z-varying amplitude of the $O(\tilde{\Delta}^4)$ fluctuation field. Collecting terms at the next order in $\tilde{\Delta}$ yields

$$\begin{aligned} B\left[i\tilde{\alpha}\hat{\mathcal{U}}_4 + \partial_{\mathcal{Y}}\hat{\mathcal{V}}_4 + i\tilde{\beta}\hat{\mathcal{W}}_4\right] &= -(\partial_x A)\hat{\mathcal{U}}_3 - \partial_z(A\hat{\mathcal{W}}_3), && (2.48)\\ B\left[i\tilde{\alpha}\left(\overline{\mathcal{U}}_0 - c\right)\hat{\mathcal{U}}_4 + \hat{\mathcal{V}}_4\partial_{\mathcal{Y}}\overline{\mathcal{U}}_0 + i\tilde{\alpha}\hat{\mathcal{P}}_4\right] &= -(i\tilde{\alpha})\overline{\mathcal{U}}_1 A\hat{\mathcal{U}}_3 - \overline{\mathcal{U}}_0(\partial_x A)\hat{\mathcal{U}}_3 \\ -A\hat{\mathcal{V}}_3\partial_{\mathcal{Y}}\overline{\mathcal{U}}_1 &- (\partial_x A)\hat{\mathcal{P}}_3 - A\hat{\mathcal{W}}_3\partial_z\overline{\mathcal{U}}_0, && (2.49)\\ B\left[i\tilde{\alpha}\left(\overline{\mathcal{U}}_0 - c\right)\hat{\mathcal{V}}_4 + \partial_{\mathcal{Y}}\hat{\mathcal{P}}_4\right] &= -(i\tilde{\alpha})\overline{\mathcal{U}}_1 A\hat{\mathcal{V}}_3 - \overline{\mathcal{U}}_0(\partial_x A)\hat{\mathcal{V}}_3, && (2.50)\\ B\left[i\tilde{\alpha}\left(\overline{\mathcal{U}}_0 - c\right)\hat{\mathcal{W}}_4 + i\tilde{\beta}\hat{\mathcal{P}}_4\right] &= -(i\tilde{\alpha})\overline{\mathcal{U}}_1 A\hat{\mathcal{W}}_3 - \overline{\mathcal{U}}_0(\partial_X A)\hat{\mathcal{W}}_3 - \partial_z(A\hat{\mathcal{P}}_3) && (2.51)\end{aligned}$$

As for the leading-order fluctuation equations, it proves advantageous to apply Squire's transformation to (2.48)–(2.51). Multiplying (2.49) by $\tilde{\alpha}/\tilde{\alpha}$ and (2.51) by $\tilde{\beta}/\tilde{\alpha}$ yields

$$\begin{aligned} B\left[i\tilde{\alpha}\left(\overline{\mathcal{U}}_0 - c\right)\hat{\mathcal{U}}_4 + \hat{\mathcal{V}}_4\partial_{\mathcal{Y}}\overline{\mathcal{U}}_0 + i\tilde{\alpha}^2\left(\frac{\hat{\mathcal{P}}_4}{\tilde{\alpha}}\right)\right] &= -\overline{\mathcal{U}}_0(\partial_x A)\frac{\tilde{\alpha}}{\tilde{\alpha}}\hat{\mathcal{U}}_3 - i\overline{\mathcal{U}}_1 A(\tilde{\alpha}\hat{\mathcal{U}}_3) \\ -A\hat{\mathcal{V}}_3\partial_{\mathcal{Y}}\overline{\mathcal{U}}_1 - \tilde{\alpha}(\partial_x A)\frac{\hat{\mathcal{P}}_3}{\tilde{\alpha}} &- A\hat{\mathcal{W}}_3\partial_z\overline{\mathcal{U}}_0, && (2.52)\\ B\left[i\tilde{\beta}\left(\overline{\mathcal{U}}_0 - c\right)\hat{\mathcal{W}}_4 + i\tilde{\beta}^2\left(\frac{\hat{\mathcal{P}}_4}{\tilde{\alpha}}\right)\right] &= -i\overline{\mathcal{U}}_1 A(\tilde{\beta}\hat{\mathcal{W}}_3) \\ -\overline{\mathcal{U}}_0(\partial_x A)\frac{\tilde{\beta}}{\tilde{\alpha}}\hat{\mathcal{W}}_3 &- \tilde{\beta}\partial_z\left(\frac{A\hat{\mathcal{P}}_3}{\tilde{\alpha}}\right). && (2.53)\end{aligned}$$

We define the rotated velocity fields $\hat{\mathcal{U}}_{4r}$ and $\hat{\mathcal{W}}_{4r}$ and rescaled pressure $\hat{\Pi}_4$ as

$$\hat{\mathcal{U}}_{4r} \equiv \frac{\tilde{\alpha}\hat{\mathcal{U}}_4 + \tilde{\beta}\hat{\mathcal{W}}_4}{\sqrt{\tilde{\alpha}^2 + \tilde{\beta}^2}}, \tag{2.54}$$

$$\hat{\mathcal{W}}_{4r} \equiv \frac{1}{i\tilde{k}}\frac{\tilde{\beta}}{\tilde{\alpha}}\frac{\hat{\mathcal{V}}_4 \partial_y \overline{\mathcal{U}}_0}{\overline{\mathcal{U}}_0 - c}, \tag{2.55}$$

$$\hat{\Pi}_4 \equiv \frac{\tilde{k}}{\tilde{\alpha}}\hat{\mathcal{P}}_4. \tag{2.56}$$

Here, for generality of the exposition, we also allow B (and consequently A) to depend on the original x coordinate, although, ultimately, this x-dependence of the amplitudes is suppressed. Adding (2.52) to (2.53) and using the definitions (2.54)-(2.56) yields the rotated form of the incompressibility and momentum equations:

$$B\Big[i\tilde{k}\hat{\mathcal{U}}_{4r} + \partial_y \hat{\mathcal{V}}_4\Big] = -(\partial_x A)\Big[\frac{\tilde{\alpha}}{\tilde{k}}\hat{\mathcal{U}}_{3r} - \frac{\tilde{\beta}}{\tilde{k}}\hat{\mathcal{W}}_{3r}\Big] - \partial_z\left(A\Big[\frac{\tilde{\beta}}{\tilde{k}}\hat{\mathcal{U}}_{3r} + \frac{\tilde{\alpha}}{\tilde{k}}\hat{\mathcal{W}}_{3r}\Big]\right), \tag{2.57}$$

$$\begin{aligned} B\Big[i\tilde{k}\left(\overline{\mathcal{U}}_0 - c\right)\hat{\mathcal{U}}_{4r} + \hat{\mathcal{V}}_4\partial_y\overline{\mathcal{U}}_0 + i\tilde{k}\hat{\Pi}_4\Big] &= -(i\tilde{k})\overline{\mathcal{U}}_1 A\hat{\mathcal{U}}_{3r} - \overline{\mathcal{U}}_0\frac{\tilde{k}}{\tilde{\alpha}}(\partial_x A)\hat{\mathcal{U}}_{3r} - A\hat{\mathcal{V}}_3\partial_y\overline{\mathcal{U}}_1 \\ &\quad -\frac{\tilde{\alpha}}{\tilde{k}}(\partial_x A)\hat{\Pi}_3 - \tilde{\beta}\partial_z\left(\frac{A\hat{\Pi}_3}{\tilde{k}}\right) - A\Big[\frac{\tilde{\beta}}{\tilde{k}}\hat{\mathcal{U}}_{3r} + \frac{\tilde{\alpha}}{\tilde{k}}\hat{\mathcal{W}}_{3r}\Big]\partial_z\overline{\mathcal{U}}_0, \end{aligned} \tag{2.58}$$

$$B\Big[i\tilde{k}\left(\overline{\mathcal{U}}_0 - c\right)\hat{\mathcal{V}}_4 + \partial_y\hat{\Pi}_4\Big] = -(i\tilde{k})\overline{\mathcal{U}}_1 A\hat{\mathcal{V}}_3 - \overline{\mathcal{U}}_0\frac{\tilde{k}}{\tilde{\alpha}}(\partial_x A)\hat{\mathcal{V}}_3. \tag{2.59}$$

The correction to the fluctuation vorticity in the rotated coordinate system is

$$\hat{\omega}_4 \equiv (i\tilde{k})\hat{\mathcal{V}}_4 - \partial_y\hat{\mathcal{U}}_{4r}. \tag{2.60}$$

To form a Rayleigh-like equation from (2.58)–(2.59), we begin by taking ∂_y of the rotated x-momentum equation and multiplying the y-momentum equation by $i\tilde{k}$,

$$
\begin{aligned}
&B\Big[i\tilde{k}(\partial_y\overline{\mathcal{U}}_0)\hat{\mathcal{U}}_{4r} + i\tilde{k}(\overline{\mathcal{U}}_0 - c)\partial_y\hat{\mathcal{U}}_{4r} + \partial_y\hat{\mathcal{V}}_4\partial_y\overline{\mathcal{U}}_0 + \hat{\mathcal{V}}_4\partial_y^2\overline{\mathcal{U}}_0 + i\tilde{k}\partial_y\hat{\Pi}_4\Big] = \\
&\quad -i\tilde{k}(\partial_y\overline{\mathcal{U}}_1)\hat{\mathcal{U}}_{3r}A - i\tilde{k}\overline{\mathcal{U}}_1(\partial_y\hat{\mathcal{U}}_{3r})A - \frac{\tilde{k}}{\tilde{\alpha}}(\partial_y\overline{\mathcal{U}}_0)\hat{\mathcal{U}}_{3r}\partial_x A \\
&\quad -\frac{\tilde{k}}{\tilde{\alpha}}\overline{\mathcal{U}}_0(\partial_y\hat{\mathcal{U}}_{3r})\partial_x A - \partial_y\hat{\mathcal{V}}_3(\partial_y\overline{\mathcal{U}}_1)A - \hat{\mathcal{V}}_3(\partial_y^2\overline{\mathcal{U}}_1)A - \frac{\tilde{\alpha}}{\tilde{k}}\partial_y\hat{\Pi}_3\partial_x A - \tilde{\beta}\partial_z\left(\frac{A\partial_y\hat{\Pi}_3}{\tilde{k}}\right) \\
&\quad -\partial_z\overline{\mathcal{U}}_0\partial_y\left(\frac{\tilde{\beta}}{\tilde{k}}\hat{\mathcal{U}}_{3r} + \frac{\tilde{\alpha}}{\tilde{k}}\hat{\mathcal{W}}_{3r}\right)A - \partial_z(\partial_y\overline{\mathcal{U}}_0)\left[\frac{\tilde{\beta}}{\tilde{k}}\hat{\mathcal{U}}_{3r} + \frac{\tilde{\alpha}}{\tilde{k}}\hat{\mathcal{W}}_{3r}\right]A, \qquad (2.61)
\end{aligned}
$$

$$
B\Big[i\tilde{k}(\overline{\mathcal{U}}_0 - c)i\tilde{k}\hat{\mathcal{V}}_4 + i\tilde{k}\,\partial_y\hat{\Pi}_4\Big] = -(i\tilde{k})\overline{\mathcal{U}}_1 i\tilde{k}\hat{\mathcal{V}}_3 A - \overline{\mathcal{U}}_0\frac{\tilde{k}}{\tilde{\alpha}}i\tilde{k}\hat{\mathcal{V}}_3\partial_x A. \qquad (2.62)
$$

Subtracting equation (2.62) from (2.61) to eliminate the pressure term yields

$$
\begin{aligned}
&B\Big[i\tilde{k}(\overline{\mathcal{U}}_0 - c)(i\tilde{k}\hat{\mathcal{V}}_4 - \partial_y\hat{\mathcal{U}}_{4r}) - (i\tilde{k}\hat{\mathcal{U}}_{4r} + \partial_y\hat{\mathcal{V}}_4)(\partial_y\overline{\mathcal{U}}_0) - \hat{\mathcal{V}}_4\partial_y^2\overline{\mathcal{U}}_0\Big] = \\
&\quad - i\tilde{k}(i\tilde{k}\hat{\mathcal{V}}_3 - \partial_y\hat{\mathcal{U}}_{3r})\overline{\mathcal{U}}_1 A - \frac{\tilde{k}}{\tilde{\alpha}}(i\tilde{k}\hat{\mathcal{V}}_3 - \partial_y\hat{\mathcal{U}}_{3r})\overline{\mathcal{U}}_0\partial_x A \\
&\quad + \frac{\tilde{k}}{\tilde{\alpha}}\hat{\mathcal{U}}_{3r}\partial_y\overline{\mathcal{U}}_0\partial_x A + i\tilde{k}\hat{\mathcal{U}}_{3r}(\partial_y\overline{\mathcal{U}}_1)A + \partial_y\hat{\mathcal{V}}_3(\partial_y\overline{\mathcal{U}}_1)A \\
&\quad + \hat{\mathcal{V}}_3(\partial_y^2\overline{\mathcal{U}}_1)A + \frac{\tilde{\alpha}}{\tilde{k}}\partial_y\hat{\Pi}_3\partial_x A + \tilde{\beta}\partial_z\left(\frac{A\partial_y\hat{\Pi}_3}{\tilde{k}}\right) + \partial_z\overline{\mathcal{U}}_0\partial_y\left(\frac{\tilde{\beta}}{\tilde{k}}\hat{\mathcal{U}}_{3r} + \frac{\tilde{\alpha}}{\tilde{k}}\hat{\mathcal{W}}_{3r}\right)A \\
&\quad + \partial_z(\partial_y\overline{\mathcal{U}}_0)\left[\frac{\tilde{\beta}}{\tilde{k}}\hat{\mathcal{U}}_{3r} + \frac{\tilde{\alpha}}{\tilde{k}}\hat{\mathcal{W}}_{3r}\right]A.
\end{aligned} \qquad (2.63)
$$

Finally, after substituting the incompressibility condition (2.57), we obtain

$$
\begin{aligned}
&B[(\overline{\mathcal{U}}_0 - c)(-\tilde{k}^2\hat{\mathcal{V}}_4 - i\tilde{k}\partial_y\hat{\mathcal{U}}_{4r}) - \hat{\mathcal{V}}_4\partial_y^2\overline{\mathcal{U}}_0] = \\
&\quad - i\tilde{k}(i\tilde{k}\hat{\mathcal{V}}_3 - \partial_y\hat{\mathcal{U}}_{3r})\overline{\mathcal{U}}_1 A - \frac{\tilde{k}}{\tilde{\alpha}}(i\tilde{k}\hat{\mathcal{V}}_3 - \partial_y\hat{\mathcal{U}}_{3r})\overline{\mathcal{U}}_0\partial_x A \\
&\quad + \frac{\tilde{k}}{\tilde{\alpha}}\hat{\mathcal{U}}_{3r}(\partial_y\overline{\mathcal{U}}_0)\partial_x A + i\tilde{k}\hat{\mathcal{U}}_{3r}(\partial_y\overline{\mathcal{U}}_1)A + \partial_y\hat{\mathcal{V}}_3(\partial_y\overline{\mathcal{U}}_1)A \\
&\quad + \hat{\mathcal{V}}_3(\partial_y^2\overline{\mathcal{U}}_1)A + \frac{\tilde{\alpha}}{\tilde{k}}\partial_y\hat{\Pi}_3\partial_x A + \tilde{\beta}\partial_z\left(\frac{A\partial_y\hat{\Pi}_3}{\tilde{k}}\right) + \partial_z\overline{\mathcal{U}}_0\partial_y\left(\frac{\tilde{\beta}}{\tilde{k}}\hat{\mathcal{U}}_{3r} + \frac{\tilde{\alpha}}{\tilde{k}}\hat{\mathcal{W}}_{3r}\right)A \\
&\quad + \partial_z(\partial_y\overline{\mathcal{U}}_0)\left[\frac{\tilde{\beta}}{\tilde{k}}\hat{\mathcal{U}}_{3r} + \frac{\tilde{\alpha}}{\tilde{k}}\hat{\mathcal{W}}_{3r}\right]A - \partial_y\overline{\mathcal{U}}_0\left[\frac{\tilde{\alpha}}{\tilde{k}}\hat{\mathcal{U}}_{3r} - \frac{\tilde{\beta}}{\tilde{k}}\hat{\mathcal{W}}_{3r}\right]\partial_x A \\
&\quad - \partial_y\overline{\mathcal{U}}_0\partial_z\left(A\left[\frac{\tilde{\beta}}{\tilde{k}}\hat{\mathcal{U}}_{3r} + \frac{\tilde{\alpha}}{\tilde{k}}\hat{\mathcal{W}}_{3r})\right]\right),
\end{aligned} \qquad (2.64)
$$

which together with (2.57) form a closed system of equations for $\hat{\mathcal{U}}_{4r}$ and $\hat{\mathcal{V}}_4$.

Further manipulation is required to obtain a single equation for $\hat{\mathcal{V}}_4$ involving the Rayleigh-equation linear operator. First, we observe that

$$\begin{aligned}
B[(\overline{\mathcal{U}}_0 - c)(-\tilde{k}^2\hat{\mathcal{V}}_4 - i\tilde{k}\partial_y\hat{\mathcal{U}}_{4r})] &= -B[(\overline{\mathcal{U}}_0 - c)\tilde{k}^2\hat{\mathcal{V}}_4] - (\overline{\mathcal{U}}_0 - c)\partial_y(Bi\tilde{k}\hat{\mathcal{U}}_{4r}) \\
&= - B[(\overline{\mathcal{U}}_0 - c)\tilde{k}^2\hat{\mathcal{V}}_4] - (\overline{\mathcal{U}}_0 - c)\partial_y\Bigg[(B\partial_y\hat{\mathcal{V}}_4) \\
&\quad + \left[\frac{\tilde{\alpha}}{\tilde{k}}\hat{\mathcal{U}}_{3r} - \frac{\tilde{\beta}}{\tilde{k}}\hat{\mathcal{W}}_{3r}\right]\partial_x A + \partial_z\left(A\left[\frac{\tilde{\beta}}{\tilde{k}}\hat{\mathcal{U}}_{3r} + \frac{\tilde{\alpha}}{\tilde{k}}\hat{\mathcal{W}}_{3r})\right]\right)\Bigg] \\
&= B\Big[(\overline{\mathcal{U}}_0 - c)(\partial_y^2\hat{\mathcal{V}}_4 - \tilde{k}^2\hat{\mathcal{V}}_4)\Big] + (\overline{\mathcal{U}}_0 - c)\Bigg[\partial_y\left(\frac{\tilde{\alpha}}{\tilde{k}}\hat{\mathcal{U}}_{3r} - \frac{\tilde{\beta}}{\tilde{k}}\hat{\mathcal{W}}_{3r}\right)\partial_x A \\
&\quad + \partial_z\left(A\partial_y\left(\frac{\tilde{\beta}}{\tilde{k}}\hat{\mathcal{U}}_{3r} + \frac{\tilde{\alpha}}{\tilde{k}}\hat{\mathcal{W}}_{3r})\right)\right)\Bigg].
\end{aligned} \tag{2.65}$$

We substitute (2.65) into (2.64) to remove the $\hat{\mathcal{U}}_{4r}$ term from the left-hand side. After reorganizing the right-hand side of the equation, the equation for $\hat{\mathcal{V}}_4$ becomes

$$\begin{aligned}
&B[(\overline{\mathcal{U}}_0 - c)(\partial_y\hat{\mathcal{V}}_4 - \tilde{k}^2\hat{\mathcal{V}}_4) - \partial_y^2\overline{\mathcal{U}}_0\hat{\mathcal{V}}_4] = \\
&\quad - \frac{\tilde{k}}{\tilde{\alpha}}(i\tilde{k}\hat{\mathcal{V}}_3 - \partial_y\hat{\mathcal{U}}_{3r})\overline{\mathcal{U}}_0\partial_x A + \frac{\tilde{k}}{\tilde{\alpha}}\hat{\mathcal{U}}_{3r}(\partial_y\overline{\mathcal{U}}_0)\partial_x A \\
&\quad + \frac{\tilde{\alpha}}{\tilde{k}}\partial_y\hat{\Pi}_3\partial_x A - (\overline{\mathcal{U}}_0 - c)\partial_y\left(\frac{\tilde{\alpha}}{\tilde{k}}\hat{\mathcal{U}}_{3r} - \frac{\tilde{\beta}}{\tilde{k}}\hat{\mathcal{W}}_{3r}\right)\partial_x A - \partial_y\overline{\mathcal{U}}_0\left[\frac{\tilde{\alpha}}{\tilde{k}}\hat{\mathcal{U}}_{3r} - \frac{\tilde{\beta}}{\tilde{k}}\hat{\mathcal{W}}_{3r}\right]\partial_x A \\
&\quad + \tilde{\beta}\partial_z\left(\frac{A\partial_y\hat{\Pi}_3}{\tilde{k}}\right) - \partial_y\overline{\mathcal{U}}_0\partial_z\left(A\left[\frac{\tilde{\beta}}{\tilde{k}}\hat{\mathcal{U}}_{3r} + \frac{\tilde{\alpha}}{\tilde{k}}\hat{\mathcal{W}}_{3r})\right]\right) - (\overline{\mathcal{U}}_0 - c)\partial_z\left(A\partial_y\left(\frac{\tilde{\beta}}{\tilde{k}}\hat{\mathcal{U}}_{3r} + \frac{\tilde{\alpha}}{\tilde{k}}\hat{\mathcal{W}}_{3r})\right)\right) \\
&\quad + \partial_z(\partial_y\overline{\mathcal{U}}_0)\left[\frac{\tilde{\beta}}{\tilde{k}}\hat{\mathcal{U}}_{3r} + \frac{\tilde{\alpha}}{\tilde{k}}\hat{\mathcal{W}}_{3r}\right]A + \partial_z\overline{\mathcal{U}}_0\partial_y\left(\frac{\tilde{\beta}}{\tilde{k}}\hat{\mathcal{U}}_{3r} + \frac{\tilde{\alpha}}{\tilde{k}}\hat{\mathcal{W}}_{3r}\right)A \\
&\quad + \Big[(\tilde{k}^2\hat{\mathcal{V}}_3 + i\tilde{k}\partial_y\hat{\mathcal{U}}_{3r})\overline{\mathcal{U}}_1 + \hat{\mathcal{V}}_3\partial_y^2\overline{\mathcal{U}}_1 + [i\tilde{k}\hat{\mathcal{U}}_{3r} + \partial_y\hat{\mathcal{V}}_3]\partial_y\overline{\mathcal{U}}_1\Big]A.
\end{aligned} \tag{2.66}$$

Crucially, the terms multiplying $\overline{\mathcal{U}}_1$ are a combination of continuity (identified in red) and the Rayleigh equation (highlighted in blue) at leading order; hence both are identically zero. We expand the partial z derivatives and group like terms in A to obtain

$$
\begin{aligned}
&B\Big[(\overline{\mathcal{U}}_0 - c)(\partial_{\mathcal{Y}}\hat{\mathcal{V}}_4 - \tilde{k}^2\hat{\mathcal{V}}_4) - \partial^2_{\mathcal{Y}}\overline{\mathcal{U}}_0\hat{\mathcal{V}}_4\Big] = \\
&\quad - \frac{\tilde{k}}{\tilde{\alpha}}(i\tilde{k}\hat{\mathcal{V}}_3 - \partial_{\mathcal{Y}}\hat{\mathcal{U}}_{3r})\overline{\mathcal{U}}_0\partial_x A + \frac{\tilde{k}}{\tilde{\alpha}}\hat{\mathcal{U}}_{3r}(\partial_{\mathcal{Y}}\overline{\mathcal{U}}_0)\partial_x A \\
&\quad + \frac{\tilde{\alpha}}{\tilde{k}}\partial_{\mathcal{Y}}\hat{\Pi}_3\partial_x A - (\overline{\mathcal{U}}_0 - c)\partial_{\mathcal{Y}}\left(\frac{\tilde{\alpha}}{\tilde{k}}\hat{\mathcal{U}}_{3r} - \frac{\tilde{\beta}}{\tilde{k}}\hat{\mathcal{W}}_{3r}\right)\partial_x A - \partial_{\mathcal{Y}}\overline{\mathcal{U}}_0\left[\frac{\tilde{\alpha}}{\tilde{k}}\hat{\mathcal{U}}_{3r} - \frac{\tilde{\beta}}{\tilde{k}}\hat{\mathcal{W}}_{3r}\right]\partial_x A \\
&\quad + \frac{\tilde{\beta}}{\tilde{k}}\partial_{\mathcal{Y}}\hat{\Pi}_3\partial_z A - \partial_{\mathcal{Y}}\overline{\mathcal{U}}_0\left[\frac{\tilde{\beta}}{\tilde{k}}\hat{\mathcal{U}}_{3r} + \frac{\tilde{\alpha}}{\tilde{k}}\hat{\mathcal{W}}_{3r}\right]\partial_z A - (\overline{\mathcal{U}}_0 - c)\,\partial_{\mathcal{Y}}\left(\frac{\tilde{\beta}}{\tilde{k}}\hat{\mathcal{U}}_{3r} + \frac{\tilde{\alpha}}{\tilde{k}}\hat{\mathcal{W}}_{3r}\right)\partial_z A \\
&\quad + \tilde{\beta}\partial_z\left(\frac{\partial_{\mathcal{Y}}\hat{\Pi}_3}{\tilde{k}}\right)A - \partial_{\mathcal{Y}}\overline{\mathcal{U}}_0\partial_z\left[\frac{\tilde{\beta}}{\tilde{k}}\hat{\mathcal{U}}_{3r} + \frac{\tilde{\alpha}}{\tilde{k}}\hat{\mathcal{W}}_{3r}\right]A - (\overline{\mathcal{U}}_0 - c)\,\partial_z\left(\partial_{\mathcal{Y}}\left(\frac{\tilde{\beta}}{\tilde{k}}\hat{\mathcal{U}}_{3r} + \frac{\tilde{\alpha}}{\tilde{k}}\hat{\mathcal{W}}_{3r}\right)\right)A \\
&\quad + \partial_z(\partial_{\mathcal{Y}}\overline{\mathcal{U}}_0)\left[\frac{\tilde{\beta}}{\tilde{k}}\hat{\mathcal{U}}_{3r} + \frac{\tilde{\alpha}}{\tilde{k}}\hat{\mathcal{W}}_{3r}\right]A + \partial_z\overline{\mathcal{U}}_0\partial_{\mathcal{Y}}\left(\frac{\tilde{\beta}}{\tilde{k}}\hat{\mathcal{U}}_{3r} + \frac{\tilde{\alpha}}{\tilde{k}}\hat{\mathcal{W}}_{3r}\right)A \\
&\quad \equiv f_4.
\end{aligned}
\tag{2.67}
$$

For (2.67) to be solvable, the right-hand side must be orthogonal to $\hat{\mathcal{V}}_3^\dagger$, the adjoint null solution associated with the linear operator on the left-hand side (see appendix B). Using integration by parts the adjoint Rayleigh equation can be shown to be

$$
\partial^2_{\mathcal{Y}}[(\overline{\mathcal{U}}_0 - c^*)\hat{\mathcal{V}}_3^\dagger] - \tilde{k}^2[(\overline{\mathcal{U}}_0 - c^*)\hat{\mathcal{V}}_3^\dagger] - (\partial^2_{\mathcal{Y}}\overline{\mathcal{U}}_0)\hat{\mathcal{V}}_3^\dagger = 0, \tag{2.68}
$$

where the asterisk denotes complex conjugation. Therefore, if $\hat{\mathcal{V}}_3$ is a null solution of Rayleigh's equation

$$
(\overline{\mathcal{U}}_0 - c)[\partial^2_{\mathcal{Y}}\hat{\mathcal{V}}_3 - \tilde{k}^2\hat{\mathcal{V}}_3] - (\partial^2_{\mathcal{Y}}\overline{\mathcal{U}}_0)\hat{\mathcal{V}}_3 = 0 \tag{2.69}
$$

with $c \in \Re$, (i.e. $c = c^*$) then $\hat{\mathcal{V}}_3^\dagger = \hat{\mathcal{V}}_3/(\overline{\mathcal{U}}_0 - c)$ is a solution to the adjoint Rayleigh equation (2.68). The Fredholm alternative condition requires $(f_4, \hat{\mathcal{V}}_3^\dagger) = 0$, where f_4 is the right-hand side of (2.67) and the inner product of two complex functions $f(\mathcal{Y})$, $g(\mathcal{Y})$ defined over the VF is given by $(f, g) \equiv \fint_{-\infty}^{\infty} g^* f d\mathcal{Y}$. Here, $\fint_{-\infty}^{\infty}$ denotes the principal value integral. This condition can be satisfied only if the following amplitude equation holds:

$$
a_x\partial_x A \,+\, a_z\partial_z A \,+\, a_0 A \;\;=\;\; 0, \tag{2.70}
$$

where

$$
\begin{aligned}
a_x &= \fint_{-\infty}^{\infty} \left(\frac{\hat{\mathcal{V}}_3^*}{\overline{\mathcal{U}}_0 - c} \right) \Bigg[-\frac{\tilde{k}}{\tilde{\alpha}} (\overline{\mathcal{U}}_0 - c)(i\tilde{k}\hat{\mathcal{V}}_3 - \partial_{\mathcal{Y}}\hat{\mathcal{U}}_{3r}) + \frac{\tilde{k}}{\tilde{\alpha}} (\partial_{\mathcal{Y}}\overline{\mathcal{U}}_0)\hat{\mathcal{U}}_{3r} + \frac{\tilde{\alpha}}{\tilde{k}} \partial_{\mathcal{Y}}\hat{\Pi}_3 \\
&- \partial_{\mathcal{Y}}\overline{\mathcal{U}}_0 \left[\frac{\tilde{\alpha}}{\tilde{k}}\hat{\mathcal{U}}_{3r} - \frac{\tilde{\beta}}{\tilde{k}}\hat{\mathcal{W}}_{3r} \right] - (\overline{\mathcal{U}}_0 - c) \left[\frac{\tilde{\alpha}}{\tilde{k}} \partial_{\mathcal{Y}}\hat{\mathcal{U}}_{3r} - \frac{\tilde{\beta}}{\tilde{k}} \partial_{\mathcal{Y}}\hat{\mathcal{W}}_{3r} \right] \Bigg] d\mathcal{Y}, \qquad (2.71) \\
a_z &= \fint_{-\infty}^{\infty} \left(\frac{\hat{\mathcal{V}}_3^*}{\overline{\mathcal{U}}_0 - c} \right) \left[\frac{\tilde{\beta}}{\tilde{k}} \partial_{\mathcal{Y}}\hat{\Pi}_3 - \partial_{\mathcal{Y}}\overline{\mathcal{U}}_0 \left[\frac{\tilde{\beta}}{\tilde{k}}\hat{\mathcal{U}}_{3r} + \frac{\tilde{\alpha}}{\tilde{k}}\hat{\mathcal{W}}_{3r} \right] \right. \\
&- \left. (\overline{\mathcal{U}}_0 - c)\, \partial_{\mathcal{Y}} \left(\frac{\tilde{\beta}}{\tilde{k}}\hat{\mathcal{U}}_{3r} + \frac{\tilde{\alpha}}{\tilde{k}}\hat{\mathcal{W}}_{3r} \right) \right] d\mathcal{Y}, \qquad (2.72) \\
a_0 &= \fint_{-\infty}^{\infty} \left(\frac{\hat{\mathcal{V}}_3^*}{\overline{\mathcal{U}}_0 - c} \right) \left[\tilde{\beta} \partial_z \left(\frac{\partial_{\mathcal{Y}}\hat{\Pi}_3}{\tilde{k}} \right) - \partial_{\mathcal{Y}}\overline{\mathcal{U}}_0 \partial_z \left[\frac{\tilde{\beta}}{\tilde{k}}\hat{\mathcal{U}}_{3r} + \frac{\tilde{\alpha}}{\tilde{k}}\hat{\mathcal{W}}_{3r} \right] \right. \\
&- (\overline{\mathcal{U}}_0 - c)\, \partial_z \left(\partial_{\mathcal{Y}} \left(\frac{\tilde{\beta}}{\tilde{k}}\hat{\mathcal{U}}_{3r} + \frac{\tilde{\alpha}}{\tilde{k}}\hat{\mathcal{W}}_{3r} \right) \right) \\
&+ \left. \partial_z(\partial_{\mathcal{Y}}\overline{\mathcal{U}}_0) \left[\frac{\tilde{\beta}}{\tilde{k}}\hat{\mathcal{U}}_{3r} + \frac{\tilde{\alpha}}{\tilde{k}}\hat{\mathcal{W}}_{3r} \right] + \partial_z\overline{\mathcal{U}}_0 \partial_{\mathcal{Y}} \left(\frac{\tilde{\beta}}{\tilde{k}}\hat{\mathcal{U}}_{3r} + \frac{\tilde{\alpha}}{\tilde{k}}\hat{\mathcal{W}}_{3r} \right) \right] d\mathcal{Y}. \qquad (2.73)
\end{aligned}
$$

The apparent singularities in the expressions for a_x, a_z and a_0 associated with the prefactor $(\overline{\mathcal{U}}_0 - c)^{-1}$ can be removed through repeated use of the incompressibility condition (2.42) and Rayleigh's equation (2.47). Following considerable algebraic manipulation (see appendix C), the coefficients in the amplitude equation (2.70) can be simplified greatly:

$$
\begin{aligned}
a_x &= -2i\tilde{\alpha} \int_{-\infty}^{\infty} \hat{\mathcal{V}}_3 \hat{\mathcal{V}}_3^* d\mathcal{Y}, \qquad (2.74) \\
a_z &= -2i\tilde{\beta} \int_{-\infty}^{\infty} \hat{\mathcal{V}}_3 \hat{\mathcal{V}}_3^* d\mathcal{Y}, \qquad (2.75) \\
a_0 &= -i \int_{-\infty}^{\infty} \left[2\tilde{\beta} \partial_z(\hat{\mathcal{V}}_3)\hat{\mathcal{V}}_3^* + (\partial_z\tilde{\beta})\hat{\mathcal{V}}_3\hat{\mathcal{V}}_3^* - 2\frac{\tilde{\beta}}{\tilde{k}^2} \partial_{\mathcal{Y}} \left(\frac{\partial_z\overline{\mathcal{U}}_0}{\overline{\mathcal{U}}_0 - c} \right) (\partial_{\mathcal{Y}}\hat{\mathcal{V}}_3)\hat{\mathcal{V}}_3^* \right. \\
&+ \left. 2\frac{\tilde{\beta}}{\tilde{k}^2} \partial_{\mathcal{Y}} \left(\frac{\partial_z\overline{\mathcal{U}}_0}{\overline{\mathcal{U}}_0 - c} \right) \left[\frac{\hat{\mathcal{V}}_3\hat{\mathcal{V}}_3^* \partial_{\mathcal{Y}}\overline{\mathcal{U}}_0}{\overline{\mathcal{U}}_0 - c} \right] \right] d\mathcal{Y}. \qquad (2.76)
\end{aligned}
$$

Note that the integrand in (2.76) is regular as $\mathcal{Y} \to 0$ (since $\overline{\mathcal{U}}_0 \sim \tilde{\lambda}\mathcal{Y}$) and all integrals are convergent, as shown in appendix C.

To identify the simplest viable inertial-layer SSP, we henceforth seek solutions to (2.70) for which $A = A(z)$, only. Consequently, the amplitude equation simplifies to

$$a_z \partial_z A + a_0 A = 0, \tag{2.77}$$

which can be readily integrated, yielding an equation for the amplitude function

$$A = \exp\left(- \int_0^z \frac{a_0}{a_z} dz \right), \tag{2.78}$$

where $A(z) = A(-z)$; i.e., A is even about $z = 0$, and the constant of integration has been subsumed into the constant $\mathcal{A}$ arising in the WKBJ ansatz.

The solution (2.78) breaks down at those z locations where $a_z \to 0$. In particular, the coefficient $a_z \to 0^+$ while $a_0 < 0$ remains finite as $\tilde{\beta} \to 0^+$, as can be corroborated using (2.75)-(2.76). Thus, there is a curve (a line in the x–z plane in the present context), termed a *caustic*, on which the amplitude $A(z)$ formally becomes unbounded. The caustic separates the flow within the VF into a region with finite-amplitude fluctuations, termed the 'illuminated' region, and a region in which the fluctuations are exponentially small, termed the 'shadow' region. A more careful analysis (see appendix D) confirms that within an asymptotically small neighborhood of each caustic the amplitude is viscously regularized and thus does not become unbounded. Moreover, the spanwise fluctuation velocity is suppressed at the caustic since the spanwise fluctuation pressure gradient is weak there relative to its magnitude in the illuminated region, enabling the incident Rayleigh mode to two-dimensionalize prior to being reflected. Upon reflection, the rays leaving each caustic experience a $\pi/2$ phase shift in z. Finally, it can be shown that the contribution to the roll-flow energy budget (performed in section 2.5) from this neighborhood of each caustic is asymptotically small (again, because w' is suppressed there) and therefore can be neglected from the integral (2.137) used to calculate $\bar{\Omega}_c$.

2.4 Critical Layers

Although the rotated neutral-mode velocity components $\hat{\mathcal{U}}_{3r}$ and $\hat{\mathcal{V}}_3$ are regular for all $\mathcal{Y} \in (-\infty, \infty)$, the rotated spanwise fluctuation velocity $\hat{\mathcal{W}}_{3r}$ is singular as $\mathcal{Y} \to 0$, as evident from inspection of (2.45). Thus, a critical layer (CL) emerges within the VF, where the horizontal mean streamwise flow speed matches the phase speed (i.e. 0, for the VF centered at $\mathcal{Y} = 0$) of the instability mode. Within this CL, the $\mathcal{Y}^{-1}$ amplification of the (non-rotated) fluctuation fields $\hat{\mathcal{U}}_3$ and $\hat{\mathcal{W}}_3$ is viscously regularized.

To examine the dynamics within the CL, we introduce a rescaled fissure-normal coordinate $Y \equiv y/\tilde{\delta}$, where $\tilde{\delta}$ is the scaled thickness of the critical layer (and, again, $\tilde{\delta}/\tilde{\Delta} \to 0$ as $Re \to \infty$), and posit the following expansions:

$$u(x,y,z,t;Re) \sim \tilde{\Delta}\overline{U}_1(Y,z) + a'\frac{\tilde{\Delta}}{\tilde{\delta}}U_2'(x,Y,z) + \cdots , \tag{2.79}$$

$$v(x,y,z,t;Re) \sim \overline{a}\tilde{\delta}\,\overline{V}_4(Y,z) + a'V_3'(x,Y,z) + \cdots , \tag{2.80}$$

$$w(x,y,z,t;Re) \sim \overline{a}\overline{W}_2(z) + a'\frac{\tilde{\Delta}}{\tilde{\delta}}W_2'(x,Y,z) + \overline{a}\tilde{\Delta}\overline{W}_3(Y,z) + \cdots , \tag{2.81}$$

$$p(x,y,z,t;Re) \sim \overline{a}^2\overline{P}_4(z) + a'P_3'(x,Y,z) + \cdots . \tag{2.82}$$

Thus, for smooth matching with the streak and roll flow in the VF, the streak velocity becomes small, i.e. $O(\tilde{\Delta})$, while the mean spanwise velocity component remains $O(\bar{a})$ within the CL. The latter scaling follows because, within the CL, $\bar{w}$ is not sheared at leading order. In addition, the fissure-normal fluctuation velocity component v' remains $O(a')$ as the CL is approached while the tangential components u' and w' blow-up algebraically; this growth is accounted for by the amplification of these fluctuation velocity components by the factor $\tilde{\Delta}/\tilde{\delta}$ in (2.79) and (2.81).

2.4.1 Mean Equations

We next demonstrate that the nonlinear self-interaction of the fluctuation mode within the CL gives rise to a Reynolds stress divergence that ultimately drives a spanwise mean flow. To determine this transverse mean-flow response, we apply the streamwise/fast-phase averaging operation

to the $\perp$-momentum equations. When integrated across the CL, the leading-order (i.e. $O(\tilde{\Delta}^3)$) balance $\partial_Y^2 \overline{W}_3 - \partial_Y(\overline{V_3' W_2'}) = 0$ fails to induce a jump in the mean x-vorticity. Accordingly, we turn to the mean equations at $O(\tilde{\Delta}^4)$:

$$\partial_Y^2 \overline{U}_1 = 0, \tag{2.83}$$

$$\partial_Y \tilde{P}_4 = 0, \tag{2.84}$$

$$\tilde{W}_2 \partial_z \tilde{W}_2 = -\partial_z \tilde{P}_4 - \frac{\partial_z(\overline{W_2' W_2'})}{\overline{\Omega}_c^2} - \frac{\partial_Y(\overline{V_3' W_3'})}{\overline{\Omega}_c^2} + \partial_Y^2 \tilde{W}_4, \tag{2.85}$$

$$\partial_Y \tilde{V}_4 + \partial_z \tilde{W}_2 = 0. \tag{2.86}$$

The solution to the mean x-momentum equation is

$$\overline{U}_1 = \tilde{\lambda} Y. \tag{2.87}$$

Here, again, the mean transverse velocities and pressure have been rescaled so that $(\overline{V}_4, \overline{W}_2) = \bar{\Omega}_c(\tilde{V}_4, \tilde{W}_2)$ and $\overline{P}_4 = \bar{\Omega}_c^2 \tilde{P}_4$. Balancing the fluctuation-induced forcing with mean diffusion in both the $O(\tilde{\Delta}^3)$ and the $O(\tilde{\Delta}^4)$ mean $\perp$-momentum equations requires the scaling relationship $(a')^2 = \overline{a}/(\bar{\Omega}_c Re)$ to be satisfied. Recalling that $\overline{a} = 1/(\bar{\Omega}_c Re \tilde{\Delta}^2)$, the former relation is consistent with the requirement that $a' = \tilde{\Delta}\overline{a}$, an ordering already presumed in the analysis of the mean dynamics within the VF (see section 2.3.1). From the analysis of the VF it is also known that

$$-\partial_z \tilde{\mathcal{P}}_4 = \tilde{\mathcal{W}}_2 \partial_z \tilde{\mathcal{W}}_2.$$

Since both $\tilde{P}_4$ and $\tilde{W}_2$ are independent of Y, this equality must also hold within the critical layer. Subtracting this asymptotic balance from (2.85) and integrating the result across the CL (noting that the term involving the cross-correlation again integrates to zero) yields

$$\left[\partial_Y \tilde{W}_4\right]_-^+ = \frac{1}{\bar{\Omega}_c^2} \int_{-\infty}^{\infty} \partial_z \left(\overline{W_2' W_2'}\right)\, dY, \tag{2.88}$$

where $[\cdot]_-^+$ denotes the jump across the CL.

Matching the mean x-vorticity at the edges of the CL with that at the center of the VF yields a crucial final scaling relationship $\tilde{\delta} = \tilde{\Delta}^2$. Moreover, the jump in the mean x-vorticity across the CL now can be expressed as

$$\left[\partial_{\mathcal{Y}} \tilde{\mathcal{W}}_3\right]_-^+ = \frac{1}{\bar{\Omega}_c^2} \int_{-\infty}^{\infty} \partial_z \left(\overline{W_2' W_2'}\right)\, dY. \tag{2.89}$$

Thus, as in VWI theory, a jump in the x-mean spanwise shear across the CL is induced by the nonlinear self-interaction of the Rayleigh mode within the CL. A key distinction, however, arises because of the separation in length scales between the rolls and the instability mode; in particular, a *modulational* spanwise derivative of the Rayleigh-mode-induced Reynolds stress is operative in the present construction.

2.4.2 Fluctuation Equations

To evaluate the stress jump (2.89), the fluctuation dynamics within the CL must be analyzed. The requirement that viscous forces arise at leading order in the fluctuation equations yields the scaling relationship $Re\tilde{\delta}^3 = \tilde{\Delta}^2$. Using this relation in conjunction with the three other scaling relationships among the asymptotic parameters $\tilde{\Delta}$, $\tilde{\delta}$, $\overline{a}$ and a' gives

$$\tilde{\Delta} = \left(\bar{\Omega}_c Re\right)^{-1/4};\ \tilde{\delta} = \left(\bar{\Omega}_c Re\right)^{-1/2};\ \overline{a} = \tilde{\Delta}^2;\ a' = \tilde{\Delta}^3; \tag{2.90}$$

implying $\Delta = Re^{-1/4}$ and $\delta = Re^{-1/2}$ (see table 2.2). For the CL at $y = 0$, the leading-order fluctuation equations thus reduce to

$$\begin{aligned}
\partial_x U_2' + \bar{\Omega}_c \partial_Y V_3' + \partial_z W_2' &= 0, && (2.91)\\
\overline{U}_1 \partial_x U_2' + V_3' \partial_Y \overline{U}_1 &= -\partial_x P_3' + \bar{\Omega}_c \partial_Y^2 U_2', && (2.92)\\
\partial_Y P_3' &= 0, && (2.93)\\
\overline{U}_1 \partial_x W_2' &= -\partial_z P_3' + \bar{\Omega}_c \partial_Y^2 W_2', && (2.94)
\end{aligned}$$

where the factor $\bar{\Omega}_c$ appears as a diffusion coefficient in the fluctuation momentum equations owing to the redefinition of the small parameter $\Delta \to \tilde{\Delta}$. It can be seen from the y-momentum equation that the fluctuating pressure in this region is independent of Y. We make the following ansatz for the fluctuation fields in the CL:

$$\begin{bmatrix} U_2' \\ V_3' \\ W_2' \\ P_3' \end{bmatrix} = \mathcal{A} \begin{bmatrix} \hat{U}_2(Y;z) \\ \hat{V}_3(Y;z) \\ \hat{W}_2(Y;z) \\ \hat{P}_3(z) \end{bmatrix} A(z)\, \mathrm{e}^{i\left[\alpha(x-ct)+\theta(z/\tilde{\Delta})\right]} \; + \; c.c.$$

Substituting this ansatz into (2.94) yields an equation for $\hat{W}_2$,

$$i\tilde{\alpha}\overline{U}_1\hat{W}_2 = -i\tilde{\beta}\hat{\mathcal{P}}_3|_{\mathcal{Y}=0} + \bar{\Omega}_c\partial_Y^2\hat{W}_2, \tag{2.95}$$

and using (2.87) to eliminate $\overline{U}_1$ gives

$$\partial_Y^2\hat{W}_2 - i\frac{\tilde{\alpha}\tilde{\lambda}}{\overline{\Omega}_c}Y\hat{W}_2 = \frac{i\tilde{\beta}}{\overline{\Omega}_c}\hat{\mathcal{P}}_3|_{\mathcal{Y}=0}. \tag{2.96}$$

The Airy-like solution for $\hat{W}_2$ is proportional to $\mathrm{Yi}(s)$, where Yi solves $\mathrm{Yi}'' - is\mathrm{Yi} = \frac{1}{\pi}$ subject to decay conditions as as $|s| \to \infty$ and has the following integral representation (Balmforth *et al.*, 1997):

$$\mathrm{Yi}(s) \equiv -\frac{1}{\pi}\int_0^\infty \exp(-\frac{\eta^3}{3} - is\eta)d\eta. \tag{2.97}$$

The real and imaginary parts of the function $\mathrm{Yi}(s)$ are plotted in figure 2.5. Hence, the solution to (2.96) can be expressed as

$$\hat{W}_2 = -\overline{\Omega}_c^{-1/3}(\tilde{\alpha}\tilde{\lambda})^{-2/3}(i\tilde{\beta}\hat{\mathcal{P}}_3|_{\mathcal{Y}=0})\int_0^\infty e^{-i\left(\frac{\tilde{\alpha}\tilde{\lambda}}{\overline{\Omega}_c}\right)^{1/3}Y\varphi-\varphi^3/3}d\varphi. \tag{2.98}$$

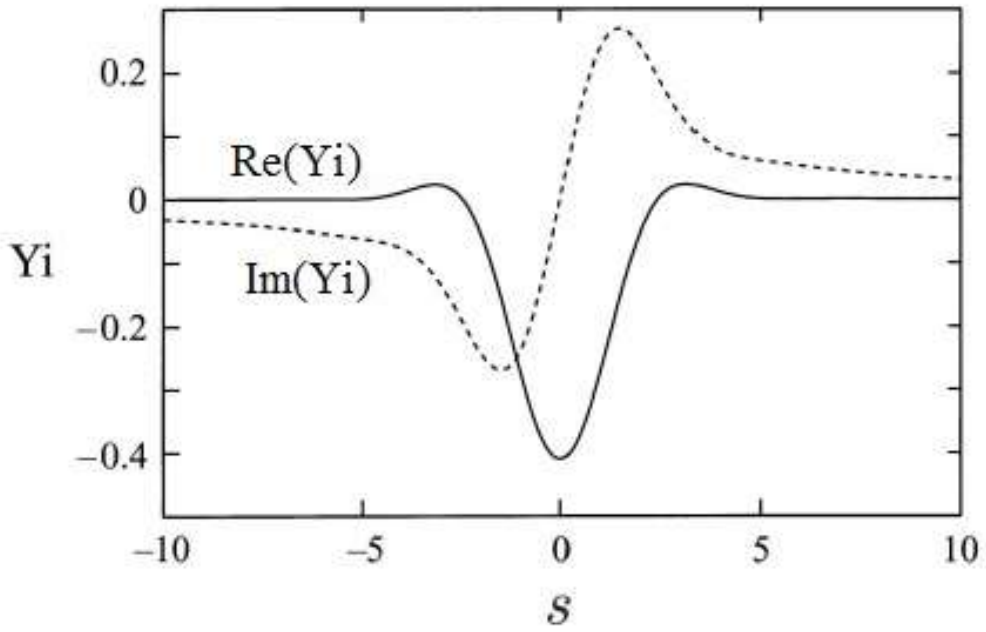

Figure 2.5: The real (Re) and imaginary (Im) parts of the function Yi(s) for real s. (Adapted from Balmforth *et al.* (1997).)

To determine how this solution will match with the spanwise fluctuation velocity component within the VF, the behavior of $\mathrm{Yi}(s)$ at large $|s|$ is required:

$$\mathrm{Yi}(s) \sim \frac{i}{\pi s} \sum_{n=0}^{\infty} \frac{(3n)!}{3^n n!} (is)^{-3n} \quad \text{if} \quad \arg(s) < \frac{1}{6}\pi \ \text{ or } \ \frac{5}{6}\pi < \arg(s), \tag{2.99}$$

and

$$\mathrm{Yi}(s) \sim \exp\left[\frac{2}{3}s^{3/2}\right] \quad \text{if} \quad \frac{1}{6}\pi < \arg(s) < \frac{5}{6}\pi. \tag{2.100}$$

These asymptotic expansions show $\mathrm{Yi}(s) \sim i/(\pi s)$ as the real part of $s \to \pm\infty$ with the imaginary component of s fixed, confirming that the fluctuating spanwise velocity component decays in the far field of the CL (i.e. as $|Y| \to \infty$) to smoothly match with its functional form in the internal shear layer.

From the mean spanwise momentum equation, the vorticity jump across the CL is given by (2.89). To evaluate the vorticity jump, $\overline{W_2' W_2'}$ first needs to be determined in terms of $\hat{W}_2$. Recalling

that the analysis in appendix D indicates that the fluctuation fields experience a $\pi/2$ spanwise phase shift upon reflection from each caustic, the spanwise fluctuation velocity can be expressed as

$$W_2' = \mathcal{A}\Bigg(A\hat{W}_2^+ e^{i(\alpha x+\theta+\frac{\pi}{4})} + A\hat{W}_2^+ e^{i(\alpha x+\theta+\frac{3\pi}{4})} + A\hat{W}_2^- e^{i(\alpha x-\theta-\frac{\pi}{4})} + A\hat{W}_2^- e^{i(\alpha x-\theta-\frac{3\pi}{4})} + c.c.\Bigg). \tag{2.101}$$

Inspection of the fluctuation z-momentum equation for $\tilde{\beta} \to -\tilde{\beta}$ shows that $\hat{W}_2 \equiv \hat{W}_2^+ = -\hat{W}_2^-$. Forming the product of W_2' with itself and applying the streamwise/fast-phase averaging operation therefore yields

$$\overline{(W_2'W_2')} = 8\mathcal{A}^2 A^2 \hat{W}_2^+ \hat{W}_2^{+*} \equiv 8\mathcal{A}^2 A^2 \hat{W}_2 \hat{W}_2^*. \tag{2.102}$$

Substituting (2.102) into (2.89) then gives

$$\left[\partial_{\mathcal{Y}} \tilde{\mathcal{W}}_3\right]_-^+ = 8\mathcal{A}^2 \overline{\Omega}_c^{-2} \int_{-\infty}^{\infty} \partial_z (A^2 \hat{W}_2 \hat{W}_2^*) dY. \tag{2.103}$$

Using (2.98) to eliminate $\hat{W}_2$ yields

$$\left[\partial_{\mathcal{Y}} \tilde{\mathcal{W}}_3\right]_-^+ = 8\frac{\mathcal{A}^2}{\overline{\Omega}_c^2} \int_{-\infty}^{\infty} \partial_z \Bigg(\overline{\Omega}_c^{-2/3} A^2 (\tilde{\alpha}\tilde{\lambda})^{-4/3} \tilde{\beta}^2 \left|\hat{\mathcal{P}}_3|_{\mathcal{Y}=0}\right|^2 \times \int_0^{\infty} e^{-i\left(\frac{\tilde{\alpha}\tilde{\lambda}}{\overline{\Omega}_c}\right)^{1/3} Y\varphi - \varphi^3/3} d\varphi \int_0^{\infty} e^{i\left(\frac{\tilde{\alpha}\tilde{\lambda}}{\overline{\Omega}_c}\right)^{1/3} Y\psi - \psi^3/3} d\psi \Bigg) dY. \tag{2.104}$$

We rescale the Y term so that $\hat{Y} = \left(\frac{\tilde{\alpha}\tilde{\lambda}}{\overline{\Omega}_c}\right)^{1/3} Y$, giving

$$\begin{aligned}\left[\partial_{\mathcal{Y}} \tilde{\mathcal{W}}_3\right]_-^+ &= 8\frac{\mathcal{A}^2}{\overline{\Omega}_c^2} \int_{-\infty}^{\infty} \partial_z \left(\overline{\Omega}_c^{-1/3} A^2 (\tilde{\alpha}\tilde{\lambda})^{-5/3} \tilde{\beta}^2 \left|\hat{\mathcal{P}}_3|_{\mathcal{Y}=0}\right|^2 \int_0^{\infty} e^{-i\hat{Y}\varphi - \varphi^3/3} d\varphi \int_0^{\infty} e^{i\hat{Y}\psi - \psi^3/3} d\psi \right) d\hat{Y} \\ &= \frac{8\mathcal{A}^2}{\overline{\Omega}_c^{7/3} \tilde{\alpha}^{5/3}} \partial_z \left(\frac{A^2 \tilde{\beta}^2 \left|\hat{\mathcal{P}}_3|_{\mathcal{Y}=0}\right|^2}{\tilde{\lambda}^{5/3}} \int_{-\infty}^{\infty} \left[\int_0^{\infty} e^{-i\hat{Y}\varphi - \varphi^3/3} d\varphi \int_0^{\infty} e^{i\hat{Y}\psi - \psi^3/3} d\psi \right] d\hat{Y} \right).\end{aligned} \tag{2.105}$$

Next, we use the fact that if arbitrary functions f and g are integrable functions, then the integral of their convolution on the whole space $(-\infty, \infty)$ is simply obtained as the product of their integrals

each taken on the half space $[0,\infty)$. The convolution used for (2.105) is summarized in appendix E. This result gives

$$\begin{aligned}\left[\partial_{\mathcal{Y}}\tilde{\mathcal{W}}_3\right]_-^+ &= \frac{8\mathcal{A}^2}{\overline{\Omega}_c^{7/3}\tilde{\alpha}^{5/3}}\partial_z\left(\frac{A^2\tilde{\beta}^2\left|\hat{\mathcal{P}}_3|_{\mathcal{Y}=0}\right|^2}{\tilde{\lambda}^{5/3}}\int_{-\infty}^{\infty}\left[\int_0^{\infty}\frac{\sqrt{\pi}}{\sqrt{\varphi}}e^{-\frac{\hat{Y}^2}{\varphi}-\varphi^3/12}d\varphi\right]d\hat{Y}\right)\\ &= \frac{8\pi\mathcal{A}^2}{\overline{\Omega}_c^{7/3}\tilde{\alpha}^{5/3}}\partial_z\left(\frac{A^2\tilde{\beta}^2\left|\hat{\mathcal{P}}_3|_{\mathcal{Y}=0}\right|^2}{\tilde{\lambda}^{5/3}}\int_0^{\infty}\left[e^{-\varphi^3/12}\int_{-\infty}^{\infty}\frac{1}{\sqrt{\pi\varphi}}e^{-\frac{\hat{Y}^2}{\varphi}}d\hat{Y}\right]d\varphi\right).\end{aligned} \tag{2.106}$$

Recognizing the $\hat{Y}$ integral inside the brackets as twice the error function, this expression simplifies to

$$\left[\partial_{\mathcal{Y}}\tilde{\mathcal{W}}_3\right]_-^+ = \frac{8\pi\mathcal{A}^2}{\overline{\Omega}_c^{7/3}\tilde{\alpha}^{5/3}}\partial_z\left(\frac{A^2\tilde{\beta}^2\left|\hat{\mathcal{P}}_3|_{\mathcal{Y}=0}\right|^2}{\tilde{\lambda}^{5/3}}\int_0^{\infty}e^{-\varphi^3/12}d\varphi\right). \tag{2.107}$$

The remaining integral can be evaluated analytically in terms of the Gamma function. Consequently, the stress jump may be expressed as

$$\left[\partial_{\mathcal{Y}}\tilde{\mathcal{W}}_3\right]_-^+ = \frac{8\pi\mathcal{A}^2\left(\frac{2}{3}\right)^{2/3}\Gamma\left(\frac{1}{3}\right)}{\overline{\Omega}_c^{7/3}\tilde{\alpha}^{5/3}}\partial_z\left(\frac{A^2\tilde{\beta}^2\left|\hat{\mathcal{P}}_3|_{\mathcal{Y}=0}\right|^2}{\tilde{\lambda}^{5/3}}\right), \tag{2.108}$$

where Γ is the Gamma function. Recalling $\hat{P}_3 = \frac{\tilde{\alpha}}{\tilde{k}}\hat{\Pi}_3$, and letting $n_0 = 2\pi(2/3)^{2/3}\Gamma(1/3)$, following the notation in Hall & Sherwin (2010), (2.108) reduces to

$$\left[\partial_{\mathcal{Y}}\tilde{\mathcal{W}}_3\right]_-^+ = \frac{4n_0\mathcal{A}^2\tilde{\alpha}^{1/3}}{\overline{\Omega}_c^{7/3}}\partial_z\left(\frac{A^2\tilde{\beta}^2\left|\hat{\Pi}_3|_{\mathcal{Y}=0}\right|^2}{\tilde{k}^2\tilde{\lambda}^{5/3}}\right). \tag{2.109}$$

Here, again, the z derivative is a modulational derivative unlike in VWI. Finally, normalizing so that $|\hat{\Pi}_3|_{\mathcal{Y}=0} = \tilde{\lambda}/\tilde{k}$ (so that, conveniently, $\hat{\mathcal{V}}_3|_{\mathcal{Y}=0} = -i$) gives

$$\left[\partial_{\mathcal{Y}}\tilde{\mathcal{W}}_3\right]_-^+ = \frac{4n_0\mathcal{A}^2\tilde{\alpha}^{1/3}}{\overline{\Omega}_c^{7/3}}\partial_z\left(\frac{A^2\tilde{\beta}^2\tilde{\lambda}^{1/3}}{\tilde{k}^4}\right). \tag{2.110}$$

Consequently, the jump in spanwise shear stress across the CL is known in terms of the Rayleigh-mode parameters, i.e. the scalar amplitude $\mathcal{A}$, amplitude function $A(z)$, streamwise wavenumber

$\tilde{\alpha}$ and spanwise wavenumber $\tilde{\beta}(z)$, and in terms of the streak shear stress $\tilde{\lambda}(z)$ and the to-be-determined roll vorticity $\bar{\Omega}_c$. Note that $\bar{\Omega}_c$ also must be known to relate the $O(1)$ streamwise wavenumbers $\tilde{\alpha}$ and $\breve{\alpha}$. Since the latter is rendered dimensionless using only $Re^{1/4}$ and l_y, it is a more natural control parameter, e.g., for numerical computations of ECS at large but finite Re using the full NS equations.

2.5 Roll-Flow Energy Budget

To close the analysis, the nonlinear eigenvalue $\bar{\Omega}_c$ must be self-consistently determined. The required calculation exploits the fact that, physically, the stress jump across the CL drives a spanwise flow within and, thence, a roll flow outside the VFs. More specifically, the work done by the mean viscous tangential stress at the CL/VF boundary is balanced by dissipation of roll kinetic energy within the UMZ. This constraint can be utilized to determine the unknown roll vorticity $\bar{\Omega}_c$ by integrating the steady form of the x-mean $\perp$-kinetic energy equation over one roll cell, *excluding* the critical layers at $y = 0, 1$.

We begin with the exact mean equations,

$$\partial_t \overline{v} + \overline{v}\partial_y \overline{v} + \overline{w}\partial_z \overline{v} = -\partial_y \overline{p} - \partial_y(\overline{v'v'}) - \partial_z(\overline{v'w'}) + \frac{1}{Re}\nabla_\perp^2 \overline{v}, \tag{2.111}$$

$$\partial_t \overline{w} + \overline{v}\partial_y \overline{w} + \overline{w}\partial_z \overline{w} = -\partial_z \overline{p} - \partial_y(\overline{v'w'}) - \partial_z(\overline{w'w'}) + \frac{1}{Re}\nabla_\perp^2 \overline{w}. \tag{2.112}$$

Multiplying (2.111) by $\bar{v}$ and (2.112) by $\bar{w}$ yields a mean energetics equation:

$$\begin{aligned} \overline{v}\partial_t \overline{v} + \overline{w}\partial_t \overline{w} + \overline{v}\overline{v}\partial_y \overline{v} + \overline{w}\overline{v}\partial_z \overline{v} + \overline{v}\overline{w}\partial_y \overline{w} + \overline{w}\overline{w}\partial_z \overline{w} = \\ - \overline{v}\partial_y \overline{p} - \overline{w}\partial_z \overline{p} - \overline{v}\partial_y(\overline{v'v'}) - \overline{v}\partial_z(\overline{v'w'}) - \overline{w}\partial_y(\overline{v'w'}) - \overline{w}\partial_z(\overline{w'w'}) \\ + \frac{1}{Re}(\overline{v}\nabla_\perp^2 \overline{v} + \overline{w}\nabla_\perp^2 \overline{w}), \end{aligned} \tag{2.113}$$

or, in conservative form,

$$\partial_t\left(\frac{\overline{v}^2}{2}+\frac{\overline{w}^2}{2}\right)+\partial_y\left[\bar{v}\left(\frac{\overline{v}^2}{2}+\frac{\overline{w}^2}{2}\right)\right]+\partial_z\left[\bar{w}\left(\frac{\overline{v}^2}{2}+\frac{\overline{w}^2}{2}\right)\right]=$$
$$-\partial_y(\bar{v}\bar{p})-\partial_z(\bar{w}\bar{p})-\overline{v}\partial_y(\overline{v'v'})-\overline{v}\partial_z(\overline{v'w'})-\overline{w}\partial_y(\overline{v'w'}) \tag{2.114}$$
$$-\overline{w}\partial_z(\overline{w'w'})+\frac{1}{Re}(\overline{v}\nabla_\perp^2\overline{v}+\overline{w}\nabla_\perp^2\overline{w}).$$

We integrate the steady form of (2.114) over one cell excluding the critical layers at $y=0$ and $y=1$ to obtain

$$\int_0^{L_z/2}\int_{0^+}^{1^-}\Bigg\{\underbrace{\partial_y\left[\bar{v}\left(\frac{\overline{v}^2}{2}+\frac{\overline{w}^2}{2}\right)\right]}_{1}+\underbrace{\partial_z\left[\bar{w}\left(\frac{\overline{v}^2}{2}+\frac{\overline{w}^2}{2}\right)\right]}_{2}=$$
$$\underbrace{-\partial_y(\bar{v}\bar{p})-\partial_z(\bar{w}\bar{p})}_{3}\underbrace{-\overline{v}\partial_y(\overline{v'v'})-\overline{v}\partial_z(\overline{v'w'})-\overline{w}\partial_y(\overline{v'w'})-\overline{w}\partial_z(\overline{w'w'})}_{4} \tag{2.115}$$
$$\underbrace{+\frac{1}{Re}(\overline{v}\nabla_\perp^2\overline{v}+\overline{w}\nabla_\perp^2\overline{w})}_{5}\Bigg\}dydz.$$

The asymptotic matching conditions along $y=0^+$ and $y=1^-$ and the exact symmetry conditions along $z=0$ and $z=L_z/2$ needed for the evaluations of the integrals are as follows:

$$\overline{v}(1^-,z) = O(\Delta^4), \tag{2.116}$$
$$\overline{v}(0^+,z) = O(\Delta^4), \tag{2.117}$$
$$\overline{w}(y,0) = 0, \tag{2.118}$$
$$\overline{w}(y,L_z/2) = 0. \tag{2.119}$$

The leading-order balance in the roll-flow energy budget (2.115) arises at $O(\Delta^8)$ and, using the x-mean incompressibility condition and matching and symmetry conditions around the roll-cell periphery, can be shown to include only the term proportional to $1/Re$. To see this, we first analyze the integral of the terms in group one:

$$\int_0^{L_z/2}\int_{0^+}^{1^-}\partial_y\left[\bar{v}\left(\frac{\overline{v}^2}{2}+\frac{\overline{w}^2}{2}\right)\right]dydz = = \int_0^{L_z/2}\left[\bar{v}\left(\frac{\overline{v}^2}{2}\right)\Big|_{0^+}^{1^-}+\bar{v}\left(\frac{\overline{w}^2}{2}\right)\Big|_{0^+}^{1^-}\right]dz,$$
$$= \int_0^{L_z/2}\left[\bar{v}\left(\frac{\overline{v}^2}{2}\right)\Big|_{0^+}^{1^-}\right]dz, \tag{2.120}$$
$$= O(\Delta^{12}),$$

upon noting that $\bar{w}^2$ is even and $\bar{v}$ is odd about $z = L_z/4$ (along lines $y = 0^+$ and $y = 1^-$).

The integral of the terms belonging to group two trivially vanishes using the symmetry conditions (2.118)-(2.119). Next, we integrate the terms in group three in (2.115):

$$-\int_0^{L_z/2}\int_{0^+}^{1^-}\left[\partial_y(\bar{v}\bar{p})+\partial_z(\bar{w}\bar{p})\right]dydz = -\left[\int_0^{L_z/2}\bar{v}\bar{p}\Big|_{y=0^+}^{y=1^-}dz+\int_{0^+}^{1^-}\bar{w}\bar{p}\Big|_{z=0}^{z=L_z/2}dy\right], \tag{2.121}$$
$$= 0,$$

using the fact that, within the VFs at $y = 0$ and $y = 1$, $\bar{p}$, like $\bar{w}^2$, is an even function of z about the line $z = \pi/4$ (cf. (2.25)). Finally, the terms in group four in (2.115) are asymptotically small compared to the terms comprising group five over the entire domain of integration, owing to the scaling of the fluctuation fields. Therefore, at leading order, (2.115) reduces to

$$\int_0^{L_z/2}\int_{0^+}^{1^-}\left[\overline{v}\nabla_\perp^2\overline{v}+\overline{w}\nabla_\perp^2\overline{w}\right]dydz = 0, \tag{2.122}$$

or, equivalently, upon substituting $\overline{v} = \overline{\Omega}_c\tilde{v}$ and $\overline{w} = \overline{\Omega}_c\tilde{w}$

$$\int_0^{L_z/2}\int_{0^+}^{1^-}\left[\tilde{v}\nabla_\perp^2\tilde{v}+\tilde{w}\nabla_\perp^2\tilde{w}\right]dydz = 0. \tag{2.123}$$

We next evaluate this integral asymptotically. Considering first the terms involving $\tilde{w}$, we integrate by parts to show

$$\begin{aligned}\int_0^{L_z/2}\int_{0^+}^{1^-}\left[\tilde{w}\nabla_\perp^2\tilde{w}\right]dydz &= \int_0^{L_z/2}\int_{0^+}^{1^-}\Big[\tilde{w}\nabla_\perp\cdot(\nabla_\perp\tilde{w})\Big]dydz,\\ &= \int_0^{L_z/2}\int_{0^+}^{1^-}\Big[\nabla_\perp\cdot(\tilde{w}\nabla_\perp\tilde{w})-(\nabla_\perp\tilde{w})\cdot(\nabla_\perp\tilde{w})\Big]dydz,\\ &= \int_0^{L_z/2}\int_{0^+}^{1^-}\partial_y\left[\tilde{w}\partial_y\tilde{w}\right]dydz+\int_0^{L_z/2}\int_{0^+}^{1^-}\partial_z\left[\tilde{w}\partial_z\tilde{w}\right]dydz\\ &\quad-\int_0^{L_z/2}\int_{0^+}^{1^-}\left[(\partial_y\tilde{w})^2+(\partial_z\tilde{w})^2\right]dydz.\end{aligned} \tag{2.124}$$

Using periodicity in the z-direction, we obtain

$$\int_0^{L_z/2}\int_{0^+}^{1^-}\left[\tilde{w}\nabla_\perp^2\tilde{w}\right]dydz=\int_0^{L_z/2}\tilde{w}\partial_y\tilde{w}\Big|_{y=0^+}^{y=1^-}dz-\int_0^{L_z/2}\int_{0^+}^{1^-}\left[(\partial_y\tilde{w})^2+(\partial_z\tilde{w})^2\right]dydz. \tag{2.125}$$

Moreover, using $\tilde{w}\partial_y\tilde{w}\Big|_{y=1^-}=-\tilde{w}\partial_y\tilde{w}\Big|_{y=0^+}$,

$$\begin{aligned}\int_0^{L_z/2}\int_{0^+}^{1^-}\left[\tilde{w}\nabla_\perp^2\tilde{w}\right]dydz &= -2\int_0^{L_z/2}\tilde{w}\partial_y\tilde{w}\Big|_{y=0^+}dz-\int_0^{L_z/2}\int_{0^+}^{1^-}\left[(\partial_y\tilde{w})^2+(\partial_z\tilde{w})^2\right]dydz,\\ &= -2\int_0^{L_z/2}\tilde{w}\partial_y\tilde{w}\Big|_{y=0^+}dz-\int_0^{L_z/2}\int_{0^+}^{1^-}(\nabla_\perp\tilde{w})^2dydz.\end{aligned} \tag{2.126}$$

We next consider the terms in (2.123) involving $\tilde{v}$. Integrating by parts yields

$$\begin{aligned}\int_0^{L_z/2}\int_{0^+}^{1^-}\left[\tilde{v}\nabla_\perp^2\tilde{v}\right]dydz &= \int_0^{L_z/2}\int_{0^+}^{1^-}\Big[\tilde{v}\nabla_\perp\cdot(\nabla_\perp\tilde{v})\Big]dydz,\\ &= \int_0^{L_z/2}\int_{0^+}^{1^-}\Big[\nabla_\perp\cdot(\tilde{v}\nabla_\perp\tilde{v})-(\nabla_\perp\tilde{v})\cdot(\nabla_\perp\tilde{v})\Big]dydz,\\ &= \int_0^{L_z/2}\int_{0^+}^{1^-}\partial_y\left[\tilde{v}\partial_y\tilde{v}\right]dydz+\int_0^{L_z/2}\int_{0^+}^{1^-}\partial_z\left[\tilde{v}\partial_z\tilde{v}\right]dydz\\ &\quad-\int_0^{L_z/2}\int_{0^+}^{1^-}\left[(\partial_y\tilde{v})^2+(\partial_z\tilde{v})^2\right]dydz.\end{aligned} \tag{2.127}$$

Using periodicity in the z-direction and noting that $\tilde{v}\partial_y\tilde{v}\Big|_{y=1^-}=-\tilde{v}\partial_z\tilde{w}\Big|_{y=1^-}=O(\Delta^6)$ and similarly for the term evaluated at $y=0^+$, while the term on the left of (2.127) is at least $O(\Delta^4)$:

$$\begin{aligned}\int_0^{L_z/2}\int_{0^+}^{1^-}\left[\tilde{v}\nabla_\perp^2\tilde{v}\right]dydz &= -\int_0^{L_z/2}\int_{0^+}^{1^-}\left[(\partial_y\tilde{v})^2+(\partial_z\tilde{v})^2\right]dydz,\\ &= -\int_0^{L_z/2}\int_{0^+}^{1^-}(\nabla_\perp\tilde{v})^2 dydz.\end{aligned} \tag{2.128}$$

Collecting these various results, (2.123) simplifies to

$$-2\int_0^{L_z/2}\tilde{w}\partial_y\tilde{w}\Big|_{y=0^+}dz = \int_0^{L_z/2}\int_{0^+}^{1^-}\left[(\nabla_\perp\tilde{v})^2+(\nabla_\perp\tilde{w})^2\right]dydz, \tag{2.129}$$

where each term is $O(\Delta^4)$. Physically, (2.129) indicates that the work done by the viscous stress at the edge of the CL is balanced by the viscous dissipation of roll kinetic energy in the interior of each roll cell.

The dissipation integral on the right-hand side of (2.129) can be further simplified, as we now demonstrate:

$$\begin{aligned}&\int_0^{L_z/2}\int_{0^+}^{1^-}\left[(\nabla_\perp\tilde{v})^2+(\nabla_\perp\tilde{w})^2\right]dydz\\ &\quad=\int_0^{L_z/2}\int_{0^+}^{1^-}\left[(\partial_y\tilde{w})^2-2(\partial_y\tilde{w})(\partial_z\tilde{v})+(\partial_z\tilde{v})^2+(\partial_z\tilde{w})^2+2(\partial_y\tilde{w})(\partial_z\tilde{v})+(\partial_y\tilde{v})^2\right]dydz,\\ &\quad=\int_0^{L_z/2}\int_{0^+}^{1^-}(\partial_y\tilde{w}-\partial_z\tilde{v})^2\,dydz+2\int_0^{L_z/2}\int_{0^+}^{1^-}(\partial_y\tilde{w})(\partial_z\tilde{v})dydz\\ &\quad\quad+\int_0^{L_z/2}\int_{0^+}^{1^-}\left[(\partial_z\tilde{w})^2+(\partial_y\tilde{v})^2\right]dydz.\end{aligned} \tag{2.130}$$

We use integration by parts to recognize that

$$2\int_0^{L_z/2}\int_{0^+}^{1^-}(\partial_y\tilde{w})(\partial_z\tilde{v})dydz = 2\int_0^{L_z/2}\int_{0^+}^{1^-}(\partial_y\tilde{v})(\partial_z\tilde{w})dydz. \tag{2.131}$$

Substituting (2.131) into (2.130) yields

$$\begin{aligned}\int_0^{L_z/2}\int_{0^+}^{1^-}\left[(\nabla_\perp\tilde{v})^2+(\nabla_\perp\tilde{w})^2\right]dydz &= \int_0^{L_z/2}\int_{0^+}^{1^-}(\partial_y\tilde{w}-\partial_z\tilde{v})^2\,dydz\\ &\quad+\int_0^{L_z/2}\int_{0^+}^{1^-}(\partial_y\tilde{v}+\partial_z\tilde{w})^2\,dydz.\end{aligned} \tag{2.132}$$

Using incompressibility to eliminate the last integral, and noting, asymptotically, the core vorticity $(\partial_y \tilde{w} - \partial_z \tilde{v}) \approx 1$, we obtain

$$\begin{aligned}\int_0^{L_z/2} \int_{0^+}^{1^-} \left[(\nabla_\perp \tilde{v})^2 + (\nabla_\perp \tilde{w})^2\right] dydz &= \int_0^{L_z/2} \int_{0^+}^{1^-} dydz \\ &= \frac{L_z}{2}.\end{aligned} \tag{2.133}$$

Substituting into (2.129) then yields

$$-2\int_0^{L_z/2} (\tilde{w}\partial_y \tilde{w})\,|_{y=0^+} dz = \frac{L_z}{2}. \tag{2.134}$$

From the analysis of the fluctuation dynamics within the CL (section 2.4.2), recall the vorticity jump across the CL expression as

$$\left[\partial_{\mathcal{Y}} \tilde{\mathcal{W}}_3\right]_-^+ = \frac{4n_0 \mathcal{A}^2 \tilde{\alpha}^{1/3}}{\overline{\Omega}_c^{7/3}} \partial_z \left(\frac{A^2 \tilde{\beta}^2 \tilde{\lambda}^{1/3}}{\tilde{k}^4}\right). \tag{2.135}$$

Using (2.134) along with the expression for $\tilde{w}|_{y=0^+}$ given in (2.18) yields

$$16\int_0^{L_z/2} \left(\frac{n_0 \mathcal{A}^2 \tilde{\alpha}^{1/3}}{\overline{\Omega}_c^{7/3}} \partial_z \left(\frac{A^2 \tilde{\beta}^2 \tilde{\lambda}^{1/3}}{\tilde{k}^4}\right) \sum_{n=0}^{n=\infty} \left[\frac{L_z}{n^2\pi^2} \tanh\left(\frac{n\pi}{L_z}\right) \sin\left(\frac{2n\pi z}{L_z}\right)\right]\right) dz = \frac{L_z}{2}. \tag{2.136}$$

Finally, rearranging (2.136), we obtain an equation for $\overline{\Omega}_c$:

$$\overline{\Omega}_c^{7/3} = \frac{32\mathcal{A}^2 n_0 \tilde{\alpha}^{1/3}}{\pi^2} \int_0^{L_z/2} \left(\partial_z \left(\frac{A^2 \tilde{\beta}^2 \tilde{\lambda}^{1/3}}{\tilde{k}^4}\right) \sum_{n=0}^{n=\infty} \left[\frac{1}{n^2} \tanh\left(\frac{n\pi}{L_z}\right) \sin\left(\frac{2n\pi z}{L_z}\right)\right]\right) dz. \tag{2.137}$$

This expression relates $\overline{\Omega}_c$ to known or computable quantities, thereby closing the problem for the construction of inertial ECS.

2.6 Summary

Figure 2.6 provides a schematic representation of the new self-sustaining process supporting UMZs and VFs in the inertial domain of turbulent wall flows as deduced from the asymptotic analysis.

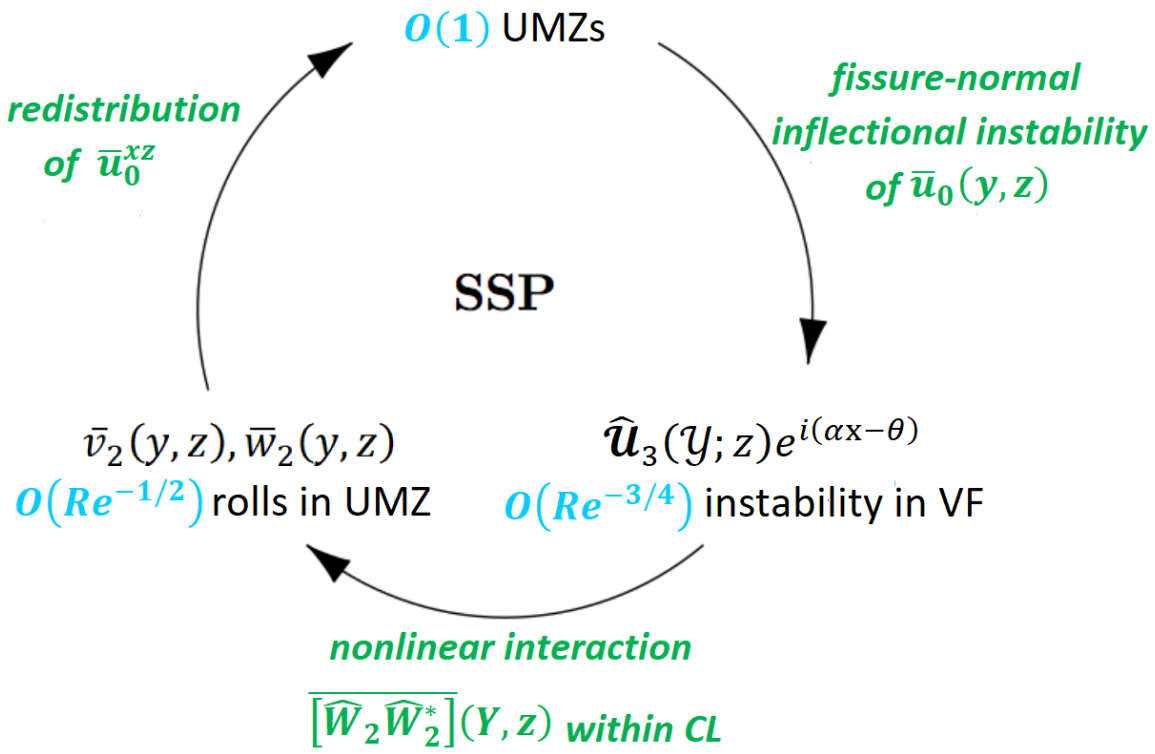

Figure 2.6: Schematic diagram of a mechanistic self-sustaining process for UMZs and VFs in the inertial domain of turbulent wall flows. The feedback loop shown indicates that rolls having $O(Re^{-1/2})$ circulation strength redistribute the background shear flow to induce an $O(1)$ inflected streamwise flow. The counter-rotating and stacked rolls are sufficiently strong to differentially homogenize the background flow, thereby creating and maintaining both UMZs and internal shear layers (VFs). The wall-normal (y) inflections in the streamwise-mean streamwise velocity support an $O(Re^{-3/4})$ Rayleigh (inviscid shear) instability mode that has a streamwise (x) wavelength $2\pi/\alpha \ll 1$ that is commensurate with the VF thickness. Consequently, the Rayleigh mode is confined to the VF, where it is refracted and rendered three-dimensional by the comparably slow spanwise variation in the fissure thickness, and the resulting ECS are inherently multiscale. The 3D Rayleigh mode suffers a critical-layer singularity, causing the magnitude of the x-varying spanwise velocity component to be amplified to $O(Re^{-1/2})$. The resulting nonlinear self-interaction of the Rayleigh mode within the CL drives the roll motions in the UMZs through a modulational (i.e. slow spanwise) Reynolds stress divergence involving this velocity component.

Field	**UMZ**: $y = O(1)$	**VF**: $y = O(\Delta) = O(Re^{-1/4})$	**CL**: $y = O(\delta) = O(Re^{-1/2})$
$\bar{u}$	1	1	$Re^{-1/4}$
$\bar{v}$	$Re^{-1/2}$	$Re^{-3/4}$	Re^{-1}
$\bar{w}$	$Re^{-1/2}$	$Re^{-1/2}$	$Re^{-1/2}$
$\bar{\Omega}$	$Re^{-1/2}$	$Re^{-1/2}$	$Re^{-1/2}$
$\bar{p}$	Re^{-1}	Re^{-1}	Re^{-1}
u'	$E.S.T.$	$Re^{-3/4}$	$Re^{-1/2}$
v'	$E.S.T.$	$Re^{-3/4}$	$Re^{-3/4}$
w'	$E.S.T.$	$Re^{-3/4}$	$Re^{-1/2}$
p'	$E.S.T.$	$Re^{-3/4}$	$Re^{-3/4}$

Table 2.2: Summary of the scalings of the mean and fluctuation fields in each of the three fissure-normal subdomains: UMZ = Uniform Momentum Zone; VF = Vortical Fissure / Internal Shear Layer; and CL = Critical Layer.

Table 2.2 summarizes the scalings associated with the analysis of each of the subdomains (UMZs, VFs, and CLs).

Physically, the counter-rotating and stacked rolls are sufficiently strong to differentially homogenize the background flow, thereby creating and maintaining both $O(1)$ UMZs and internal shear layers of thickness Δ, where $\Delta(Re) \to 0$ as $Re \to \infty$. Because the streamwise-varying fluctuation fields are exponentially small within the UMZs, the x-mean rolls and streaks cannot be directly driven there. Instead, in this inertial layer SSP, the driving for the staircase-like profiles of the instantaneous streamwise velocity is confined to the internal layers of concentrated spanwise vorticity, i.e. to the VFs.

The singularities arising in the largely dynamically-inviscid roll/streak flow within the UMZs are regularized by viscous forces and torques acting within emergent internal shear layers (VFs) and streamwise jets, both of dimensionless thickness $O(\Delta)$, acting along the periphery of each cell. In the proposed configuration, no physical boundary exists along the horizontal planes separating rows of stacked counter-rotating rolls. Accordingly, the leading-order mean spanwise velocity component within the VF is not sheared; i.e. $\partial_y \overline{\mathcal{W}}_2 = 0 \to \overline{\mathcal{W}}_2 = \overline{\mathcal{W}}_2(z)$, only. Consequently, the roll vorticity has the same asymptotic size $O(Re^{-1/2})$ within the VF and UMZ ensuring smooth matching of this field is possible.

Within each fissure, the wall-normal (y) inflections in the streamwise-mean streamwise velocity support an $O(Re^{-3/4})$ Rayleigh (inviscid shear) instability mode. The Rayleigh mode has a streamwise (x) wavelength $2\pi/\alpha \ll 1$ that is commensurate with the VF thickness, i.e. $O(Re^{-1/2})$. Consequently, the Rayleigh mode is confined to the VF, where it is refracted and rendered three-dimensional by the comparably slow spanwise variation in the fissure thickness. The resulting multiscale ECS are analyzed using a WKBJ ansatz. The fluctuations satisfy quasilinear equations with respect to the leading-order streak velocity, which can be collapsed into Rayleigh's equation following Squire's transformation. This eigenvalue problem is solved to provide the fluctuation fields within the VF to within some unknown z-varying amplitude. The eigenvalue $\tilde{k}^2$ is the total horizontal wavenumber of the neutral Rayleigh mode, which varies with z since the mean shear $\tilde{\lambda}$ does so. To solve for the slowly spanwise-varying amplitude, the fluctuation fields are analyzed at a higher asymptotic order. It is shown that the amplitude grows in asymptotically thin spanwise regions of the VF known as caustics. Beyond the caustics are shadow regions where the wave amplitude is suppressed. Physically, caustics arise in regions of the flow where the internal shear layer is to diffuse to sustain the Rayleigh instability. By modifying the WKBJ ansatz to include Airy functions, a bounded solution for the fluctuation amplitude within the caustics can be found. The analysis of this region reveals that the instability mode is reflected at the caustics and experiences a $\pi/2$-shift in spanwise phase before re-entering the illuminated region.

Although 2D neutral Rayleigh modes are regular, the 3D Rayleigh mode suffers a critical-layer singularity, causing the magnitude of the x-varying spanwise velocity component to be amplified. The resulting nonlinear self-interaction of the Rayleigh mode within the CL induces a jump in the x-mean vorticity through a modulational Reynolds stress divergence driving roll motions within the UMZs. The core vorticity $\overline{\Omega}_c$ is found from a mean kinetic energy budget obtained by integrating over a single roll cell *excluding* the CLs at $y = 0, 1$. It is shown that the work done by the mean viscous stress at edge of each CL is balanced by dissipation of the roll kinetic energy within UMZ, thereby closing the analysis.

In summary, the overarching objective of this asymptotic analysis has been to probe the governing Navier–Stokes equations in the limit of large Re in search of a mechanistic self-sustaining process (SSP) theory that

(i) can account for the emergent staircase-like profile of streamwise velocity in the inertial region; and

(ii) is compatible with the singular nature of turbulent wall flows.

This objective has been achieved via identification of the new, multiscale inertial-layer SSP described here. Next, in chapter 3, the numerical methods used to solve for ECS supported by this new SSP are reviewed. In chapter 4, the results of these computations are described.

CHAPTER 3

NUMERICAL METHODS

3.1 Introduction

In the previous chapter, a detailed asymptotic analysis was performed in the dual limit of large Reynolds number and large streamwise wavenumber to derive a mechanistic SSP that can account for the UMZs and VFs observed in the inertial region of the turbulent boundary layers. This chapter describes the numerical methods used to solve the resulting asymptotically reduced equations. In particular, the solution of the Childress cell problem is replaced by the large (but finite) Re solution of the steady advection–diffusion equation (2.19) for the leading-order streak velocity over the entire spatial domain. It proves more convenient to extract the full (2D) streak velocity field within the VF in this manner than to attempt to reconstruct this field (rather just the streak shear $\tilde{\lambda}(z)$ at the VF centreline) from the formal solution to the Childress cell problem. This finite-Re approach is justified in section 3.3.1. Moreover, it should be noted that reconstructions of the ECS, presented in the next chapter, necessarily must be generated at large, but finite Re, since the Rayleigh mode and the rolls are asymptotically small relative to the streak field. Spectral numerical methods are employed to obtain the required steady solutions to 2D PDEs, to solve eigenvalue problems for the Rayleigh mode in the VF, and to evaluate quadratures for the stress jump across the CL and coefficients in the amplitude equation. The various numerical techniques in each subdomain of the flow (UMZ, VF, CL) will be summarized in sequence.

3.2 Uniform Momentum Zones

The dynamics within the UMZs are governed by the 2D (x-independent) but three-component NS equations, (2.19)–(2.20) repeated below for ease of reference, since the streamwise-varying fluctuation fields are exponentially small:

$$(\tilde{\mathbf{v}}_{2\perp} \cdot \nabla_\perp)\, \overline{u}_0 \;=\; \tilde{\Delta}^2 \nabla_\perp^2 \overline{u}_0, \tag{3.1}$$

$$(\tilde{\mathbf{v}}_{2\perp} \cdot \nabla_\perp)\, \tilde{\mathbf{v}}_{2\perp} \;=\; -\nabla_\perp \tilde{p}_4 \,+\, \tilde{\Delta}^2 \nabla_\perp^2 \tilde{\mathbf{v}}_{2\perp}. \tag{3.2}$$

The key simplification resulting from the homogenization of the roll vorticity is that the roll velocity components $(\bar{v}, \bar{w})$ can be analytically determined up to an unknown constant prefactor $\overline{\Omega}_c$. By employing the alternative small parameter $\tilde{\Delta} = (Re\overline{\Omega}_c)^{-1/4}$ and expressing the mean fields as $\overline{v} = \overline{\Omega}_c \tilde{v}$, $\overline{w} = \overline{\Omega}_c \tilde{w}$, and $\overline{p} = \overline{\Omega}_c^2 \tilde{p}$, the unknown constant $\overline{\Omega}_c$ is removed from the equations for $(\tilde{v}, \tilde{w})$; see (3.2). With this change, as shown in Chini (2008), the rescaled version of (2.10) is readily solved analytically in a rectangular domain of (asymptotically) known dimensions one unit in y and $L_z/2$ units in z, where again L_z is the prescribed spanwise periodicity length of the rolls. The solution for $\tilde{v}$ and $\tilde{w}$ given in (2.17) and (2.18) is repeated here:

$$\tilde{v}_2 \;=\; \sum_{n=1,odd}^{\infty} \frac{2L_z}{(n\pi)^2} \left[\frac{\cosh[(2n\pi/L_z)(1/2-y)]}{\cosh(n\pi/L_z)} - 1 \right] \cos\left(\frac{2n\pi z}{L_z}\right), \tag{3.3}$$

$$\tilde{w}_2 \;=\; \sum_{n=1,odd}^{\infty} \frac{2L_z}{(n\pi)^2} \left[\frac{\sinh[(2n\pi/L_z)(1/2-y)]}{\cosh(n\pi/L_z)} \right] \sin\left(\frac{2n\pi z}{L_z}\right). \tag{3.4}$$

Crucially, ($\tilde{v}_2$, $\tilde{w}_2$) therefore can be self-consistently prescribed in the reduced x-momentum equation (3.1), with $\overline{u}_0$ behaving as a passive scalar that is advected and diffused around the cell. Here, the solution for $\overline{u}_0$ is obtained as the steady-state solution of the time-dependent version of (3.1) after first decomposing the mean streamwise velocity into a background Couette profile and a finite amplitude fluctuation $\bar{u}$ such that $\overline{u}_0 = y + \overline{u}$. Thus within the UMZ and VF subdomains, $\bar{u}$ satisfies

$$\partial_t \overline{u} + \tilde{v}_2 + (\tilde{\mathbf{v}}_{2\perp} \cdot \nabla_\perp)\, \overline{u} = \tilde{\Delta}^2 \nabla_\perp^2 \overline{u} \tag{3.5}$$

subject to homogeneous Dirichlet symmetry conditions at $y = 0$ and $y = 1$ and periodic boundary conditions in the spanwise direction:

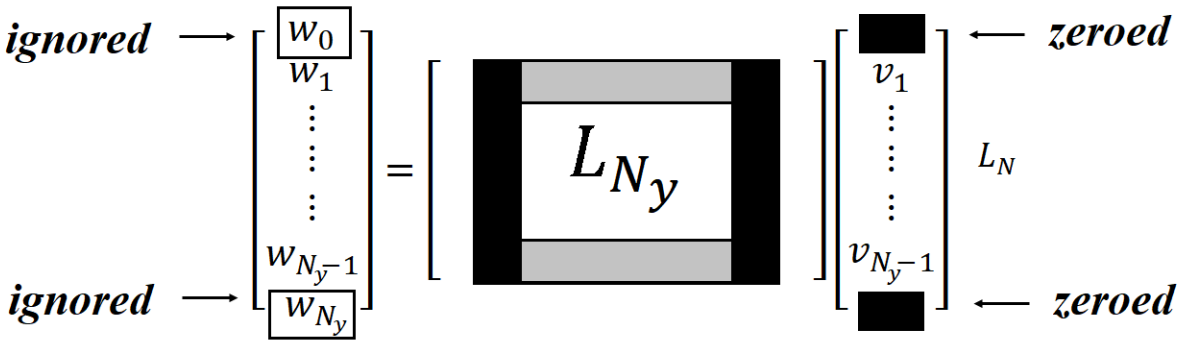

Figure 3.1: Schematic demonstrating how homogeneous Dirichlet boundary conditions are implemented in a Chebyshev discretization method, resulting in the zeroing of certain rows and columns (adapted from Trefethen (2000)).

$$\overline{u} = 0 \quad \text{along} \quad y = 0, \tag{3.6}$$

$$\overline{u} = 0 \quad \text{along} \quad y = 1, \tag{3.7}$$

$$\overline{u}(y, -L_z/2) = \overline{u}(y, L_z/2) \quad \text{(periodicity)}. \tag{3.8}$$

To solve (3.5) subject to (3.6)–(3.8), a Fourier pseudospectral discretization is used for the spanwise (z) direction, while a Chebyshev collocation scheme is implemented in the fissure-normal y direction. As Figure 3.1 demonstrates, when enforcing homogeneous Dirichlet conditions in a Chebyshev collocation scheme, the first and last columns of the discrete linear operator (L_{Ny}) have no effect since they are multiplied by zero; moreover, the first and last rows are not needed, since the first and last values of the vector of unknowns (v_0 and v_{Ny}) are known, yielding an $(N_y - 1)$ x $(N_y - 1)$ matrix operator, where $N_y + 1$ is the number of Chebyshev grid points (Trefethen, 2000). While the Fourier grid is equispaced, the Chebyshev discretization is defined on the computational domain $Y_c \in [-1, 1]$ with discrete grid points $Y_j = \cos(j\pi/N_y)$, where $j = 0, 1, ..., N_y$. The computational and physical domains are relocated via the mapping $Y_c = 2y - 1$ where $0 \leq y \leq 1$. The distribution of grid points associated with the Chebyshev discretization is advantageous, since the points are clustered at the edges of the domain near $y = 0$ and $y = 1$, which coincide with the locations of the internal shear layers.

$\kappa = 2\pi/L_z$	0.75	0.76	0.775	0.785	0.8	0.875	1	1.25	1.3	1.4
N_y	1500	750	750	750	750	750	750	1500	750	750
N_z	450	400	400	400	400	400	400	400	400	400
$\kappa = 2\pi/L_z$	1.5	2	2.5	π	3.25	3.5	4.5	6	6.75	10
N_y	750	750	750	1500	750	750	750	1500	1500	1500
N_z	400	400	400	300	400	400	400	200	200	200

Table 3.1: Summary of the discretization used in the numerical solution of (3.5) for $\overline{u}_0(y,z)$ regularized by the inclusion of Laplacian diffusion $\tilde{\Delta} = O(10^{-4})$.

To study the impact of the cell width (L_z), or equivalently aspect ratio, on the x-mean vorticity, a range of spanwise roll-pair wavenumbers $\kappa \equiv \frac{2\pi}{L_z} = 0.75$ through $\kappa = 10$ is simulated. The spatial discretization $[N_y, N_z]$ used for each L_z value is shown in Table 3.1.

Equation (3.5) is discretized in time using a semi-implicit second-order accurate finite-difference scheme. The linear terms are time-advanced using the Crank-Nicolson method, while the nonlinear terms are advanced using a second-order Adams-Bashforth method. Recall that the Crank-Nicolson scheme is a second order implicit method for the model ODE $\frac{du}{dt} = F(u)$,

$$u^{n+1} = u^n + \frac{\Delta t}{2}\left[F(u^{n+1}) + F(u^n)\right], \tag{3.9}$$

while the Adams-Bashforth scheme used here is the second order explicit method

$$u^{n+1} = u^n + \frac{\Delta t}{2}\left[3F(u^n) - F(u^{n-1})\right], \tag{3.10}$$

where $u^n = u(n\Delta t)$ for integer n and Δt is the time step.

3.3 Vortical Fissures

As demonstrated below, for sufficiently small numerical values of $\tilde{\Delta}^2$, the numerically-computed solution $\overline{u}_0 = y + \overline{u}$ yields a quantitatively reliable approximation to $\overline{\mathcal{U}}_0(\mathcal{Y}, z)$ within the internal shear layers (VFs). Recall that within the VF there is a new dominant force balance in which viscous forces are significant, thereby regularizing discontinuities in the mean fields at the periphery

$\kappa = 2\pi/L_z$	0.75	0.76	0.775	0.785	0.8	0.875	1	1.25	1.3	1.4
N_y	750	750	750	750	750	750	750	750	750	750
N_z	2000	2000	2000	2000	2000	2000	2000	2000	2000	2000
$\kappa = 2\pi/L_z$	1.5	2	2.5	π	3.25	3.5	4.5	6	6.75	10
N_y	750	750	750	750	750	750	750	750	750	750
N_z	750	2000	2000	1600	2000	2000	2000	1100	1100	1100

Table 3.2: Summary of the discretization used for solving Rayleigh's (eigenvalue) stability equation within the VF domain.

of each cell. The resulting (steady) $\overline{\mathcal{U}}_0(\mathcal{Y}, z)$ is then used as an input to the Rayleigh equation (eigenvalue problem) for the fluctuations within the VFs. The spanwise domain for this region remains $-L_z/2 \leq z \leq L_z/2$; however, the (re-scaled) fissure normal coordinate ranges over $0 \leq \mathcal{Y} \leq \infty$ where $y = \tilde{\Delta}\mathcal{Y}$. The spatial discretization $[N_y, N_z]$ used for each L_z value within the VF is shown in Table 3.2.

3.3.1 Mean Fields

To obtain the true streak velocity field within each VF in the asymptotic limit $Re \to \infty$, the Childress cell problem formulated in section 2.3.1 must be solved. Here, in figure 3.2, the solution for $\tilde{\lambda}(z)$ obtained from the solution of the Childress cell problem given by Chini & Cox (2009), i.e. in the limit $Re \to \infty$, is compared to that obtained by numerically solving the advection–diffusion equation (3.5) for small but finite $\tilde{\Delta}^2$ (corresponding to large but finite Re) as a means of validating the two independent calculations. The two profiles agree closely except at $z = 0$, where diffusion heals a passive singularity arising in the solution of the Childress cell problem. This validation enables the finite-Re data (i.e. with viscous regularization) to be used in the calculation of the fluctuation velocities within the VF, considered next. This strategy proves to be more convenient and robust than attempting to directly reconstruct $\overline{\mathcal{U}}_0(\mathcal{Y}, z)$ from the solution of the Childress cell problem.

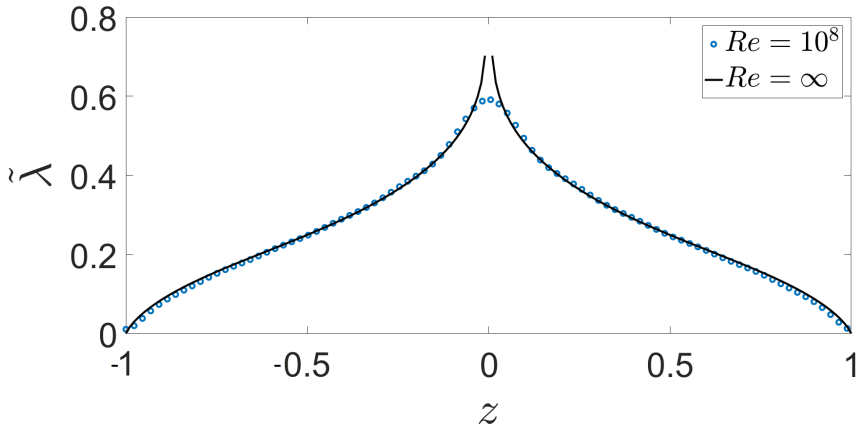

Figure 3.2: Normalized streak-induced shear $\tilde{\lambda}(z) \equiv \partial_{\mathcal{Y}} \overline{\mathcal{U}}_0(0, z)$ at the mid-plane of the VF obtained from the solution of the Childress cell problem (i.e. in the limit $Re \to \infty$, solid curve) and from the numerical solution of the full advection–diffusion equation (2.19) [or, equivalently, (3.5)] for finite Re (dotted curve).

3.3.2 Fluctuation Fields

The fluctuation fields within the VFs are defined by the WKBJ ansatz

$$\begin{bmatrix} \mathcal{U}_3' \\ \mathcal{V}_3' \\ \mathcal{W}_3' \\ \mathcal{P}_3' \end{bmatrix} = \mathcal{A} \begin{bmatrix} \hat{\mathcal{U}}_3(\mathcal{Y}; z) \\ \hat{\mathcal{V}}_3(\mathcal{Y}; z) \\ \hat{\mathcal{W}}_3(\mathcal{Y}; z) \\ \hat{\mathcal{P}}_3(\mathcal{Y}; z) \end{bmatrix} A(z)\, \mathrm{e}^{i[\tilde{\alpha}/\tilde{\Delta}(x-ct)+\theta(z/\tilde{\Delta})]} + c.c.,$$

where the scalar amplitude of the wave $\mathcal{A}$ and streamwise wavenumber $\tilde{\alpha}$ are inputs. The (hatted) eigenfunctions along with the spanwise wavenumber $\tilde{\beta} \equiv \partial_z \theta$, where $\theta(z/\tilde{\Delta}) \equiv \theta(z)/\tilde{\Delta}$, and the amplitude modulation function $A(z)$ must be computed. Since a neutral Rayleigh mode is sought, the imaginary part of the Rayleigh mode phase speed c is set to zero. For the VF at $\mathcal{Y} = 0$, analyzed here, the real part of c also is set to zero, although, more generally, for the VF located at $y = n$ (for integer n), $c = n$. Squire's transformation is employed to simplify the resulting eigenvalue problem, where

$$\tilde{k} = \sqrt{\tilde{\alpha}^2 + \tilde{\beta}^2}, \qquad \tilde{k}\hat{\mathcal{P}}_3 = \tilde{\alpha}\hat{\Pi}_3,$$
$$\tilde{k}\hat{\mathcal{U}}_{3r} = \tilde{\alpha}\hat{\mathcal{U}}_3 + \tilde{\beta}\hat{\mathcal{W}}_3 \qquad \Longleftrightarrow \qquad \tilde{k}\hat{\mathcal{U}}_3 = \tilde{\alpha}\hat{\mathcal{U}}_{3r} - \tilde{\beta}\hat{\mathcal{W}}_{3r}, \tag{3.11}$$
$$\tilde{k}\hat{\mathcal{W}}_{3r} = \tilde{\alpha}\hat{\mathcal{W}}_3 - \tilde{\beta}\hat{\mathcal{U}}_3 \qquad \Longleftrightarrow \qquad \tilde{k}\hat{\mathcal{W}}_3 = \tilde{\beta}\hat{\mathcal{U}}_{3r} + \tilde{\alpha}\hat{\mathcal{W}}_{3r}.$$

In the rotated ('r') coordinates, Rayleigh's equation

$$\partial_{\mathcal{Y}}^2\phi - \frac{\partial_{\mathcal{Y}}^2\overline{\mathcal{U}}_0}{\left(\overline{\mathcal{U}}_0 - c\right)}\phi = \tilde{k}^2\phi, \tag{3.12}$$

is obtained (see section 2.3.2), where $\tilde{k}\hat{\mathcal{U}}_{3r} \equiv \partial_{\mathcal{Y}}\phi$ and $\hat{\mathcal{V}}_3 \equiv -i\phi$. This equation is solved repeatedly at each (discrete) z location as an eigenvalue problem for $\tilde{k}$ and ϕ using a Chebyshev collocation method in conjunction with Matlabs QZ ('eig') algorithm. The required values for the mean streamwise velocity are obtained by interpolating the solution $\overline{u}_0$ onto a grid in the VF region (see table 3.2 for discretization details). At a given spanwise location, the fissure-normal grid used for interpolation ranges over $0 \leq y \leq 0.3$, which approximately translates to $0 \leq \mathcal{Y} \leq 30$ for the given (finite) $Re(\tilde{\Delta})$. The domain includes (half of) the VF and extends into the UMZ where the fluctuations reach exponentially small values. (Recall that the fluctuations approach zero exponentially as they leave the fissure.) Noting from symmetry that $\hat{\mathcal{U}}_{3r} \to 0$ as $\mathcal{Y} \to 0$, the boundary conditions applied to ϕ are

$$\phi \to 0 \qquad \text{as} \qquad \mathcal{Y} \to \infty, \tag{3.13}$$
$$\partial_{\mathcal{Y}}\phi = 0 \qquad \text{at} \qquad \mathcal{Y} = 0. \tag{3.14}$$

The sole positive real eigenvalue ($\tilde{k}^2(z)$) and corresponding eigenfunction ($\phi(\mathcal{Y}, z)$) at each z location are selected. Note that, given the ansatz $e^{i[\tilde{\alpha}/\tilde{\Delta}(x-ct)+\theta(z/\tilde{\Delta})]}$, only real $\tilde{k}$ are admissible; complex values of $\tilde{k}$ would result in complex θ and blow-up of the fluctuations either as $z \to -\infty$ or as $z \to \infty$. The relationship between $\tilde{k}(z)$, the spanwise wavenumber $\tilde{\beta}(z)$, and the streamwise wavenumber $\tilde{\alpha}$ is given by (3.11). In particular, the spanwise wavenumber $\tilde{\beta}(z)$ is then calculated using the Eikonal equation with the streamwise wavenumber $\tilde{\alpha}$ specified as an input and

$\tilde{k}$ calculated through the solution of the eigenvalue problem (3.12). Integration of the spanwise wavenumber $\tilde{\beta}(z)$ yields the phase $\theta(z)$. Finally, noting $\hat{\mathcal{W}}_{3r} \equiv \frac{1}{i\tilde{k}}\frac{\tilde{\beta}}{\tilde{\alpha}}\frac{\hat{\mathcal{V}}_3 \partial_{\mathcal{Y}}\overline{\mathcal{U}_0}}{\overline{\mathcal{U}}_0 - c}$ allows for each fluctuation velocity-component eigenfunction to be calculated in the rotated frame.

To find the slowly-varying amplitude $A(z)$ using $\overline{\mathcal{U}}_0$, $\hat{\mathcal{V}}_3$, and $\hat{\mathcal{U}}_{3r}$, we first calculate the coefficents a_z and a_0. Recalling the definitions

$$a_z = -2i\tilde{\beta}\int_{-\infty}^{\infty} \hat{\mathcal{V}}_3 \hat{\mathcal{V}}_3^* d\mathcal{Y}, \tag{3.15}$$

$$\begin{aligned} a_0 &= -i\int_{-\infty}^{\infty} \left[2\tilde{\beta}\partial_z(\hat{\mathcal{V}}_3)\hat{\mathcal{V}}_3^* + (\partial_z\tilde{\beta})\hat{\mathcal{V}}_3\hat{\mathcal{V}}_3^* - 2\frac{\tilde{\beta}}{\tilde{k}^2}\partial_{\mathcal{Y}}\left(\frac{\partial_z\overline{\mathcal{U}}_0}{\overline{\mathcal{U}}_0 - c}\right)(\partial_{\mathcal{Y}}\hat{\mathcal{V}}_3)\hat{\mathcal{V}}_3^* \right. \\ &+ \left. 2\frac{\tilde{\beta}}{\tilde{k}^2}\partial_{\mathcal{Y}}\left(\frac{\partial_z\overline{\mathcal{U}}_0}{\overline{\mathcal{U}}_0 - c}\right)\left[\frac{\hat{\mathcal{V}}_3\hat{\mathcal{V}}_3^*\partial_{\mathcal{Y}}\overline{\mathcal{U}_0}}{\overline{\mathcal{U}}_0 - c}\right]\right] d\mathcal{Y}, \end{aligned} \tag{3.16}$$

cf. (2.75) and (2.76), the required numerical integrations are performed using Matlab's 'trapz' function at each z location. With a_z and a_0 determined, a further numerical integration yields the amplitude function

$$A(z) = \exp\left(-\int_0^z \frac{a_0}{a_z}dz\right) \tag{3.17}$$

Once the eigenfunctions corresponding to the individual components of the fluctuating velocity have been determined, the velocity fields in the original (non-rotated) coordinate system can be reconstructed using (3.11). Then by incorporating the complex conjugate expressions and phase shift induced at the caustics, the fluctuating velocity fields can be derived as follows. To find $\mathcal{U}_3'$ we designate a hatted fluctuation field corresponding to $\tilde{\beta} > 0$ with a '+' superscript and conversely a hatted fluctuation field corresponding to $\tilde{\beta} < 0$ is denoted by a '-' superscript. Consequently, $\hat{\mathcal{U}}_3 = \hat{\mathcal{U}}^+$, $\hat{\mathcal{V}}_3 = \hat{\mathcal{V}}^+$, and $\hat{\mathcal{W}}_3 = \hat{\mathcal{W}}^+$ and,

$$\begin{aligned} \mathcal{U}_3' &= \mathcal{A}\left(A\hat{\mathcal{U}}_3^+ e^{i(\alpha x + \hat{\theta})} + A\hat{\mathcal{U}}_3^+ e^{i(\alpha x + \hat{\theta} + \frac{\pi}{2})} + A\hat{\mathcal{U}}_3^- e^{i(\alpha x - \hat{\theta})} + A\hat{\mathcal{U}}_3^+ e^{i(\alpha x - \hat{\theta} - \frac{\pi}{2})} + c.c.\right), \\ &= 2\mathcal{A}A\hat{\mathcal{U}}_3^+ \cos(\alpha x + \hat{\theta}) + 2\mathcal{A}A\hat{\mathcal{U}}_3^- \cos(\alpha x - \hat{\theta}), \\ &+ 2\mathcal{A}A\hat{\mathcal{U}}_3^+ \cos(\alpha x + \hat{\theta} + \frac{\pi}{2}) + 2\mathcal{A}A\hat{\mathcal{U}}_3^- \cos(\alpha x - \hat{\theta} - \frac{\pi}{2}), \end{aligned} \tag{3.18}$$

where $\hat{\theta} = \theta + \pi/4$. Noting that $\hat{\mathcal{U}}_3^+ = \hat{\mathcal{U}}_3^-$ from (2.38) upon mapping $\tilde{\beta} \to -\tilde{\beta}$,

$$\begin{aligned}
\mathcal{U}_3' &= 2\mathcal{A}A\hat{\mathcal{U}}_3^+ \left[\cos(\alpha x + \hat{\theta}) + \cos(\alpha x - \hat{\theta})\right] + 2\mathcal{A}A\hat{\mathcal{U}}_3^+ \left[\cos(\alpha x + \hat{\theta} + \frac{\pi}{2}) + \cos(\alpha x - \hat{\theta} - \frac{\pi}{2})\right], \\
&= 4\mathcal{A}A\hat{\mathcal{U}}_3^+ \cos(\alpha x)\cos(\hat{\theta}) - 2\mathcal{A}A\hat{\mathcal{U}}_3^+ \left[\sin(\alpha x + \hat{\theta}) - \sin(\alpha x - \hat{\theta})\right], \\
&= 4\mathcal{A}A\hat{\mathcal{U}}_3^+ \left[\cos(\alpha x)\cos(\hat{\theta}) - \sin(\hat{\theta})cos(\alpha x)\right], \\
&= 4\mathcal{A}A\hat{\mathcal{U}}_3^+ \left[\cos\left(\theta + \frac{\pi}{4}\right) - \sin\left(\theta + \frac{\pi}{4}\right)\right]\cos(\alpha x), \\
&= 4\sqrt{2}\mathcal{A}A\hat{\mathcal{U}}_3^+ \sin(\theta)\cos(\alpha x).
\end{aligned} \tag{3.19}$$

Next, solving for $\mathcal{V}_3'$, we obtain

$$\begin{aligned}
\mathcal{V}_3' &= \mathcal{A}\left(A\hat{\mathcal{V}}_3^+ e^{i(\alpha x + \hat{\theta})} + A\hat{\mathcal{V}}_3^+ e^{i(\alpha x + \hat{\theta} + \frac{\pi}{2})} + A\hat{\mathcal{V}}_3^- e^{i(\alpha x - \hat{\theta})} + A\hat{\mathcal{V}}_3^+ e^{i(\alpha x - \hat{\theta} - \frac{\pi}{2})} + c.c.\right), \\
&= 2i\mathcal{A}A\hat{\mathcal{V}}_3^+ \sin(\alpha x + \hat{\theta}) + 2i\mathcal{A}A\hat{\mathcal{V}}_3^- \sin(\alpha x - \hat{\theta}), \\
&+ 2i\mathcal{A}A\hat{\mathcal{V}}_3^+ \sin(\alpha x + \hat{\theta} + \frac{\pi}{2}) + 2i\mathcal{A}A\hat{\mathcal{V}}_3^- \sin(\alpha x - \hat{\theta} - \frac{\pi}{2}).
\end{aligned} \tag{3.20}$$

Since $\hat{\mathcal{V}}_3^+ = \hat{\mathcal{V}}_3^-$,

$$\begin{aligned}
\mathcal{V}_3' &= 2i\mathcal{A}A\hat{\mathcal{V}}_3^+ \left[\sin(\alpha x + \hat{\theta}) + \sin(\alpha x - \hat{\theta})\right] + 2i\mathcal{A}A\hat{\mathcal{V}}_3^+ \left[\sin(\alpha x + \hat{\theta} + \frac{\pi}{2}) + \sin(\alpha x - \hat{\theta} - \frac{\pi}{2})\right], \\
&= 4i\mathcal{A}A\hat{\mathcal{V}}_3^+ \sin(\alpha x)\cos(\hat{\theta}) + 2i\mathcal{A}A\hat{\mathcal{V}}_3^+ \left[\cos(\alpha x + \hat{\theta}) - \cos(\alpha x - \hat{\theta})\right], \\
&= 4i\mathcal{A}A\hat{\mathcal{V}}_3^+ \sin(\alpha x)\cos(\hat{\theta}) - 4i\mathcal{A}A\hat{\mathcal{V}}_3^+ \sin(\alpha x)\sin(\hat{\theta}), \\
&= 4i\mathcal{A}A\hat{\mathcal{V}}_3^+ \sin(\alpha x)\left[\cos\left(\theta + \frac{\pi}{4}\right) - \sin\left(\theta + \frac{\pi}{4}\right)\right], \\
&= 4\sqrt{2}i\mathcal{A}A\hat{\mathcal{V}}_3^+ \sin(\alpha x)\sin(\theta).
\end{aligned} \tag{3.21}$$

Finally, we solve for $\mathcal{W}_3'$:

$$\begin{aligned}
\mathcal{W}_3' &= \mathcal{A}\left(A\hat{\mathcal{W}}_3^+ e^{i(\alpha x + \hat{\theta})} + A\hat{\mathcal{W}}_3^+ e^{i(\alpha x + \hat{\theta} + \frac{\pi}{2})} + A\hat{\mathcal{W}}_3^- e^{i(\alpha x - \hat{\theta})} + A\hat{\mathcal{W}}_3^+ e^{i(\alpha x - \hat{\theta} - \frac{\pi}{2})} + c.c.\right), \\
&= 2\mathcal{A}A\hat{\mathcal{W}}_3^+ \cos(\alpha x + \hat{\theta}) + 2\mathcal{A}A\hat{\mathcal{W}}_3^- \cos(\alpha x - \hat{\theta}), \\
&+ 2\mathcal{A}A\hat{\mathcal{W}}_3^+ \cos(\alpha x + \hat{\theta} + \frac{\pi}{2}) + 2\mathcal{A}A\hat{\mathcal{W}}_3^- \cos(\alpha x - \hat{\theta} - \frac{\pi}{2}).
\end{aligned} \tag{3.22}$$

Since $\hat{\mathcal{W}}_3^+ = -\hat{\mathcal{W}}_3^-$

$$\begin{aligned}
\mathcal{W}_3' &= 2\mathcal{A}A\hat{\mathcal{W}}_3^+ \left[\cos(\alpha x + \hat{\theta}) - \cos(\alpha x - \hat{\theta})\right] + 2\mathcal{A}A\hat{\mathcal{W}}_3^+ \left[\cos(\alpha x + \hat{\theta} + \frac{\pi}{2}) - \cos(\alpha x - \hat{\theta} - \frac{\pi}{2})\right], \\
&= -4\mathcal{A}A\hat{\mathcal{W}}_3^+ \sin(\alpha x)\sin(\hat{\theta}) - 2\mathcal{A}A\hat{\mathcal{W}}_3^+ \left[\sin(\alpha x + \hat{\theta}) - \sin(\alpha x - \hat{\theta})\right], \\
&= -4\mathcal{A}A\hat{\mathcal{W}}_3^+ \left[\sin(\alpha x)\sin(\hat{\theta}) + \cos(\hat{\theta})\sin(\alpha x)\right], \\
&= -4\mathcal{A}A\hat{\mathcal{W}}_3^+ \left[\cos\left(\theta + \frac{\pi}{4}\right) + \sin\left(\theta + \frac{\pi}{4}\right)\right]\sin(\alpha x), \\
&= -4\sqrt{2}\mathcal{A}A\hat{\mathcal{W}}_3^+ \cos(\theta)\sin(\alpha x).
\end{aligned} \tag{3.23}$$

Consequently, $\mathcal{W}_3'$ is an even function about $z = 0$ while $\mathcal{U}_3'$ and $\mathcal{V}_3'$ are odd.

3.3.3 Caustics

In appendix D, we showed that caustics do not contribute to the integral when calculating $\overline{\Omega}_c$. Accordingly, the detailed solutions for the fluctuation fields in the caustics need not be computed.

3.4 Critical Layers

In section 2.4, it was shown that the vorticity jump in the illuminated region is given by

$$[\partial_{\mathcal{Y}}\tilde{\mathcal{W}}_3]_-^+ = \frac{4n_0\mathcal{A}^2\tilde{\alpha}^{1/3}}{\overline{\Omega}_c^{7/3}}\partial_z\left(\frac{A^2\tilde{\beta}^2\tilde{\lambda}^{1/3}}{\tilde{k}^4}\right). \tag{3.24}$$

Additionally, in the asymptotic analysis of the VF, it was shown that the integrands determining a_z and a_0 (see (3.15) and (3.16)) do not grow within the CL. Therefore, the contributions to these integrals from the CLs are asymptotically small and can be ignored. Hence, no numerical computations need be performed for this subdomain, an important benefit of the analysis.

3.5 Roll-Flow Energy Budget

The (rescaled) homogenized value of the x-mean vorticity ($\overline{\Omega}_c$), which fixes the precise value of the roll-induced circulation, is a primary unknown in this analysis. Since the contributions to the

integral for $\overline{\Omega}_c$ in (2.137) from the caustics and shadow regions are subdominant, the expression therefore simplifies to

$$\overline{\Omega}_c^{7/3} = \frac{32\mathcal{A}^2 n_0 \tilde{\alpha}^{1/3}}{\pi^2} \int_0^{z_c^-} \left(\partial_z \left(\frac{A^2 \tilde{\beta}^2 \tilde{\lambda}^{1/3}}{\tilde{k}^4} \right) \sum_{n=0}^{n=\infty} \left[\frac{1}{n^2} \tanh\left(\frac{n\pi}{L_z} \right) \sin\left(\frac{2n\pi z}{L_z} \right) \right] \right) dz. \quad (3.25)$$

Note that all of the terms on the right-hand side of (3.25) either are numerically computable as described in the preceding sections (namely $\tilde{\beta}(z)$, $A(z)$, and $\tilde{\lambda}(z)$) or are inputs to the problem ($\mathcal{A}$, $\tilde{\alpha}$, and L_z). Since the domain of integration is not the full z-domain $-L_z/2$ to $L_z/2$, periodicity does not apply and therefore Fourier transforms cannot be used to evaluate the derivatives. Instead, we calculate the derivative $\partial_z \left(\frac{A^2 \tilde{\beta}^2 \tilde{\lambda}^{1/3}}{\tilde{k}^4} \right)$ using a finite-difference method, while the quadrature is performed using Matlab's trapz function. Once $\overline{\Omega}_c$ is computed, the true spanwise wavenumber, true fissure thickness, and true Reynolds number can be found via

$$\breve{\alpha} = \tilde{\alpha} \overline{\Omega}_c^{1/4}, \quad (3.26)$$

$$\Delta = \tilde{\Delta} \overline{\Omega}_c^{1/4}, \quad (3.27)$$

$$Re^{-1} = \tilde{\Delta}^4 \overline{\Omega}_c. \quad (3.28)$$

With these computations, the ECS flow fields can be reconstructed. These reconstructions, along with a parametric study detailing how key outputs (i.e. the roll circulation) vary with changes to the input parameters are presented in the next chapter.

3.6 Summary

In this chapter, the numerical methods used to solve the reduced governing equations derived in chapter 2 are summarized. First, the x-mean streamwise velocity is computed in the UMZ and VFs by marching (3.5) to steady state, where $\overline{u}_0 = y + \overline{u}$ and the roll motions are self-consistently prescribed according to (3.3)–(3.4). A Fourier pseudospectral method is used to treat the spanwise dependencies while a Chebyshev collocation scheme is used to discretize the fissure-

normal (y) direction. A semi-implicit Crank-Nicolson/Adams-Bashforth time-stepping scheme is used to advance (3.5) to a steady-state solution.

Next, the resulting viscously-regularized numerical solution for the streak shear at the VF centerline $\partial_y \overline{u}_0(0,z)$ computed for finite Re is compared at $y = 0$ with the corresponding profile obtained from the Childress cell problem for infinite Re obtained by Chini & Cox (2009). This validation enables the mean streamwise velocity from the finite-Re computation to be used in the numerical solution of the Rayleigh equation for the fluctuation fields in the VF, with the values for the mean streamwise velocity obtained by interpolating onto a grid within the VF domain. The Rayleigh equation (3.12) is then solved at a discrete set of z-locations within the VF to obtain the (positive real) eigenvalue $\tilde{k}^2$ and corresponding eigenfunction ϕ. The eigenvalue $\tilde{k}^2(z)$ is used to determine the slowly z-varying spanwise wavenumber $\tilde{\beta}(z)$ through the Eikonal equation, while the eigenfunction ϕ directly yields the rotated streamwise fluctuating velocity component $\hat{\mathcal{U}}_{3r}$ and the fissure-normal fluctuating velocity component $\hat{\mathcal{V}}_3$ according to $\tilde{k}\hat{\mathcal{U}}_{3r} = \partial_{\mathcal{Y}}\phi$ and $\hat{\mathcal{V}}_3 = -i\phi$. These results are then used to evaluate the coefficients a_z and a_0 arising in the fluctuation amplitude equation and, thence,

$$A = \exp\left(-\int_0^z \frac{a_4}{a_3} dz\right). \tag{3.29}$$

In the original (non-rotated) coordinate system, the fluctuation velocity components within the VF centered on $\mathcal{Y} = 0$ are given by

$$\mathcal{U}_3' = 4\sqrt{2}\mathcal{A}A\hat{\mathcal{U}}_3^+ \sin(\theta)\cos(\alpha x), \tag{3.30}$$

$$\mathcal{V}_3' = 4\sqrt{2}i\mathcal{A}A\hat{\mathcal{V}}_3^+ \sin(\alpha x)\sin(\theta), \tag{3.31}$$

$$\mathcal{W}_3' = -4\sqrt{2}\mathcal{A}A\hat{\mathcal{W}}_3^+ \cos(\theta)\sin(\alpha x), \tag{3.32}$$

where the '+' superscript indicates $\tilde{\beta} > 0$.

Finally, recalling that contribution to the integral determining the x-mean vorticity $\overline{\Omega}_c$ arising from the caustics is asymptotically small, the quadrature for the core vorticity $\overline{\Omega}_c$ reduces to

$$\overline{\Omega}_c^{7/3} = \frac{32\mathcal{A}^2 n_0 \tilde{\alpha}^{1/3}}{\pi^2} \int_0^{z_c^-} \left(\partial_z \left(\frac{A^2 \tilde{\beta}^2 \tilde{\lambda}^{1/3}}{\tilde{k}^4} \right) \sum_{n=0}^{n=\infty} \left[\frac{1}{n^2} \tanh\left(\frac{n\pi}{L_z} \right) \sin\left(\frac{2n\pi z}{L_z} \right) \right] \right) dz. \quad (3.33)$$

where z_c^- is the location of the caustic in $z > 0$. With the core vorticity known, the values for the true spanwise wavenumber, true fissure thickness, and true Reynolds number can be computed.

CHAPTER 4

RESULTS

4.1 Introduction

In the previous chapters a detailed asymptotic analysis of the incompressible NS equations revealed a new self-sustaining process in (initially) non-inflectional uni-directional shear flows that provides a mechanistic explanation for the sustenance of UMZs and VFs in high-Reynolds number wall turbulence. Having reviewed the numerical methods used to solve the asymptotically reduced equations derived in chapter 2, in this chapter, ECS supported by the new SSP are reconstructed and analyzed. The ECS we construct are spatially distributed in that the rolls and streaks are stacked in the y direction, being embedded in unbounded plane Couette flow. Because the Rayleigh instability modes are strictly localized within the spatially-segregated fissures (owing to the scale separation between the wavy instabilities and the roll/streak flow), the required stacking is simpler than that performed in Hall (2018). In the latter investigation, a countable infinity of viscous VWI states (each related to the lower-branch equilibrium solution EQ7) is shown to be an asymptotic solution in unbounded plane Couette flow provided the x-varying fluctuation pressure satisfies a certain *global* elliptic equation. In contrast, the fluctuation pressure field associated with the spatially-distributed inertial ECS constructed here decays exponentially away from the center of each VF. The only subtlety is that although roll and streak flow in each layer is steady, the Rayleigh instability mode is stationary only for the VF at $y = 0$. More generally, the instability mode localized within the VF at $y = n$, for integer n, propagates with a phase speed $c_n = n$, i.e. the average of the homogenized streamwise speeds of the adjacent upper and lower UMZs (*viz.* $[(n + 1/2) + (n - 1/2)]/2$). Nevertheless, the homogenized vorticity $\bar{\Omega}_c$ within each UMZ has the same value, implying the rolls have the same circulation strength independently of their y location.

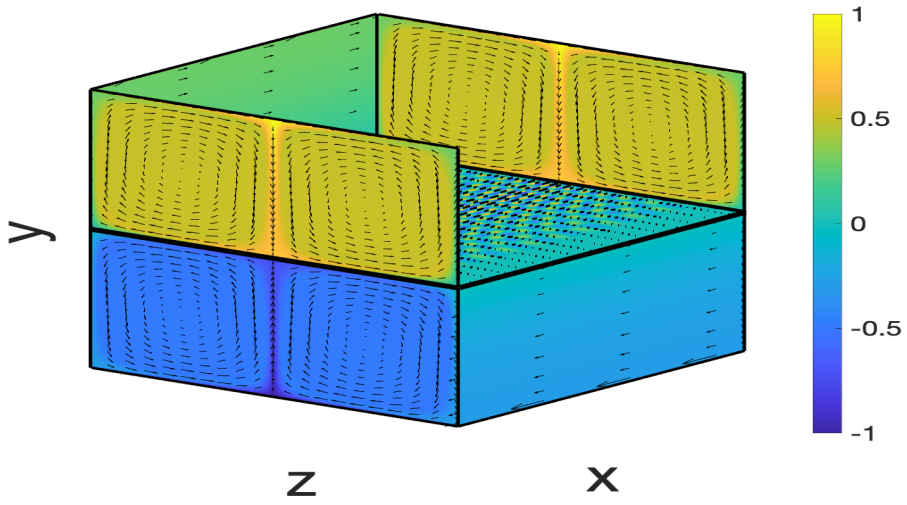

Figure 4.1: 3D numerical reconstruction of inertial layer ECS supporting VFs coupled to adjacent UMZs. Input parameters are $\mathcal{A} = 5$, $\breve{\alpha} = 0.576$ and $L_z = 2$. ($Re = 1.36 \times 10^7$ for computation of the streak velocity field.) Color indicates the streamwise-averaged streamwise flow speed in the y–z and x–y planes and the fissure-normal fluctuation velocity, scaled by $O(\Delta^3)$, in the exposed x–z plane. Arrows show in-plane velocity vectors.

This deduction, however, applies only to unbounded plane Couette flow and does not hold for base flow profiles that vary nonlinearly with y. Our ECS solution algorithm is summarized in appendix F.

4.2 Numerical Reconstruction of ECS

Figure 4.1 shows a 'unit ECS' excised from the flow domain centered on the VF at $y = 0$. Color indicates the streamwise-averaged streamwise flow speed in the y–z and x–y planes, as well as the $O(\Delta^3)$ fissure-normal fluctuation velocity in the exposed x–z plane. The parameters used to generate this ECS are $\mathcal{A} = 5$, $\tilde{\alpha} = 0.35$, and $L_z = 2$. With these inputs, the x-mean vorticity $\bar{\Omega}_c = 7.35$ is self-consistently computed. The true streamwise wavenumber, i.e. the dimensional streamwise wavenumber divided by $Re^{1/4} l_y^{-1}$ independently of $\bar{\Omega}_c$, is found to be $\breve{\alpha} = 0.5763$. For ease of interpretation, subsequent visualizations are presented in three orthogonal planes: the y–z plane at $x = 0$, an x–z plane in the VF and on x–y plane restricted in $\mathcal{Y}$ to show a close-up view near the center of the VF.

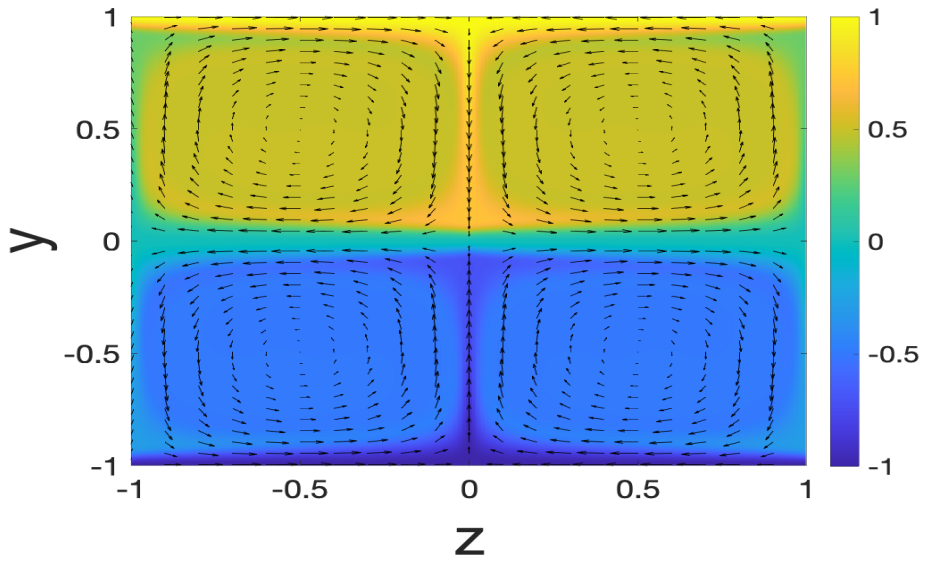

Figure 4.2: Reconstruction of inertial ECS exhibiting VFs coupled to adjacent UMZs in unbounded plane Couette flow: Mean velocity field in the fissure-normal/spanwise-plane. Color indicates the value of the streamwise-averaged streamwise velocity component while arrows show the roll velocity field. Parameter values are given in the figure 4.1 caption.

4.2.1 Uniform Momentum Zones

Figure 4.2 shows a plane perpendicular to the streamwise flow. Only mean velocities are plotted because the fluctuation fields are exponentially small except within the asymptotically thin VF. The colors indicate the values of the mean streamwise velocity component, while the arrows show the in-plane roll velocity field with the size of the arrows indicating the flow velocities relative to an arbitrary maximum value. This construction enables the rolls to be visualized but it should be recalled that, asymptotically, the roll flow is weak relative to the streamwise velocity component. The steady solution clearly exhibits the homogenization driven by the rolls as well as the spontaneous emergence of thin fissures at $y = 0$. Additional shear layers located above at $y = 1$ and below at $y = -1$ also are apparent. As expected from symmetry considerations, the streak speed within the upper UMZ is homogenized to a value $\overline{u}_0 = 1/2$ while the lower UMZ has $\overline{u}_0 = -1/2$. For the upper UMZ, fluid having relatively high (low) streamwise momentum is carried downward (upward) in narrow jets centered on $z = 0$ ($z = \pm 1$).

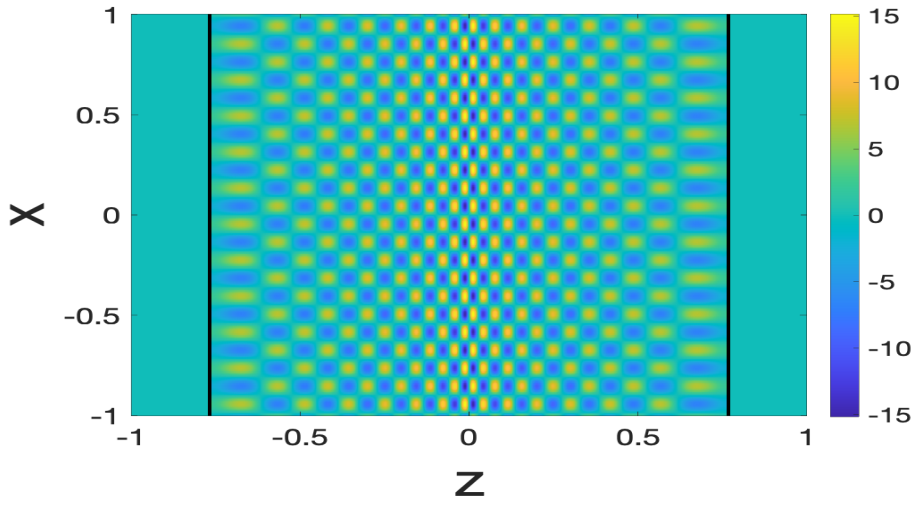

Figure 4.3: Reconstruction of inertial ECS exhibiting VFs coupled to adjacent UMZs in unbounded plane Couette flow: Fissure-normal fluctuation velocity component in a streamwise/spanwise plane within the VF near $y = 0$. Color indicates the value of this component normalized by Δ^3. The solid black lines indicate caustics, which partition the plane into an illuminated region ($-0.75 \lesssim z \lesssim 0.75$) and shadow zones ($|z| \gtrsim 0.75$). Parameter values are given in the figure 4.1 caption.

4.2.2 Vortical Fissures

Figure 4.3 shows the fissure-normal fluctuation velocity component $\mathcal{V}_3'$ in a streamwise/spanwise plane located within the VF close to the CL (i.e. close to $\mathcal{Y} = 0$). Color is used to represent flow speeds with yellow corresponding to positive and blue to negative values. This visualization reveals two important features of the inertial ECS supported by the SSP investigated here. Firstly, caustics partition the spanwise domain within the VF into an illuminated region, within which the fluctuations are confined, and shadow zones, where the instability mode is exponentially small. Note that only the fluctuations are plotted in figure 4.3; the mean fields do not vanish in the shadow regions, so the fluid is in motion there. The shadow zones are observed to align with the upwelling (downwelling) regions in the mean flow for $y > 0$ ($y < 0$), suggesting that the caustics arise from divergent straining of the shear layer to the extent that the shear within the VF is too diffuse to support the Rayleigh instability mode. A second feature that is clearly evident is the slow z modulation of the Rayleigh mode spanwise wavenumber and amplitude; indeed, the lines of constant

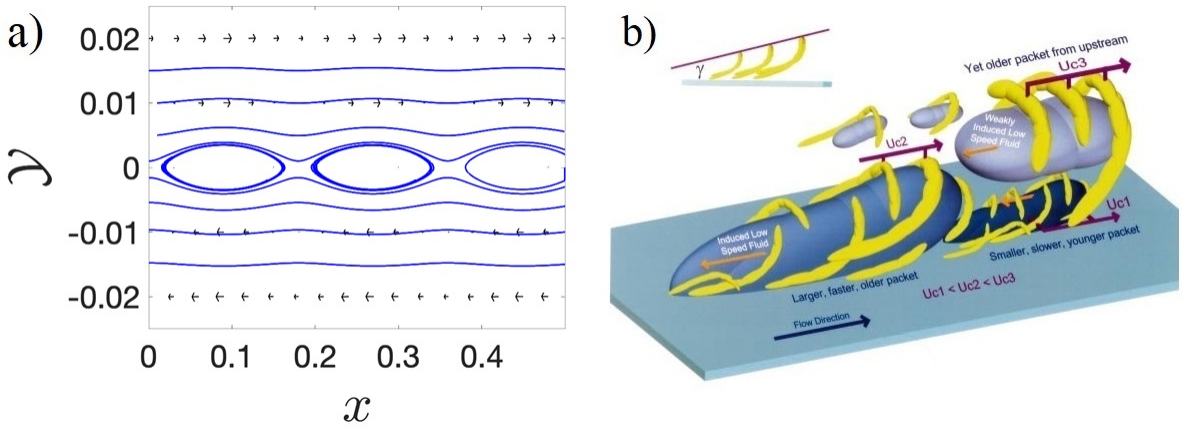

Figure 4.4: (a) Streamlines within the VF associated with an inertial-ECS solution computed for $\mathcal{A} = 5$, $\breve{\alpha} = 0.576$ and $L_z = 2$ (with $Re = 1.36\text{x}10^7$) showing a fine-scale Kelvin's cat's-eyes vortex pattern in the streamwise/wall-normal plane $z = -0.6738$ on which the spanwise fluctuation velocity vanishes. (b) Schematic taken from Adrian *et al.* (2000) showing fine-scale hairpin and 'cane' vortices (in yellow) separating boluses of large-scale streamwise flow having quasi-uniform momentum (in grey).

instability-wave phase appear to bend in this plane, forming cusps at the caustics. This patterning highlights the horizontal scale separation between the instability mode and the roll/streak flow.

Figure 4.4 (a) shows a close-up view of streamlines in a streamwise/fissure-normal plane within the VF centered on $y = 0$. In a co-moving reference frame, the streamlines within each fissure adopt a characteristic Kelvin's cat's-eyes vortex pattern. This patterning is commonly observed in the neighborhood of critical layers when streamlines are plotted in a reference frame traveling with the marginally stable disturbance mode (Drazin, 2002). Intriguingly, this streamline pattern seems to accord qualitatively with the conceptual model of Adrian *et al.* (2000), who proposed that regions of high shear separating the UMZs comprise the heads of hairpin and/or 'cane' vortices, as shown schematically in figure 4.4(b).

4.3 Parameter Study

We next analyze the impact of varying the key control parameters $\mathcal{A}$, $\breve{\alpha}$ and L_z on the ECS. For this purpose, a convenient metric is the homogenized value of the x-mean x-vorticity $\bar{\Omega}_c$ within the UMZs. Equation (2.137) gives $\bar{\Omega}_c$ as a function of L_z, $\tilde{\alpha}$ and $\mathcal{A}$. To recover the dependence

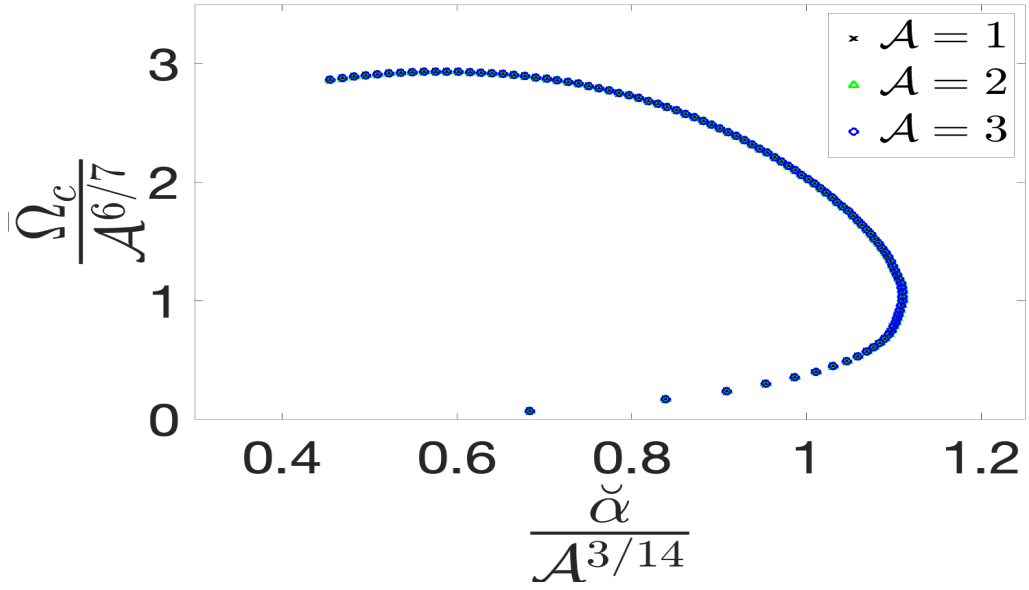

Figure 4.5: The homogenized value of the roll vorticty $\overline{\Omega}_c$ normalized by $\mathcal{A}^{6/7}$ versus the true streamwise wavenumber normalized by $\mathcal{A}^{3/14}$ for $L_z = 2$. The different curves correspond to different values of $\mathcal{A}$.

of $\bar{\Omega}_c$ on the true streamwise wavenumber $\breve{\alpha}$, the substitution $\breve{\alpha} = \left[\bar{\Omega}_c(\tilde{\alpha})\right]^{1/4} \tilde{\alpha}$ is made. In addition, for a given roll-cell wavelength L_z, the dependence of $\bar{\Omega}_c$ on $\mathcal{A}$ can be removed by scaling $\bar{\Omega}_c \to \mathcal{A}^{6/7}\bar{\Omega}_c$, provided that the true streamwise wavenumber is also rescaled according to $\breve{\alpha} \to \mathcal{A}^{3/14}\breve{\alpha}$. Figure 4.5 shows that plots of $\bar{\Omega}_c$ versus $\breve{\alpha}$ for fixed L_z but varying $\mathcal{A}$ then will collapse onto a single curve. Physically, the roll circulation achieved for a given L_z, $\mathcal{A}$ and $\breve{\alpha}$ also can be realized by appropriately modifying both $\mathcal{A}$ and $\breve{\alpha}$.

Figure 4.6 shows the x-mean vorticity as a function of the roll-cell width. Figure 4.6a shows curves of constant input parameter $\tilde{\alpha}$ while the plot on the right shows curves of constant $\breve{\alpha}$. $\overline{\Omega}_c$ monotonically decreasing with L_z for the smaller values of $\tilde{\alpha}$. For larger $\tilde{\alpha}$, there is a local maximum indicating a specific $\tilde{\alpha}$ will result in the greatest circulation within the UMZ for a given cell width. Figure 4.6b shows the x-mean vorticity versus L_z for specific values of the true streamwise wavenumber $\breve{\alpha}$. Interestingly, when $\bar{\Omega}_c$ is plotted versus L_z for fixed $\breve{\alpha}$, a saddle-node bifurcation with upper- and lower-branch solutions is revealed. The upper branch is characterized by stronger

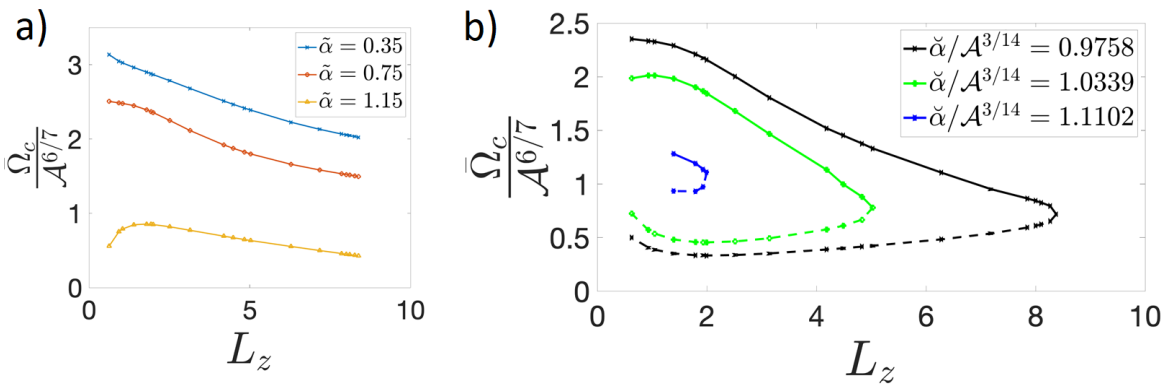

Figure 4.6: The homogenized value of the roll vorticty $\overline{\Omega}_c$ normalized by $\mathcal{A}^{6/7}$ versus the roll wavelength L_z. In (a), the different curves correspond to different constant values of the input wavenumber $\tilde{\alpha}$, while in (b), the various curves indicate different constant values of the 'true' streamwise wavenumber $\breve{\alpha}$.

roll-cell circulation arising at smaller $\breve{\alpha}$ (i.e. for streamwise-varying instability modes with longer wavelengths), while the lower branch exhibits the opposite trend.

Figure 4.7 shows the x-mean vorticity as a function of streamwise wavenumber. The figure on the left shows $\overline{\Omega}_c$ versus the rescaled input wavenumber $\tilde{\alpha}$ for given constant values of the input parameter L_z, while the plot on the right uses the *a posteriori* calculated value of $\breve{\alpha}$, again for curves of constant L_z. Figure 4.7a reveals two interesting features. One is the existence of a global maximum for each curve of constant L_z. Thus, there is a specific $\tilde{\alpha}$ that will result in a maximum circulation in the UMZ for a given roll-cell width L_z. A second feature is the tendency for a larger $\overline{\Omega}_c$ to be associated with smaller L_z, as first observed in figure 4.6. However, for sufficiently large $\tilde{\alpha}$, there is a region in which this trend is not realized. This exception can be understood as a consequence of different cell widths being associated with different maximum values of $\tilde{k}(z)$. Recalling the Eikonal equation,

$$\tilde{\alpha}^2 + \tilde{\beta}^2 = \tilde{k}^2, \tag{4.1}$$

cells with larger maximum $\tilde{k}$ values can support larger values of input $\tilde{\alpha}$.

Figure 4.7b shows the x-mean vorticity as a function of true streamwise wavenumber $\breve{\alpha}$ for a range of given, constant roll-cell widths L_z. In this figure, too, turning points are evident, and

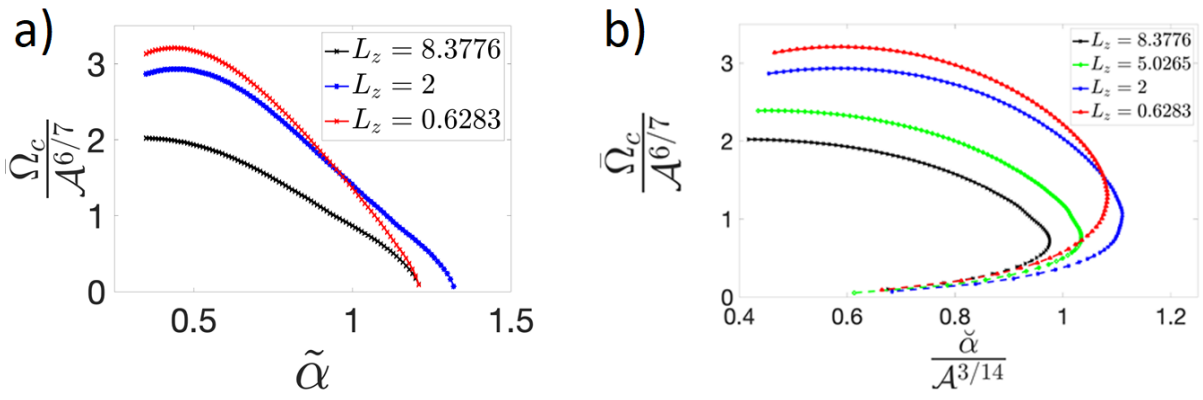

Figure 4.7: The homogenized value of the roll vorticty $\overline{\Omega}_c$ normalized by $\mathcal{A}^{6/7}$ (a) plotted versus the input wavenumber $\tilde{\alpha}$, where the different curves correspond to different constant values of the roll wavelength L_z, and (b) plotted versus the 'true' streamwise wavenumber $\breve{\alpha}$ normalized by $\mathcal{A}^{3/14}$, where the different curves again correspond to different constant values of the roll wavelength L_z.

the solution bifurcates into upper and lower branches. For the upper-branch solutions, it can be seen that $\bar{\Omega}_c$ increases monotonically as the roll-cell size is decreased. In contrast, the roll vorticity associated with the lower-branch states does not vary monotonically with L_z. Moreover, the bifurcation curve for each fixed L_z possesses a maximum along the upper branch, implying that for a given L_z there exists a specific streamwise wavenumber at which the roll-cell circulation is maximized. The primary qualitative distinction between the upper- and lower-branch solutions is that the illuminated regions associated with the upper-branch states are larger than those associated with the corresponding lower-branch ECS.

4.4 Upper and Lower Branch States

In this section, the emergence of upper- and lower-branch ECS is analyzed in greater detail. The saddle-node bifurcations evident in figure 4.6b and figure 4.7b, but not in figure 4.6a and figure 4.7a can be traced to relationship between the two $O(1)$ streamwise wavenumbers $\tilde{\alpha}$ and $\breve{\alpha}$; namely $\breve{\alpha} = \tilde{\alpha}\overline{\Omega}_c^{1/4}$. Crucially, this relationship is nonlinear because $\overline{\Omega}_c$ itself a function of $\tilde{\alpha}$. Figure 4.8 confirms that $\tilde{\alpha}$ is *not* a single-valued function of $\breve{\alpha}$.

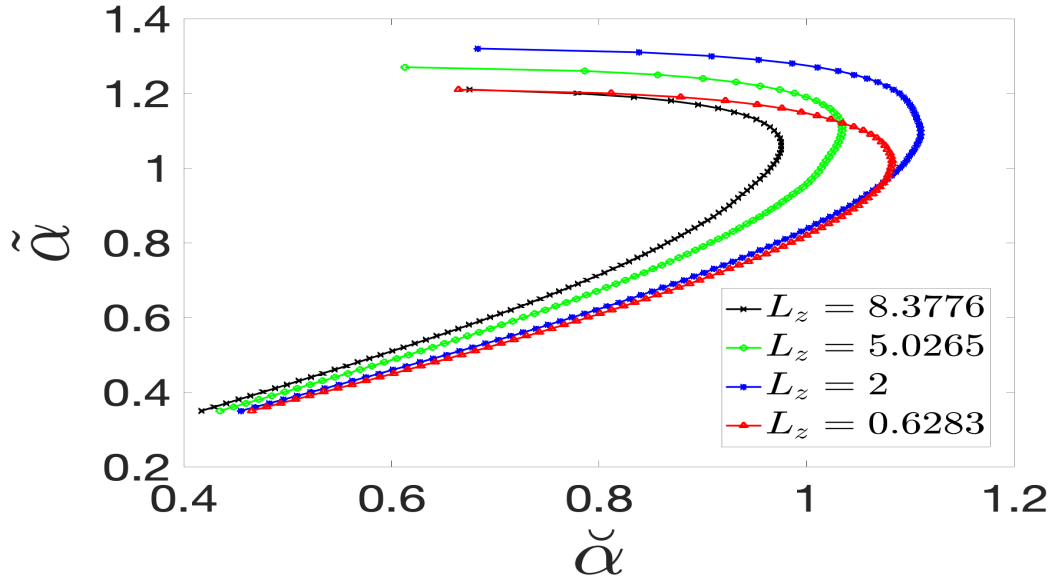

Figure 4.8: The input streamwise wavenumber $\tilde{\alpha}$ plotted versus the 'true' streamwise wavenumber $\breve{\alpha}$ to demonstrate the nonlinear relationship between them that yields upper and lower branch inertial ECS. The different curves correspond to different values of the roll wavelength.

As evident in figure 4.7, when $\bar{\Omega}_c$ is plotted versus the true streamwise wavenumber $\breve{\alpha}$, a saddle-node bifurcation with upper- and lower-branch solutions is revealed; in contrast, as a function of $\tilde{\alpha}$, $\bar{\Omega}_c$ is not multi-valued and decreases monotonically to zero as $\tilde{\alpha}$ is increased beyond a threshold value. This latter trend may be understood by recalling the Eikonal equation $\tilde{\alpha}^2 + \tilde{\beta}^2(z) = \tilde{k}^2(z)$. For a given L_z, the z-varying profile of the eigenvalue $\tilde{k}^2$ qualitatively resembles that of the streak shear $\tilde{\lambda}(z)$, which itself is *independent* of $\tilde{\alpha}$, shown in figure 3.2: the total horizontal wavenumber of the neutral Rayleigh mode is larger where the shear is locally larger and the fissure is locally thinner (and conversely). As $\tilde{\alpha}$ is increased, the Eikonal equation therefore requires the width of the illuminated region to decrease. Consequently, both the magnitude of the z-integrated forcing from the Rayleigh mode and the resulting value of $\bar{\Omega}_c$ also must decrease. The caveat is that, as the turning point is approached from the upper branch, the ECS solutions become non-uniformly asymptotic; that is, for the lower-branch states, ever larger values of Re are required to ensure that the width of the illuminated region remains asymptotically larger than the widths of the caustics

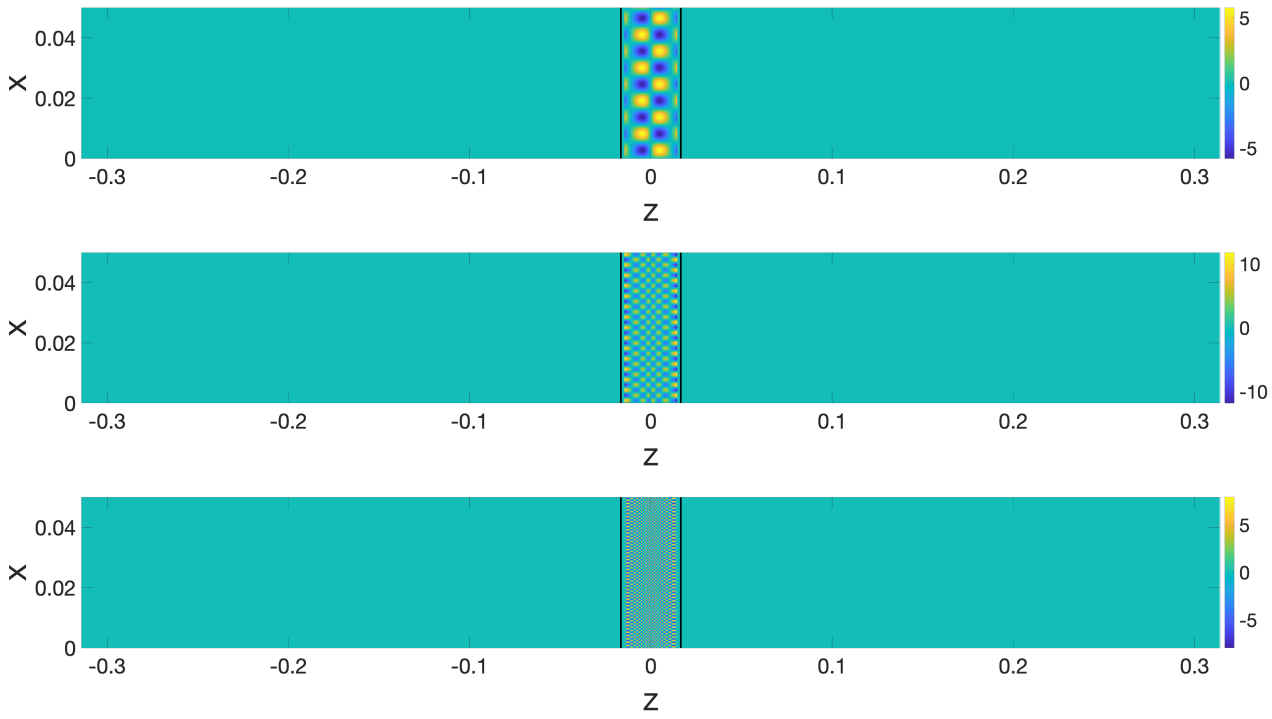

Figure 4.9: Fissure-normal fluctuation velocity in an x–z plane near the CL for a lower-branch ECS computed at $\mathcal{A} = 1$, $L_z = \pi/5$, and $\tilde{\alpha} = 1.02$. Colors indicate velocities normalized by $\tilde{\Delta}^3$. $Re = 10^{11}$: top; $Re = 10^{13}$: middle; $Re = 10^{15}$: bottom.

and the streamwise jets. For this reason, a dashed line is used to designate the lower-branch states in figure 4.6b and figure 4.7b.

Although the widths of the illuminated and shadow regions are determined by the input $\tilde{\alpha}$ independently of Re, reconstructions of the fluctuating velocities are dependent on Re. Figure 4.9 shows the fissure-normal fluctuation velocity in a streamwise/spanwise plane within the VF for $Re = (10^{11}, 10^{13}, 10^{15})$ for the turning point of the ECS. Clearly, $A(z)$ is exponentially small over the majority of the z-domain, as the shadow zones occupy most of the x–z plane shown. Physically, the driving of these rolls from the vorticity jump across the CL is restricted to a very narrow portion of the spanwise flow domain. Furthermore, the validity of the WKBJ ansatz is dependent upon spatial scale separation in the spanwise direction. This scale separation becomes ever more difficult to realize as the illuminated regions associated with the lower-branch ECS

become narrower as $\tilde{\alpha}$ is increased. Accordingly, extreme values of Re are required to achieve scale separation, as evident in figure 4.9.

4.5 Summary

The ECS supported by the inertial-layer SSP exhibit the characteristic attributes outlined in the dissertation objectives. In particular, the numerically-reconstructed ECS clearly show the homogenization of the streamwise velocity and the creation of internal shear layers. Additionally, the reconstructions exhibit other features anticipated from the analysis, including the slow modulation of the Rayleigh mode in the spanwise direction and the emergence of shadow regions. Unexpected features such as the cats-eye vortex pattern also are revealed, in evident agreement with a schematic representation of UMZs and VFs produced by Adrian *et al.* (2000).

The dependence of the newly-identified ECS on input parameters has been quantified by plotting the roll vorticity $\overline{\Omega}_c$ as functions of the Rayleigh-mode (true) streamwise wavenumber $\breve{\alpha}$ and the roll-pair spanwise wavelength L_z. The dependence of $\overline{\Omega}_c$ on the scalar amplitude $\mathcal{A}$ of the Rayleigh mode can be eliminated through a suitable rescaling of $\mathcal{A}$ and the streamwise wavenumber. These plots reveal saddle-node bifurcations and the emergence of upper and lower branch solutions, as is common for ECS in shear flows.

Inspection of the upper- and lower- branch solutions, reveals that the former are characterized by larger values of the roll circulation and wider illuminated regions than exhibited by the latter. In fact, the illuminated regions associated with the lower-branch ECS can be sufficiently narrow (depending on the precise value of the streamwise wavenumber) that extraordinarily large values of Re are required to achieve the scale separation in the spanwise direction necessary for the validity of the WKBJ approximation.

CHAPTER 5

CONCLUSIONS AND FUTURE WORK

In turbulent wall flows at large Reynolds number, the ensemble or long-time mean viscous force is sub-dominant outboard of the peak in the Reynolds stress and hence over the majority of the turbulent flow domain. Mounting evidence indicates that the instantaneous streamwise velocity in this inertial domain is characterized by regions of quasi-uniform momentum (UMZs) separated by spatially-segregated internal shear layers (i.e. vortical fissures). In this investigation, a first-principles self-sustaining process theory has been derived from the incompressible Navier–Stokes equations in the large Reynolds number limit that can account for key attributes of the resulting staircase-like profiles of streamwise velocity. Chief among these attributes is that the suitably normalized fissure thickness decreases as the friction Reynolds number $Re_\tau = u_\tau h/\nu$ increases; that the dimensional jump in flow speed across each VF scales with the friction velocity u_τ; and that the volume-mean viscous force is, in fact, sub-dominant in this dynamical process.

Figure 5.1 depicts the key components of the proposed inertial-layer SSP. As in vortex–wave interaction (VWI) theory, streamwise rolls induce $O(1)$ streamwise streaks through the lift-up mechanism. A crucial distinction, however, is that in the inertial domain the comparably weak rolls must nevertheless have a circulation strength that is asymptotically larger than $O(1/Re)$ to ensure that these large-scale roll and streak components of the turbulence are not (in a volume-averaged sense) dynamically influenced by viscous forces, unlike ECS solutions of the VWI equations. Indeed, in the present inertial-layer SSP theory, the roll strength is $O(Re^{-1/2})$. This sub-Re^{-1} decay is also a necessary condition for stacked arrays of counter-rotating roll vortices to differentially homogenize the background shear flow and thereby generate slender embedded internal layers of high vorticity. Each internal layer (VF) has a characteristic thickness that decreases with Re. In

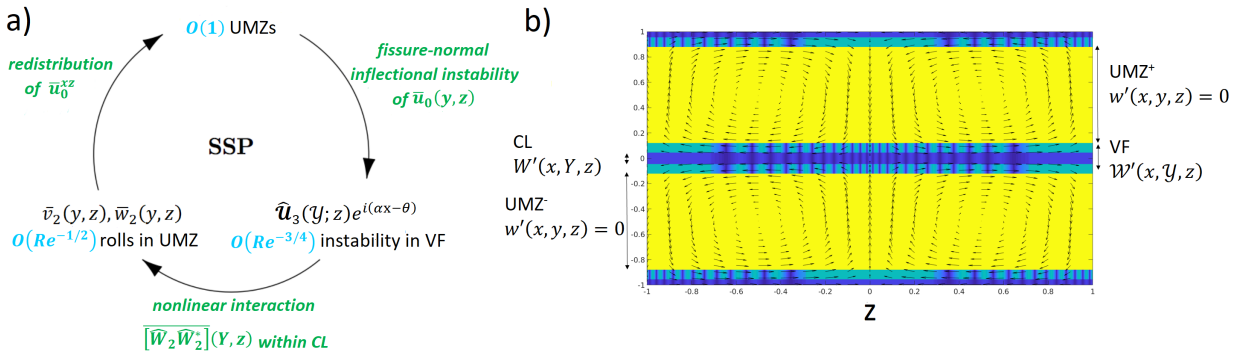

Figure 5.1: Schematic diagram of a mechanistic self-sustaining process for UMZs and VFs in the inertial domain of turbulent wall flows. The feedback loop shown in (a) indicates that rolls having $O(Re^{-1/2})$ circulation strength redistribute the background shear flow to induce $O(1)$ streamwise streaks. As depicted in (b), the counter-rotating and stacked rolls are sufficiently strong to differentially homogenize the background flow, thereby creating and maintaining both UMZs (highlighted in yellow) and internal shear layers (VFs, indicated in blue). The wall-normal (y) inflections in the streak velocity support an $O(Re^{-3/4})$ Rayleigh (inviscid shear) instability mode that has a streamwise (x) wavelength $2\pi/\alpha \ll 1$ that is commensurate with the VF thickness. Consequently, the Rayleigh mode is confined to the VF, where it is refracted and rendered three-dimensional by the comparably slow spanwise variation in the fissure thickness (not depicted), and the resulting ECS are inherently multiscale. The 3D Rayleigh mode suffers a critical-layer singularity, causing the magnitude of the x-varying spanwise velocity component to be amplified to $O(Re^{-1/2})$. The resulting nonlinear self-interaction of the Rayleigh mode within the CL drives the roll motions in the UMZs through a modulational (i.e. slow spanwise) Reynolds stress divergence involving this velocity component.

contrast, the lower- and upper-branch equilibrium solutions EQ7 and EQ8 in plane Couette flow, which share the same roll configuration as the ECS constructed here, remain viscously dominated even as $Re \to \infty$. Consequently, neither EQ7 nor EQ8 exhibits thinning internal shear layers or genuinely homogenized zones of streamwise momentum.

Apparent discontinuities in the inertial-ECS streak velocity and roll vorticity are smoothed by viscous forces and torques acting within the VFs and narrow streamwise jets demarcating the boundary of each roll cell. The inflectional streak shear within each fissure supports a neutral Rayleigh instability (or 'fluctuation') mode having an $O(Re^{-3/4})$ characteristic size and a streamwise wavelength that scales with the VF thickness. Thus, inertial ECS are inherently multiscale: the streamwise-varying fluctuation fields and the streamwise-mean roll/streak flow exhibit dis-

parate spatial scales, a feature that is accommodated in the theory via a WKBJ representation of the instability mode. Moreover, the fluctuation fields are exponentially localized within the fissures, since that is where the shear is confined. The Rayleigh mode, which might be expected to vary primarily in the streamwise and fissure-normal directions, is refracted in the spanwise direction and rendered 3D by the comparably slow spanwise variation in the thickness of each fissure. This three-dimensionality is essential because, at least in the present formulation, the fluctuation-induced Reynolds stresses associated with the inviscid marginal mode necessarily vanish within the VF; thus, the roll motions are not directly driven there.

Instead, a critical layer (CL) mechanism is operative. More specifically, although the (appropriately rotated) two-component, 2D marginal Rayleigh mode is a smooth function of the fissure-normal coordinate, the full three-component, 3D marginal mode exhibits a CL singularity at the center of each VF. As in VWI theory, the resulting amplification of the tangential fluctuation velocity components is regularized by viscous forces acting within the CL. (It is conceivable that nonlinear regularization also may be realizable, although that possibility is not pursued here.) The nonlinear self-interaction of the Rayleigh mode within the CL induces a jump in the x-mean spanwise shear or, equivalently, the x-mean streamwise vorticity across the CL via a *modulational* (i.e. slow spanwise) divergence of the spanwise Reynolds stress component. In turn, this shear drives a tangential mean flow within – and ultimately a roll flow outside of – the VF in which the CL is embedded. (Since this flow is transverse to the streamwise velocity and driven by spanwise stress gradients, it may be understood as a *Prandtl secondary flow of the second kind*.) In steady state, the work done by the fluctuation-induced mean viscous tangential stress at the edges of the CL is balanced by viscous dissipation of roll kinetic energy within the adjacent UMZs, thereby closing the inertial-domain SSP.

Visualizations of the inertial ECS clearly show the slow spanwise modulation of the Rayleigh-mode spanwise wavenumber as well as the emergence of caustics, which separate the VFs into illuminated and shadow regions. Within these zones, the fluctuations have finite and exponentially small amplitudes, respectively. The caustics arise because, at specific spanwise locations, the roll

flow strains the embedded VF to the extent that the streak shear is too diffuse to continue to support the marginal Rayleigh mode. As is common in shear flows, the ECS identified here exhibit saddle-node bifurcations, with the primary distinction between the upper- and lower-branch solutions being the magnitude of the roll-cell circulation and the width of the illuminated regions (both are larger for the upper-branch states).

In a co-moving reference frame, the streamlines within each fissure adopt a characteristic Kelvin's cat's-eyes vortex pattern. Intriguingly, this streamline pattern seems to accord qualitatively with the conceptual model of Adrian *et al.* (2000), who proposed that regions of high shear separating the UMZs comprise the heads of hairpin and/or 'cane' vortices, as shown schematically in figure 4.4b. Regardless of the relevance or not of hairpin vortices *per se*, flow visualizations by Adrian *et al.* (2000) and others reveal small-scale rotary motions, consistent with the structure of the ECS supported by the proposed SSP, as illustrated in figure 4.4a. Perhaps more significantly, the schematic shown in figure 4.4b suggests a disparity between the scale (diameter) of these rotary motions and the transverse scale of the boluses of fluid having uniform momentum, again in apparent qualitative agreement with the multiscale structure intrinsic to the proposed SSP. In particular, the rotary motions in the inertial ECS have a size that is commensurate with the $O(\Delta)$ thickness of the fissure and therefore much smaller than separation distance between adjacent VFs.

Of course, there are certain evident limitations on the potential applicability of the SSP theory developed here to turbulent wall flows. Firstly, the predicted VF thickness scales as $Re^{-1/4}$, while data from DNS and laboratory experiments indicate that the thickness of a 'representative' fissure scales in proportion to $Re_\tau^{-1/2}$. It seems conceivable, however, that the difference between the predicted and measured scalings may be at least partly attributable to the different definitions of the Reynolds numbers used. In particular, the length scale used in the definition of Re is the separation distance l_y between the VFs, while the length scale h used to define Re_τ is the boundary-layer height or channel half-height. Moreover, for turbulent wall flows (at a given Re_τ), l_y varies with the wall-normal coordinate, and the ratio of the characteristic separation distance $\langle l_y \rangle$ to h varies with Re_τ. In appendix A, it is shown that, by accounting for this variation in the context of

the self-similar layer hierarchy admitted by the mean momentum balance (e.g. Wei *et al.* (2005); Klewicki (2013*a*,*b*)), the associated characteristic dimensional VF thickness Δ_f normalized by h scales in proportion to $Re_\tau^{-7/16}$, i.e. in much closer agreement with empirical estimates of this ratio.

A second, related restriction is that the ECS constructed are asymptotic solutions of the Navier–Stokes equations only for the non-physically-realizable case of unbounded Couette flow. Nevertheless, the ultimate aim of the research initiated in this dissertation is to treat inertial ECS arising in flows (e.g. plane Poiseuille flow) having velocity profiles that vary nonlinearly with the wall-normal coordinate. Preliminary considerations indicate that for solutions to exist the VFs necessarily will be non-uniformly spaced, in accord with observations of turbulent wall flows. In addition, it would be desirable to develop a time-dependent reduced PDE model of turbulence in the inertial layer by leveraging the most robust features of the asymptotic SSP identified in this study (a general strategy advocated, e.g., by Chini (2016)); for example, by exploiting the confinement of the fluctuations to the fissures and the *quasilinear* mathematical structure of the asymptotically-simplified system. This extension would enable an even tighter link to be made with the 1D UMZ/VF turbulence model recently developed by Bautista *et al.* (2019), e.g. by allowing for 'wafting' of the fissures, while also placing the 1D model on a more secure theoretical footing. Finally, the asymptotic ECS computed here for a given set of parameters presumably could be used as a very good initial iterate in a Newton search for a finite (but large) Reynolds number realization of this ECS employing the full Navier–Stokes equations.

In summary, a primary merit of the new SSP identified here is that it highlights the distinction between viscous and inertial ECS. The SSP also provides a plausible mechanism, derived directly from the NS equations, for the observed UMZ/VF profiles of streamwise velocity. In this mechanism, the VFs play a dynamically *active* role in the sustenance and persistence of the UMZs. Perhaps most significantly, the new SSP and associated ECS provide a concrete dynamical realization of the conceptual model of the singular nature of turbulent wall flows proposed by Klewicki

(2013*a*,*b*), lending further support to the 'boundary-layers-within-*the*-turbulent-boundary-layer' paradigm.

BIBLIOGRAPHY

ADRIAN, RJ., MEINHART, CD. & TOMKINS, CD. 2000 Vortex organization in the outer region of the turbulent boundary layer. *J. Fluid Mech.* **422**, 1–54.

AUBRY, N., HOLMES, P., LUMLEY, JL. & STONE, E. 1988 The dynamics of coherent structures in the wall region of a turbulent boundary layer. *J. Fluid Mech.* **192**, 115–173.

BALMFORTH, NJ., DEL-CASTILLO-NEGRETE, D. & YOUNG, WR. 1997 Dynamics of vorticity defects in shear. *J. Fluid Mech.* **333**, 197–230.

BATCHELOR, GK. 1956 On steady laminar flow with closed streamlines at large Reynolds number. *J. Fluid Mech.* **1**, 177–190.

BAUTISTA, JC. CUEVAS, EBADI, A., WHITE, CM. & CHINI, GP. 2019 A uniform momentum zone-vortical fissure model of the turbulent boundary layer. *J. Fluid Mech.* **858**, 609–633.

BEAUME, C., CHINI, GP., JULIEN, K. & KNOBLOCH, E. 2015 Reduced description of exact coherent states in parallel shear flows. *Phys. Rev. E* **91**, 43010.

BLACKBURN, HM, HALL, P. & SHERWIN, SJ. 2013 Lower branch equilibria in Couette flow: the emergence of canonical states for arbitrary shear flows. *J. Fluid Mech.* **762R2**, 1–12.

CHINI, GP. 2008 Strongly nonlinear langmuir circulation and Rayleigh-Bénard convection. *J. Fluid Mech.* **614**, 39–65.

CHINI, GP. 2016 Exact coherent structures at extreme Reynolds number. *J. Fluid Mech.* **794**, 1–4.

CHINI, GREG & COX, SM. 2009 Large Rayleigh number thermal convection: Heat flux predictions and strongly nonlinear solutions. *Physics of Fluids.* **21**, 083603.

CHINI, GP., MONTEMURO, B., WHITE, CM. & KLEWICKI, JC. 2017 A self-sustaining process model of inertial layer dynamics in high Reynolds number turbulent wall flows. *Phil. Trans. Roy. Soc. A* **375**, 20160090.

DAVIDSON 2004 *Turbulence: An introduction for scientist and engineers*. Oxford University Press.

DRAZIN 2002 *Introduction to Hydrodynamic Stability*. Cambridge Texts in Applied Mathematics.

DUGUET, Y., WILLIS, AP. & KERSWELL, RR. 2008 Transition in pipe flow: the saddle structure on the boundary of turbulence. *J. Fluid Mech* **613**, 255–274.

DUGUET, Y., WILLIS, AP. & KERSWELL, RR. 2010 Slug genesis in cylindrical pipe flow. *J. Fluid Mech* **663**, 180–208.

ECKHARDT, B. & ZAMMERT, S. 2018 Small scale exact coherent structures at large Reynolds numbers in plane Couette flow. *Nonlinearity.* **31**, R66.

EISMA, J., WESTERWEEL, J., OOMS, G. & ELSINGA, G. 2015 Interfaces and internal layers in a turbulent boundary layer. *Phys. Fluids* **27**, 055103.

ELSNAB, JR., MONTY, JP., WHITE, CM., KOOCHESFAHANI, MM. & KLEWICKI, JC. 2017 Efficacy of single-component mtv to measure turbulent wall-flow velocity derivative profiles at high resolution. *Exp. Fluids* **58**, 128–139.

FAIST, H. & ECKHARDT, B. 2003 Traveling waves in pipe flow. *Phys. Rev. Lett.* **91**, 224502.

FARRELL, BF. & IOANNOU, PJ. 2012 Dynamics of streamwise rolls and streaks in wall-bounded shear flow. *J. Fluid Mech.* **708**, 149–196.

GAD-EL-HAK, MOHAMED 1998 Fluid mechanics from the beginning to the third millennium. *International Journal of Engineering Education* **14(3)**, 177–185.

GIBSON, JF., HALCROW, J. & CVITANOVIĆ, P. 2008 Visualizing the geometry of state space in plane Couette flow. *J. Fluid Mech.* **611**, 107–130.

GIBSON, J. F. 2014 Channelflow: A spectral Navier-Stokes simulator in C++. *Tech. Rep.*. U. New Hampshire, `Channelflow.org`.

HALL, P. 2018 Vortex-wave interaction arrays: a sustaining mechanism for the log layer? *J. Fluid Mech.* **850**, 46–82.

HALL, P. & SHERWIN, S. 2010 Streamwise vortices in shear flows: harbingers of transition and the skeleton of coherent structures. *J. Fluid Mech.* **661**, 178–205.

HALL, P. & SMITH, F. 1991 On strongly nonlinear vortex/wave interaction in boundary layer transition. *J. Fluid Mech.* **227**, 641–666.

HAMILTON, JM., KIM, J. & WALEFFE, F. 1995 Regeneration mechanisms of near-wall turbulence structures. *J. Fluid Mech.* **287**, 317–348.

HARPER, J. F. 1963 On boundary layers in two-dimensional flows with vorticity. *J. Fluid Mech.* **17(1)**, 141–153.

HASSAN, H. & MEZIĆ, I. 2019 Prandtl-Batchelor theorem for flows with quasiperiodic time dependence. *J. Fluid Mech.* **862**, R1.

HUTCHINS, N. & MARUSIC, I. 2007 Evidence of very long meandering features in the logarithmic region of turbulent boundary layers. *J. Fluid Mech.* **579**, 1–28.

HWANG, Y. & BENGANA, Y. 2016 Self-sustaining process of minimal attached eddies in turbulent channel flow. *J. Fluid Mech.* **795**, 703–738.

HWANG, Y. & COSSU, C. 2010 Self-sustained process at large scales in turbulent channel flow. *Phys. Rev. Letter* **105**, 044505.

HWANG, Y., WILLIS, AP. & COSSU, C. 2016 Invariant solutions of minimal large-scale structures in turbulent channel flow for Re_τ up to 1000. *J. Fluid Mech.* **802R1**, 1–13.

JIMÉNEZ, J. & MOIN, P. 1991 The minimal flow unit in near-wall turbulence. *J. Fluid Mech.* **225**, 213–240.

JIMÉNEZ, J. & ZUFIRIA, JA. 1987 A boundary-layer analysis of Rayleigh-Bénard convection at large Rayleigh number. *J. Fluid Mech.* **178**, 53–71.

KLEWICKI, JC. 2013*a* A description of turbulent wall-flow vorticity consistent with mean dynamics. *J. Fluid Mech.* **737**, 176–204.

KLEWICKI, J. 2013*b* On the singular nature of turbulent boundary layers. *Proc IUTAM* **9**, 69–78.

KLINE, SJ., REYNOLDS, WC., SCHRAUB, FA. & RUNDSTADLER, PW. 1967 The structure of turbulent boundary layers. *J. Fluid Mech.* **30**, 741–773.

LUDWIG, D. 1966 Uniform asymptotic expansions at a caustic. *Communications on Pure and Applied Mathematics.* **19**, 215–250.

MCKEE, WD. 1973 Waves on a shearing current: a uniformly valid asymptotic solution. *Proc. Camb. Phil. Soc.* **75**, 295–301.

MEINHART, CD. & ADRIAN, RJ. 1995 On the existence of uniform momentum zones in a turbulent boundary layer. *Phys. Fluids* **7**, 694.

NAGATA, M. 1990 Three-dimensional finite-amplitude solutions in plane Couette flow: bifurcation from infinity. *J. Fluid Mech.* **217**, 519–527.

PIROZZOLI, S. & BERNARDINI, M. 2012 Probing high-Reynolds-number effects in numerical boundary layers. *Phys. Fluids* **25**, 021704.

PRIYADARSHANA, PJA., KLEWICKI, J., TREAT, S. & FOSS, JF. 2007 Statistical structure of turbulent boundary layer velocity-vorticity products at high and low Reynolds numbers. *J. Fluid Mech.* **570**, 307–346.

RHINES, PB. & YOUNG, WR. 1983 How rapidly is a passive scalar mixed within closed streamlines. *J. Fluid Mech.* **133**, 133–145.

SCHOPPA, W. & HUSSAIN, F. 2002 Coherent structure generation in near-wall turbulence. *J. Fluid Mech.* **453**, 57–108.

DE SILVA, CM., HUTCHINS, N. & MARUSIC, I. 2016 Uniform momentum zones in turbulent boundary layers. *J. Fluid Mech.* **786**, 309–331.

DE SILVA, C. M., PHILIP, J., HUTCHINS, N. & MARUSIC, I. 2017 Interfaces of uniform momentum zones in turbulent boundary layers. *J. Fluid Mech.* **820**, 451–478.

SREENIVASAN, KR. 1999 Fluid turbulence. *Rev. Mod. Phys.* **71**, 383–395.

TREFETHEN 2000 *Spectral Methods in Matlab*. Springer.

WALEFFE, F. 1995 Hydrodynamic stability and turbulence: Beyond transients to a self-sustaining process. *Stud. Appl. Math* **95**, 319.

WALEFFE, FABIAN 1997 On a self-sustaining process in shear flows. *Phys. Fluids* **9**, 883–900.

WALEFFE, FABIAN 2005 Structures of shear turbulence. Woods Hole Oceangraphic Institution Geophysical Fluid Dynamics LEcture Series.

WANG, J., GIBSON, J. & WALEFFE, F. 2007 Lower branch coherent states in shear flow: transition and control. *Phys. Rev. Letter* **98**, 20.

WEDIN, H. & KERSWELL, RR. 2004 Exact coherent structures in pipe flow: travelling wave solutions. *J. Fluid Mech.* **508**, 333–371.

WEI, T., FIFE, P., KLEWICKI, J. & MCMURTRY, P. 2005 Properties of the mean momentum balance in turbulent boundary layer, pipe and channel flows. *J. Fluid Mech.* **522**, 303–327.

APPENDIX A

SCALING OF FISSURE THICKNESS

This appendix shows that by accounting for the variation in VF spacing in the context of the self-similar layer hierarchy admitted by the mean momentum balance as derived by Klewicki and collaborators, the associated characteristic dimensional VF thickness Δ_f normalized by h is predicted to decrease like $Re_\tau^{-7/16}$.

At a given large value of the friction Reynolds number $Re_\tau = u_\tau h/\nu$, the fissures in wall-bounded turbulent flows are non-uniformly spaced with distance from the wall. More precisely, observations and theoretical considerations (Klewicki, 2013*a*) indicate that the spacing between adjacent VFs within the inertial domain, i.e. the domain extending from y^+=$O(Re_\tau^{1/2})$ to y^+=$O(Re_\tau)$, increases with distance from the wall according to a geometric progression. Thus, the average spacing $\langle l_y^+ \rangle = (Re_\tau^{1/2} Re_\tau)^{1/2} = Re_\tau^{3/4}$, where the angle brackets refer to the geometric mean. Equivalently, $\langle l_y \rangle = Re_\tau^{-1/4} h$. In the inertial-region SSP identified in this investigation, the fissures are uniformly separated by a distance l_y, and it is found that the ratio of the dimensional fissure thickness to this separation distance $\Delta_f/l_y = O(Re^{-1/4})$, where $Re = u_\tau l_y/\nu$. Replacing l_y with $\langle l_y \rangle$ in the preceding expressions, which is tantamount to interpreting l_y in the asymptotic analysis as the geometric mean spacing of an array of non-uniformly spaced fissures in a turbulent wall flow, yields the estimate

$$\Delta_f/h \;\; = \;\; O(Re_\tau^{-7/16}), \tag{A.1}$$

in reasonable accord with the empirically determined scaling $\Delta_f/h \sim Re_\tau^{-1/2}$.

APPENDIX B

FREDHOLM ALTERNATIVE

This appendix summarizes the Fredholm Alternative.
For a linear boundary value problem $\mathcal{L}\tilde{\mathcal{V}}_4 = f_4$:

- If $\mathcal{L}$ is non-singular, there exists a unique solution to the problem;
- If $\mathcal{L}$ is singular, then either there is no solution, or infinitely many solutions, depending upon whether $(f_f, v^\dagger) = 0$, where $v^\dagger$ satisfies $\mathcal{L}^\dagger v^\dagger = 0$, and $(\cdot, \cdot)$ denotes a suitable inner product.

APPENDIX C

SIMPLIFICATION OF COEFFICIENTS IN AMPLITUDE EQUATION

This appendix shows the simplification of a_x, a_z, and a_0.
Recall that

$$\begin{aligned} a_x &= \fint_{-\infty}^{\infty}\left(\frac{\hat{\mathcal{V}}_3^*}{\overline{\mathcal{U}}_0-c}\right)\Bigg[-\frac{\tilde{k}}{\tilde{\alpha}}(\overline{\mathcal{U}}_0-c)(i\tilde{k}\hat{\mathcal{V}}_3-\partial_{\mathcal{Y}}\hat{\mathcal{U}}_{3r})+\frac{\tilde{k}}{\tilde{\alpha}}(\partial_{\mathcal{Y}}\overline{\mathcal{U}}_0)\hat{\mathcal{U}}_{3r}+\frac{\tilde{\alpha}}{\tilde{k}}\partial_{\mathcal{Y}}\hat{\Pi}_3 \\ &- \partial_{\mathcal{Y}}\overline{\mathcal{U}}_0\left[\frac{\tilde{\alpha}}{\tilde{k}}\hat{\mathcal{U}}_{3r}-\frac{\tilde{\beta}}{\tilde{k}}\hat{\mathcal{W}}_{3r}\right]-(\overline{\mathcal{U}}_0-c)\left[\frac{\tilde{\alpha}}{\tilde{k}}\partial_{\mathcal{Y}}\hat{\mathcal{U}}_{3r}-\frac{\tilde{\beta}}{\tilde{k}}\partial_{\mathcal{Y}}\hat{\mathcal{W}}_{3r}\right]\Bigg]d\mathcal{Y}, \qquad \text{(C.1)} \\ a_z &= \fint_{-\infty}^{\infty}\left(\frac{\hat{\mathcal{V}}_3^*}{\overline{\mathcal{U}}_0-c}\right)\Bigg[\frac{\tilde{\beta}}{\tilde{k}}\partial_{\mathcal{Y}}\hat{\Pi}_3-\partial_{\mathcal{Y}}\overline{\mathcal{U}}_0\left[\frac{\tilde{\beta}}{\tilde{k}}\hat{\mathcal{U}}_{3r}+\frac{\tilde{\alpha}}{\tilde{k}}\hat{\mathcal{W}}_{3r}\right] \\ &- (\overline{\mathcal{U}}_0-c)\,\partial_{\mathcal{Y}}\left(\frac{\tilde{\beta}}{\tilde{k}}\hat{\mathcal{U}}_{3r}+\frac{\tilde{\alpha}}{\tilde{k}}\hat{\mathcal{W}}_{3r}\right)\Bigg]d\mathcal{Y}, \qquad \text{(C.2)} \\ a_0 &= \fint_{-\infty}^{\infty}\left(\frac{\hat{\mathcal{V}}_3^*}{\overline{\mathcal{U}}_0-c}\right)\Bigg[\tilde{\beta}\partial_z\left(\frac{\partial_{\mathcal{Y}}\hat{\Pi}_3}{\tilde{k}}\right)-\partial_{\mathcal{Y}}\overline{\mathcal{U}}_0\partial_z\left[\frac{\tilde{\beta}}{\tilde{k}}\hat{\mathcal{U}}_{3r}+\frac{\tilde{\alpha}}{\tilde{k}}\hat{\mathcal{W}}_{3r}\right] \\ &- (\overline{\mathcal{U}}_0-c)\,\partial_z\left(\partial_{\mathcal{Y}}\left(\frac{\tilde{\beta}}{\tilde{k}}\hat{\mathcal{U}}_{3r}+\frac{\tilde{\alpha}}{\tilde{k}}\hat{\mathcal{W}}_{3r}\right)\right) \\ &+ \partial_z(\partial_{\mathcal{Y}}\overline{\mathcal{U}}_0)\left[\frac{\tilde{\beta}}{\tilde{k}}\hat{\mathcal{U}}_{3r}+\frac{\tilde{\alpha}}{\tilde{k}}\hat{\mathcal{W}}_{3r}\right]+\partial_z\overline{\mathcal{U}}_0\partial_{\mathcal{Y}}\left(\frac{\tilde{\beta}}{\tilde{k}}\hat{\mathcal{U}}_{3r}+\frac{\tilde{\alpha}}{\tilde{k}}\hat{\mathcal{W}}_{3r}\right)\Bigg]d\mathcal{Y}. \qquad \text{(C.3)} \end{aligned}$$

Beginning with a_x we substitute $\partial_{\mathcal{Y}}\hat{\Pi}_3=-i\tilde{k}(\overline{\mathcal{U}}_0-c)\hat{\mathcal{V}}_3$ from (2.44), giving

$$\begin{aligned} a_x =& \fint_{-\infty}^{\infty}\left(\frac{\hat{\mathcal{V}}_3^*}{\overline{\mathcal{U}}_0-c}\right)\Bigg[-\frac{\overline{\mathcal{U}}_0-c}{i\tilde{\alpha}}(-\tilde{k}^2\hat{\mathcal{V}}_3-i\tilde{k}\partial_{\mathcal{Y}}\hat{\mathcal{U}}_{3r})+\frac{\tilde{k}}{\tilde{\alpha}}(\partial_{\mathcal{Y}}\overline{\mathcal{U}}_0)\hat{\mathcal{U}}_{3r}-i\tilde{\alpha}(\overline{\mathcal{U}}_0-c)\hat{\mathcal{V}}_3 \\ &-\partial_{\mathcal{Y}}\left((\overline{\mathcal{U}}_0-c)\left[\frac{\tilde{\alpha}}{\tilde{k}}\hat{\mathcal{U}}_{3r}-\frac{\tilde{\beta}}{\tilde{k}}\hat{\mathcal{W}}_{3r}\right]\right)\Bigg]d\mathcal{Y}. \end{aligned} \qquad \text{(C.4)}$$

Next, we substitute for $\hat{\mathcal{W}}_{3r}$ from (2.46) and use Rayleigh's equation $-\tilde{k}^2\hat{\mathcal{V}}_3-i\tilde{k}\partial_{\mathcal{Y}}\hat{\mathcal{U}}_{3r}=\frac{\hat{\mathcal{V}}_3\partial_{\mathcal{Y}}^2\overline{\mathcal{U}}_0}{\overline{\mathcal{U}}_0-c}$ (indicated by the blue text) to obtain

$$\begin{aligned} a_x =& \fint_{-\infty}^{\infty}\left(\frac{\hat{\mathcal{V}}_3^*}{\overline{\mathcal{U}}_0-c}\right)\Bigg[-\frac{1}{i\tilde{\alpha}}\hat{\mathcal{V}}_3\partial_{\mathcal{Y}}^2\overline{\mathcal{U}}_0+\frac{i\tilde{k}}{i\tilde{\alpha}}(\partial_{\mathcal{Y}}\overline{\mathcal{U}}_0)\hat{\mathcal{U}}_{3r}+\frac{\tilde{\alpha}^2}{i\tilde{\alpha}}(\overline{\mathcal{U}}_0-c)\hat{\mathcal{V}}_3 \\ &-\partial_{\mathcal{Y}}\left((\overline{\mathcal{U}}_0-c)\left[\frac{\tilde{\alpha}}{\tilde{k}}\hat{\mathcal{U}}_{3r}-\frac{\tilde{\beta}}{\tilde{k}}\frac{\tilde{\beta}}{i\tilde{\alpha}\tilde{k}}\frac{\hat{\mathcal{V}}_3\partial_{\mathcal{Y}}\overline{\mathcal{U}}_0}{\overline{\mathcal{U}}_0-c}\right]\right)\Bigg]d\mathcal{Y}. \end{aligned} \qquad \text{(C.5)}$$

Factoring out $1/(i\tilde{\alpha})$ and $1/(i\tilde{\alpha}\tilde{k}^2)$ and utilizing the Eikonal equation $\tilde{\beta}^2 = \tilde{k}^2 - \tilde{\alpha}^2$,

$$\begin{aligned} a_x =& \fint_{-\infty}^{\infty} \left(\frac{\hat{\mathcal{V}}_3^*}{\overline{\mathcal{U}}_0 - c}\right) \left[\frac{1}{i\tilde{\alpha}} \left(-\hat{\mathcal{V}}_3 \partial_{\mathcal{Y}}^2 \overline{\mathcal{U}_0} + i\tilde{k}(\partial_{\mathcal{Y}} \overline{\mathcal{U}}_0)\hat{\mathcal{U}}_{3r} + \tilde{\alpha}^2(\overline{\mathcal{U}}_0 - c)\hat{\mathcal{V}}_3\right)\right. \\ & \left. - \frac{1}{i\tilde{\alpha}}\frac{1}{\tilde{k}^2}\partial_{\mathcal{Y}} \left(\tilde{\alpha}^2 i\tilde{k}\hat{\mathcal{U}}_{3r}(\overline{\mathcal{U}}_0 - c) - \tilde{\beta}^2 \hat{\mathcal{V}}_3 \partial_{\mathcal{Y}} \overline{\mathcal{U}_0}\right)\right] d\mathcal{Y} \\ =& \fint_{-\infty}^{\infty} \left(\frac{\hat{\mathcal{V}}_3^*}{\overline{\mathcal{U}}_0 - c}\right) \left[\frac{1}{i\tilde{\alpha}} \left(-\hat{\mathcal{V}}_3 \partial_{\mathcal{Y}}^2 \overline{\mathcal{U}_0} + i\tilde{k}(\partial_{\mathcal{Y}} \overline{\mathcal{U}}_0)\hat{\mathcal{U}}_{3r} + \tilde{\alpha}^2(\overline{\mathcal{U}}_0 - c)\hat{\mathcal{V}}_3\right)\right. \\ & \left. - \frac{1}{i\tilde{\alpha}}\frac{1}{\tilde{k}^2}\partial_{\mathcal{Y}} \left(\tilde{\alpha}^2 i\tilde{k}\hat{\mathcal{U}}_{3r}(\overline{\mathcal{U}}_0 - c) + \tilde{\alpha}^2 \hat{\mathcal{V}}_3 \partial_{\mathcal{Y}} \overline{\mathcal{U}_0} - \tilde{k}^2 \hat{\mathcal{V}}_3 \partial_{\mathcal{Y}} \overline{\mathcal{U}_0}\right)\right] d\mathcal{Y}. \end{aligned} \tag{C.6}$$

We now distribute the $\partial_{\mathcal{Y}}$ derivative and strategically collect terms, giving

$$\begin{aligned} a_x =& \fint_{-\infty}^{\infty} \left(\frac{\hat{\mathcal{V}}_3^*}{\overline{\mathcal{U}}_0 - c}\right) \left[\frac{1}{i\tilde{\alpha}} \left(-\hat{\mathcal{V}}_3 \partial_{\mathcal{Y}}^2 \overline{\mathcal{U}_0} + i\tilde{k}(\partial_{\mathcal{Y}} \overline{\mathcal{U}}_0)\hat{\mathcal{U}}_{3r} + \tilde{\alpha}^2(\overline{\mathcal{U}}_0 - c)\hat{\mathcal{V}}_3 + \partial_{\mathcal{Y}}\hat{\mathcal{V}}_3 \partial_{\mathcal{Y}} \overline{\mathcal{U}_0} + \hat{\mathcal{V}}_3 \partial_{\mathcal{Y}}^2 \overline{\mathcal{U}_0}\right)\right. \\ & \left. - \frac{1}{i\tilde{\alpha}}\frac{\tilde{\alpha}^2}{\tilde{k}^2} \left(i\tilde{k}(\partial_{\mathcal{Y}}\hat{\mathcal{U}}_{3r})(\overline{\mathcal{U}}_0 - c) + i\tilde{k}\hat{\mathcal{U}}_{3r}(\partial_{\mathcal{Y}} \overline{\mathcal{U}}_0) + (\partial_{\mathcal{Y}}\hat{\mathcal{V}}_3)\partial_{\mathcal{Y}} \overline{\mathcal{U}_0} + \hat{\mathcal{V}}_3 \partial_{\mathcal{Y}}^2 \overline{\mathcal{U}_0}\right)\right] d\mathcal{Y}. \end{aligned} \tag{C.7}$$

The terms indicated in red cancel owing to the incompressibility condition, while the terms in blue comprise Rayleigh's equation. Consequently,

$$a_x = \fint_{-\infty}^{\infty} \left(\frac{\hat{\mathcal{V}}_3^*}{\overline{\mathcal{U}}_0 - c}\right) \left[\frac{1}{i\tilde{\alpha}}\tilde{\alpha}^2(\overline{\mathcal{U}}_0 - c)\hat{\mathcal{V}}_3 - \frac{1}{i\tilde{\alpha}}\frac{\tilde{\alpha}^2}{\tilde{k}^2}\left(-\tilde{k}^2(\overline{\mathcal{U}}_0 - c)\hat{\mathcal{V}}_3\right)\right] d\mathcal{Y}, \tag{C.8}$$

i.e.,

$$a_x = -2i\tilde{\alpha}\int_{-\infty}^{\infty} \hat{\mathcal{V}}_3 \hat{\mathcal{V}}_3^* d\mathcal{Y}. \tag{C.9}$$

Thus $\hat{\mathcal{V}}_3$ is bounded throughout the VF and exponentially decays to 0 as $\mathcal{Y} \to \pm\infty$. Accordingly, a_x is not singular near the CL and is integrable across the VF.

We next examine the expression for a_z, again making the substitution $\partial_{\mathcal{Y}}\hat{\Pi}_3 = -i\tilde{k}(\overline{\mathcal{U}}_0 - c)\hat{\mathcal{V}}_3$ and integrating by parts:

$$\begin{aligned} a_z =& \fint_{-\infty}^{\infty} \left(\frac{\hat{\mathcal{V}}_3^*}{\overline{\mathcal{U}}_0 - c}\right) \left[\frac{\tilde{\beta}}{\tilde{k}}\partial_{\mathcal{Y}}\hat{\Pi}_3 - \partial_{\mathcal{Y}}\overline{\mathcal{U}}_0 \left[\frac{\tilde{\beta}}{\tilde{k}}\hat{\mathcal{U}}_{3r} + \frac{\tilde{\alpha}}{\tilde{k}}\hat{\mathcal{W}}_{3r}\right] - (\overline{\mathcal{U}}_0 - c)\,\partial_{\mathcal{Y}}\left(\frac{\tilde{\beta}}{\tilde{k}}\hat{\mathcal{U}}_{3r} + \frac{\tilde{\alpha}}{\tilde{k}}\hat{\mathcal{W}}_{3r}\right)\right] d\mathcal{Y} \\ =& \fint_{-\infty}^{\infty} \left(\frac{\hat{\mathcal{V}}_3^*}{\overline{\mathcal{U}}_0 - c}\right) \left[-i\tilde{\beta}(\overline{\mathcal{U}}_0 - c)\hat{\mathcal{V}}_3 - \partial_{\mathcal{Y}}\left((\overline{\mathcal{U}}_0 - c)\left[\frac{\tilde{\beta}}{\tilde{k}}\hat{\mathcal{U}}_{3r} + \frac{\tilde{\alpha}}{\tilde{k}}\hat{\mathcal{W}}_{3r}\right]\right)\right] d\mathcal{Y}. \end{aligned} \tag{C.10}$$

We next substitute for $\hat{\mathcal{W}}_{3r}$ and then distribute $(\overline{\mathcal{U}}_0 - c)$ within the derivative:

$$\begin{aligned} a_z =& \fint_{-\infty}^{\infty} \left(\frac{\hat{\mathcal{V}}_3^*}{\overline{\mathcal{U}}_0 - c} \right) \left[-i\tilde{\beta}(\overline{\mathcal{U}}_0 - c)\hat{\mathcal{V}}_3 - \frac{\tilde{\beta}}{i\tilde{k}^2}\partial_{\mathcal{Y}} \left((\overline{\mathcal{U}}_0 - c) \left[i\tilde{k}\hat{\mathcal{U}}_{3r} + \frac{\hat{\mathcal{V}}_3 \partial_{\mathcal{Y}} \overline{\mathcal{U}}_0}{\overline{\mathcal{U}}_0 - c} \right] \right) \right] d\mathcal{Y} \\ =& \fint_{-\infty}^{\infty} \left(\frac{\hat{\mathcal{V}}_3^*}{\overline{\mathcal{U}}_0 - c} \right) \left[-i\tilde{\beta}(\overline{\mathcal{U}}_0 - c)\hat{\mathcal{V}}_3 - \frac{\tilde{\beta}}{i\tilde{k}^2}\partial_{\mathcal{Y}} \left((\overline{\mathcal{U}}_0 - c) i\tilde{k}\hat{\mathcal{U}}_{3r} + \hat{\mathcal{V}}_3 \partial_{\mathcal{Y}} \overline{\mathcal{U}}_0 \right) \right] d\mathcal{Y} \\ =& \fint_{-\infty}^{\infty} \left(\frac{\hat{\mathcal{V}}_3^*}{\overline{\mathcal{U}}_0 - c} \right) \Bigg[- i\tilde{\beta}(\overline{\mathcal{U}}_0 - c)\hat{\mathcal{V}}_3 \\ & - \frac{\tilde{\beta}}{i\tilde{k}^2} \left(\partial_{\mathcal{Y}} \overline{\mathcal{U}}_0 (i\tilde{k}\hat{\mathcal{U}}_{3r}) + i\tilde{k}(\overline{\mathcal{U}}_0 - c)\partial_{\mathcal{Y}}\hat{\mathcal{U}}_{3r} + \partial_{\mathcal{Y}}\hat{\mathcal{V}}_3 \partial_{\mathcal{Y}} \overline{\mathcal{U}}_0 + \hat{\mathcal{V}}_3 \partial_{\mathcal{Y}}^2 \overline{\mathcal{U}}_0 \right) \Bigg] d\mathcal{Y}. \end{aligned} \tag{C.11}$$

As for a_x, the red terms cancel owing to incompressibility and the blue terms constitute Rayleigh's equation, enabling further simplification; i.e.,

$$\begin{aligned} a_z =& \fint_{-\infty}^{\infty} \left(\frac{\hat{\mathcal{V}}_3^*}{\overline{\mathcal{U}}_0 - c} \right) \left[-i\tilde{\beta}(\overline{\mathcal{U}}_0 - c)\hat{\mathcal{V}}_3 - \frac{\tilde{\beta}}{i\tilde{k}^2} \left(i\tilde{k}(\overline{\mathcal{U}}_0 - c)\partial_{\mathcal{Y}}\hat{\mathcal{U}}_{3r} + \hat{\mathcal{V}}_3 \partial_{\mathcal{Y}}^2 \overline{\mathcal{U}}_0 \right) \right] d\mathcal{Y} \\ =& \fint_{-\infty}^{\infty} \left(\frac{\hat{\mathcal{V}}_3^*}{\overline{\mathcal{U}}_0 - c} \right) \frac{\tilde{\beta}}{i\tilde{k}^2} \left[\tilde{k}^2(\overline{\mathcal{U}}_0 - c)\hat{\mathcal{V}}_3 - i\tilde{k}(\overline{\mathcal{U}}_0 - c)\partial_{\mathcal{Y}}\hat{\mathcal{U}}_{3r} - \hat{\mathcal{V}}_3 \partial_{\mathcal{Y}}^2 \overline{\mathcal{U}}_0 \right] d\mathcal{Y} \\ =& \fint_{-\infty}^{\infty} \left(\frac{\hat{\mathcal{V}}_3^*}{\overline{\mathcal{U}}_0 - c} \right) \frac{\tilde{\beta}}{i\tilde{k}^2} \left[2\tilde{k}^2(\overline{\mathcal{U}}_0 - c)\hat{\mathcal{V}}_3 \right] d\mathcal{Y}. \end{aligned} \tag{C.12}$$

Finally, we obtain

$$a_z = -2i\tilde{\beta} \int_{-\infty}^{\infty} \hat{\mathcal{V}}_3^* \hat{\mathcal{V}}_3 d\mathcal{Y}. \tag{C.13}$$

Note that a_z has a form similar to a_x except that $\tilde{\beta}$ rather than $\tilde{\alpha}$ multiplies the integral. Again, $\hat{\mathcal{V}}_3$ is bounded throughout the VF and exponentially approaches 0 as $\mathcal{Y} \to \pm\infty$, implying that a_z is not singular near the CL and is integrable across the VF.

Using $\partial_{\mathcal{Y}}\hat{\Pi}_3 = -i\tilde{k}(\overline{\mathcal{U}}_0 - c)\hat{\mathcal{V}}_3$ and integrating by parts,

$$\begin{aligned} a_0 =& \fint_{-\infty}^{\infty} \left(\frac{\hat{\mathcal{V}}_3^*}{\overline{\mathcal{U}}_0 - c} \right) \Bigg[- \tilde{\beta}\partial_z \Big(i(\overline{\mathcal{U}}_0 - c)\hat{\mathcal{V}}_3 \Big) - \partial_{\mathcal{Y}} \left(\partial_z \left((\overline{\mathcal{U}}_0 - c) \left(\frac{\tilde{\beta}}{\tilde{k}}\hat{\mathcal{U}}_{3r} + \frac{\tilde{\alpha}}{\tilde{k}}\hat{\mathcal{W}}_{3r} \right) \right) \right) \\ & + 2\partial_{\mathcal{Y}} \left(\partial_z \overline{\mathcal{U}}_0 \left[\frac{\tilde{\beta}}{\tilde{k}}\hat{\mathcal{U}}_{3r} + \frac{\tilde{\alpha}}{\tilde{k}}\hat{\mathcal{W}}_{3r} \right] \right) \Bigg] d\mathcal{Y}. \end{aligned} \tag{C.14}$$

We again substitute for $\hat{\mathcal{W}}_{3r}$ and then distribute and factor out $(\overline{\mathcal{U}}_0 - c)$ from various terms to obtain

$$
\begin{aligned}
a_0 =& \fint_{-\infty}^{\infty} \left(\frac{\hat{\mathcal{V}}_3^*}{\overline{\mathcal{U}}_0 - c}\right)\Bigg[-\tilde{\beta}\partial_z\Big(i(\overline{\mathcal{U}}_0 - c)\hat{\mathcal{V}}_3\Big) - \partial_z\left(\partial_{\mathcal{Y}}\left((\overline{\mathcal{U}}_0 - c)\left(\frac{\tilde{\beta}}{\tilde{k}}\hat{\mathcal{U}}_{3r} + \frac{\tilde{\beta}}{i\tilde{k}^2}\frac{\hat{\mathcal{V}}_3\partial_{\mathcal{Y}}\overline{\mathcal{U}}_0}{\overline{\mathcal{U}}_0 - c}\right)\right)\right) \\
&+ 2\partial_{\mathcal{Y}}\left(\partial_z\overline{\mathcal{U}}_0\left[\frac{\tilde{\beta}}{\tilde{k}}\hat{\mathcal{U}}_{3r} + \frac{\tilde{\beta}}{i\tilde{k}^2}\frac{\hat{\mathcal{V}}_3\partial_{\mathcal{Y}}\overline{\mathcal{U}}_0}{\overline{\mathcal{U}}_0 - c}\right]\right)\Bigg] d\mathcal{Y}, \\
a_0 =& \fint_{-\infty}^{\infty} \left(\frac{\hat{\mathcal{V}}_3^*}{\overline{\mathcal{U}}_0 - c}\right)\Bigg[-\tilde{\beta}\partial_z\Big(i(\overline{\mathcal{U}}_0 - c)\hat{\mathcal{V}}_3\Big) - \partial_z\left(\frac{\tilde{\beta}}{i\tilde{k}^2}\partial_{\mathcal{Y}}\left(i\tilde{k}(\overline{\mathcal{U}}_0 - c)\hat{\mathcal{U}}_{3r} + \hat{\mathcal{V}}_3\partial_{\mathcal{Y}}\overline{\mathcal{U}}_0\right)\right) \\
&+ 2\frac{\tilde{\beta}}{i\tilde{k}^2}\partial_{\mathcal{Y}}\left(\frac{\partial_z\overline{\mathcal{U}}_0}{\overline{\mathcal{U}}_0 - c}\left[i\tilde{k}(\overline{\mathcal{U}}_0 - c)\hat{\mathcal{U}}_{3r} + \hat{\mathcal{V}}_3\partial_{\mathcal{Y}}\overline{\mathcal{U}}_0\right]\right)\Bigg] d\mathcal{Y}.
\end{aligned}
\tag{C.15}
$$

Expanding the $\partial_{\mathcal{Y}}$ derivatives yields

$$
\begin{aligned}
a_0 =& \fint_{-\infty}^{\infty} \left(\frac{\hat{\mathcal{V}}_3^*}{\overline{\mathcal{U}}_0 - c}\right)\Bigg[-\tilde{\beta}\partial_z\Big(i(\overline{\mathcal{U}}_0 - c)\hat{\mathcal{V}}_3\Big) \\
&- \partial_z\left(\frac{\tilde{\beta}}{i\tilde{k}^2}\left(i\tilde{k}(\overline{\mathcal{U}}_0 - c)(\partial_{\mathcal{Y}}\hat{\mathcal{U}}_{3r}) + i\tilde{k}(\partial_{\mathcal{Y}}\overline{\mathcal{U}}_0)\hat{\mathcal{U}}_{3r} + (\partial_{\mathcal{Y}}\hat{\mathcal{V}}_3)\partial_{\mathcal{Y}}\overline{\mathcal{U}_0} + \hat{\mathcal{V}}_3\partial_{\mathcal{Y}}^2\overline{\mathcal{U}_0}\right)\right) \\
&+ 2\frac{\tilde{\beta}}{i\tilde{k}^2}\partial_{\mathcal{Y}}\left(\frac{\partial_z\overline{\mathcal{U}}_0}{\overline{\mathcal{U}}_0 - c}\right)\left[i\tilde{k}(\overline{\mathcal{U}}_0 - c)\hat{\mathcal{U}}_{3r} + \hat{\mathcal{V}}_3\partial_{\mathcal{Y}}\overline{\mathcal{U}_0}\right] \\
&+ 2\frac{\tilde{\beta}}{i\tilde{k}^2}\frac{\partial_z\overline{\mathcal{U}}_0}{\overline{\mathcal{U}}_0 - c}\left(i\tilde{k}(\overline{\mathcal{U}}_0 - c)(\partial_{\mathcal{Y}}\hat{\mathcal{U}}_{3r}) + i\tilde{k}(\partial_{\mathcal{Y}}\overline{\mathcal{U}}_0)\hat{\mathcal{U}}_{3r} + (\partial_{\mathcal{Y}}\hat{\mathcal{V}}_3)\partial_{\mathcal{Y}}\overline{\mathcal{U}_0} + \hat{\mathcal{V}}_3\partial_{\mathcal{Y}}^2\overline{\mathcal{U}_0}\right)\Bigg] d\mathcal{Y}.
\end{aligned}
\tag{C.16}
$$

The terms in red cancel owing to continuity while the terms in blue can be combined to obtain a multiple of Rayleigh's equation. Using these simplifications,

$$
\begin{aligned}
a_0 =& \fint_{-\infty}^{\infty} \left(\frac{\hat{\mathcal{V}}_3^*}{\overline{\mathcal{U}}_0 - c}\right)\Bigg[-\tilde{\beta}\partial_z\Big(i(\overline{\mathcal{U}}_0 - c)\hat{\mathcal{V}}_3\Big) - \partial_z\left(\frac{\tilde{\beta}}{i\tilde{k}^2}\left(-\tilde{k}^2(\overline{\mathcal{U}}_0 - c)\hat{\mathcal{V}}_3\right)\right) \\
&+ 2\frac{\tilde{\beta}}{i\tilde{k}^2}\partial_{\mathcal{Y}}\left(\frac{\partial_z\overline{\mathcal{U}}_0}{\overline{\mathcal{U}}_0 - c}\right)\left[i\tilde{k}(\overline{\mathcal{U}}_0 - c)\hat{\mathcal{U}}_{3r} + \hat{\mathcal{V}}_3\partial_{\mathcal{Y}}\overline{\mathcal{U}_0}\right] + 2\frac{\tilde{\beta}}{i\tilde{k}^2}\frac{\partial_z\overline{\mathcal{U}}_0}{\overline{\mathcal{U}}_0 - c}\left(-\tilde{k}^2(\overline{\mathcal{U}}_0 - c)\hat{\mathcal{V}}_3\right)\Bigg] d\mathcal{Y} \\
=& \fint_{-\infty}^{\infty} \left(\frac{\hat{\mathcal{V}}_3^*}{\overline{\mathcal{U}}_0 - c}\right)\Bigg[-\tilde{\beta}\partial_z\Big(i(\overline{\mathcal{U}}_0 - c)\hat{\mathcal{V}}_3\Big) - \partial_z\left(i\tilde{\beta}(\overline{\mathcal{U}}_0 - c)\hat{\mathcal{V}}_3\right) + 2i\tilde{\beta}(\partial_z\overline{\mathcal{U}}_0)\hat{\mathcal{V}}_3 \\
&- 2\frac{i\tilde{\beta}}{\tilde{k}^2}\partial_{\mathcal{Y}}\left(\frac{\partial_z\overline{\mathcal{U}}_0}{\overline{\mathcal{U}}_0 - c}\right)\left[i\tilde{k}(\overline{\mathcal{U}}_0 - c)\hat{\mathcal{U}}_{3r} + \hat{\mathcal{V}}_3\partial_{\mathcal{Y}}\overline{\mathcal{U}_0}\right]\Bigg] d\mathcal{Y}.
\end{aligned}
\tag{C.17}
$$

Next, we expand the ∂_z derivatives and group like terms to obtain

$$
\begin{aligned}
a_0 = &- i\int_{-\infty}^{\infty}\left(\frac{\hat{\mathcal{V}}_3^*}{\overline{\mathcal{U}}_0 - c}\right)\Bigg[2\tilde{\beta}(\overline{\mathcal{U}}_0 - c)\partial_z(\hat{\mathcal{V}}_3) + (\partial_z\tilde{\beta})(\overline{\mathcal{U}}_0 - c)\hat{\mathcal{V}}_3 \\
&+ 2\frac{\tilde{\beta}}{\tilde{k}^2}\partial_{\mathcal{Y}}\left(\frac{\partial_z\overline{\mathcal{U}}_0}{\overline{\mathcal{U}}_0 - c}\right)\left[i\tilde{k}(\overline{\mathcal{U}}_0 - c)\hat{\mathcal{U}}_{3r}\right] + 2\frac{\tilde{\beta}}{\tilde{k}^2}\partial_{\mathcal{Y}}\left(\frac{\partial_z\overline{\mathcal{U}}_0}{\overline{\mathcal{U}}_0 - c}\right)\left[\hat{\mathcal{V}}_3\partial_{\mathcal{Y}}\overline{\mathcal{U}_0}\right]\Bigg]d\mathcal{Y} \\
= &- i\int_{-\infty}^{\infty}\Bigg[2\tilde{\beta}\partial_z(\hat{\mathcal{V}}_3)\hat{\mathcal{V}}_3^* + (\partial_z\tilde{\beta})\hat{\mathcal{V}}_3\hat{\mathcal{V}}_3^* - \underbrace{2\frac{\tilde{\beta}}{\tilde{k}^2}\partial_{\mathcal{Y}}\left(\frac{\partial_z\overline{\mathcal{U}}_0}{\overline{\mathcal{U}}_0 - c}\right)(\partial_{\mathcal{Y}}\hat{\mathcal{V}}_3)\hat{\mathcal{V}}_3^*}_{1} \\
&+ \underbrace{2\frac{\tilde{\beta}}{\tilde{k}^2}\partial_{\mathcal{Y}}\left(\frac{\partial_z\overline{\mathcal{U}}_0}{\overline{\mathcal{U}}_0 - c}\right)\left[\frac{\hat{\mathcal{V}}_3\hat{\mathcal{V}}_3^*\partial_{\mathcal{Y}}\overline{\mathcal{U}_0}}{\overline{\mathcal{U}}_0 - c}\right]}_{2}\Bigg]d\mathcal{Y}.
\end{aligned}
\tag{C.18}
$$

The resulting expression for a_0 still apparently contains potentially singular terms indicated by the underbraces in (C.18). We start by analyzing the first potentially singular term:

$$
2\frac{\tilde{\beta}}{\tilde{k}^2}\partial_{\mathcal{Y}}\left(\frac{\partial_z\overline{\mathcal{U}}_0}{\overline{\mathcal{U}}_0 - c}\right)(\partial_{\mathcal{Y}}\hat{\mathcal{V}}_3)\hat{\mathcal{V}}_3^*. \tag{C.19}
$$

Since $(\overline{\mathcal{U}}_0 - c) \to \tilde{\lambda}\mathcal{Y}$ as $\mathcal{Y} \to 0$ (where $\tilde{\lambda} = \tilde{\lambda}(z)$), a corollary is that $\partial_{\mathcal{Y}}\left(\frac{\partial_z\overline{\mathcal{U}}_0}{\overline{\mathcal{U}}_0 - c}\right) \to \frac{\partial_z\tilde{\lambda}}{\tilde{\lambda}}\partial_{\mathcal{Y}}\left(\frac{\mathcal{Y}}{\mathcal{Y}}\right)$ as $\mathcal{Y} \to 0$; i.e., $\partial_{\mathcal{Y}}\left(\frac{\partial_z\overline{\mathcal{U}}_0}{\overline{\mathcal{U}}_0 - c}\right) \to 0$ as $\mathcal{Y} \to 0$. Hence, the term indicated by underbrace 'one' goes to zero as the CL is approached and is not singular. Next, we analyze the term highlighted by the underbrace 'two',

$$
2\frac{\tilde{\beta}}{\tilde{k}^2}\partial_{\mathcal{Y}}\left(\frac{\partial_z\overline{\mathcal{U}}_0}{\overline{\mathcal{U}}_0 - c}\right)\left[\frac{\hat{\mathcal{V}}_3\hat{\mathcal{V}}_3^*\partial_{\mathcal{Y}}\overline{\mathcal{U}_0}}{\overline{\mathcal{U}}_0 - c}\right]. \tag{C.20}
$$

The important observation here is that $\partial_{\mathcal{Y}}\left(\frac{\partial_z\overline{\mathcal{U}}_0}{\overline{\mathcal{U}}_0 - c}\right) \to 0$ at the same rate as $(\overline{\mathcal{U}}_0 - c) \to 0$, implying that this term approaches a constant as $\mathcal{Y} \to 0$. Consequently, the integrand in (C.18) is not singular near $\mathcal{Y} = 0$ and goes exponentially to zero away from the CL, confirming that it is integrable across the VF. Consequently, each of the coefficients a_x, a_z, and a_0 in the amplitude equation (2.70) is bounded.

APPENDIX D

CAUSTICS

This appendix provides a detailed analysis of the flow within the caustics.

First, taking the divergence of (2.38)–(2.41) yields an equation for the fluctuation pressure in the VF:

$$\partial_{\mathcal{Y}}^2 \hat{\mathcal{P}}_3 \; - 2 \left(\frac{\partial_{\mathcal{Y}} \overline{\mathcal{U}}_0}{\overline{\mathcal{U}}_0 - c} \right) \partial_{\mathcal{Y}} \hat{\mathcal{P}}_3 \; = \tilde{k}^2 \hat{\mathcal{P}}_3, \tag{D.1}$$

where, again, $\tilde{\alpha}^2 + \tilde{\beta}^2 = \tilde{k}^2$ is the Eikonal equation. The boundary and symmetry conditions on the fluctuation pressure, respectively, are

$$|\mathcal{Y}| \;\; \rightarrow \;\; \infty : \mathcal{P}_3' \rightarrow 0, \tag{D.2}$$

$$\mathcal{Y} \;\; = \;\; 0 : \partial_{\mathcal{Y}} \mathcal{P}_3' = 0. \tag{D.3}$$

The WKBJ solution for the fluctuation pressure given in (2.21) breaks down near each caustic. To find a uniformly valid solution for all z within VF, we begin with an expansion similar to the ansatz employed by Ludwig (1966) and McKee (1973):

$$\mathcal{P}' \sim \tilde{\Delta}^{17/6} \hat{\mathcal{P}}_3(\mathcal{Y}, z) \left[F(\mathcal{Y}, z) \mathrm{Ai} \left(-\frac{\tilde{\xi}(z)}{\tilde{\Delta}^{2/3}} \right) + i \tilde{\Delta}^{1/3} G(\mathcal{Y}, z) \mathrm{Ai}' \left(-\frac{\tilde{\xi}(z)}{\tilde{\Delta}^{2/3}} \right) \right] e^{i(\tilde{\alpha}/\tilde{\Delta})(x - ct)} + c.c., \tag{D.4}$$

where $\hat{\mathcal{P}}_3$ solves (D.1) and Ai is the Airy function such that

$$\mathrm{Ai}''(z) - z\mathrm{Ai}(z) = 0, \tag{D.5}$$

$$\mathrm{Ai}'''(z) - z\mathrm{Ai}'(z) - \mathrm{Ai}(z) = 0. \tag{D.6}$$

Using these identities and ansatz for $\mathcal{P}_3'$, spatial derivatives become

$$\partial_{\mathcal{Y}}\mathcal{P}' = \tilde{\Delta}^{17/6}\left(\partial_{\mathcal{Y}}\hat{\mathcal{P}}_3\left[F\mathrm{Ai}+i\tilde{\Delta}^{1/3}G\mathrm{Ai}'\right]+\hat{\mathcal{P}}_3\left[\partial_{\mathcal{Y}}F\mathrm{Ai}+i\tilde{\Delta}^{1/3}\partial_{\mathcal{Y}}G\mathrm{Ai}'\right]\right)e^{i(\tilde{\alpha}/\tilde{\Delta})(x-ct)}+c.c., \tag{D.7}$$

$$\begin{aligned}\partial_{\mathcal{Y}}^2\mathcal{P}' &= \tilde{\Delta}^{17/6}\Bigg(\partial_{\mathcal{Y}}^2\hat{\mathcal{P}}_3\left[F\mathrm{Ai}+i\tilde{\Delta}^{1/3}G\mathrm{Ai}'\right]+2\partial_{\mathcal{Y}}\hat{\mathcal{P}}_3\left[\partial_{\mathcal{Y}}F\mathrm{Ai}+i\tilde{\Delta}^{1/3}\partial_{\mathcal{Y}}G\mathrm{Ai}'\right]\\ &+ \hat{\mathcal{P}}_3\left[\partial_{\mathcal{Y}}^2F\mathrm{Ai}+i\tilde{\Delta}^{1/3}\partial_{\mathcal{Y}}^2G\mathrm{Ai}'\right]\Bigg)e^{i(\tilde{\alpha}/\tilde{\Delta})(x-ct)}+c.c.,\end{aligned} \tag{D.8}$$

$$\begin{aligned}\partial_z\mathcal{P}' &= \tilde{\Delta}^{17/6}\Bigg(\partial_z\hat{\mathcal{P}}_3\left[F\mathrm{Ai}+i\tilde{\Delta}^{1/3}G\mathrm{Ai}'\right]\\ &+ \hat{\mathcal{P}}_3\left[\partial_zF\mathrm{Ai}-\tilde{\Delta}^{-2/3}\partial_z\tilde{\xi}F\mathrm{Ai}'+i\tilde{\Delta}^{1/3}\partial_zG\mathrm{Ai}'+i\tilde{\Delta}^{-1}\tilde{\xi}\partial_z\tilde{\xi}G\mathrm{Ai}\right]\Bigg)e^{i(\tilde{\alpha}/\tilde{\Delta})(x-ct)}+c.c.,\end{aligned} \tag{D.9}$$

$$\begin{aligned}\partial_z^2\mathcal{P}' &= \tilde{\Delta}^{17/6}\Bigg(\partial_z^2\hat{\mathcal{P}}_3\left[F\mathrm{Ai}+i\tilde{\Delta}^{1/3}G\mathrm{Ai}'\right]+2\partial_z\hat{\mathcal{P}}_3\left[\partial_zF\mathrm{Ai}-\tilde{\Delta}^{-2/3}\partial_z\tilde{\xi}F\mathrm{Ai}'+i\tilde{\Delta}^{1/3}\partial_zG\mathrm{Ai}'\right.\\ &+ \left.i\tilde{\Delta}^{-1}\tilde{\xi}\partial_z\tilde{\xi}G\mathrm{Ai}\right]+\hat{\mathcal{P}}_3\left[\partial_z^2F\mathrm{Ai}-2\tilde{\Delta}^{-2/3}\partial_z\tilde{\xi}\partial_zF\mathrm{Ai}'-\tilde{\Delta}^{-2/3}\partial_z^2\tilde{\xi}F\mathrm{Ai}'-\tilde{\Delta}^{-2}\tilde{\xi}(\partial_z\tilde{\xi})^2F\mathrm{Ai}\right]\\ &+ \hat{\mathcal{P}}_3\Bigg[i\tilde{\Delta}^{1/3}\partial_z^2G\mathrm{Ai}'+2i\tilde{\Delta}^{-1}\tilde{\xi}\partial_z\tilde{\xi}\partial_zG\mathrm{Ai}+i\tilde{\Delta}^{-1}\tilde{\xi}\partial_z^2\tilde{\xi}G\mathrm{Ai}\\ &+ \left.i\tilde{\Delta}^{-1}(\partial_z\tilde{\xi})^2G\mathrm{Ai}-i\tilde{\Delta}^{-5/3}\tilde{\xi}(\partial_z\tilde{\xi})^2G\mathrm{Ai}'\right]\Bigg)e^{i(\tilde{\alpha}/\tilde{\Delta})(x-ct)}+c.c.,\end{aligned} \tag{D.10}$$

where

$$F \sim F_0(z)+\sum_{m=1}^{\infty}\left(\frac{\tilde{\Delta}}{i}\right)^m F_m(\mathcal{Y},z), \tag{D.11}$$

$$G \sim G_0(z)+\sum_{m=1}^{\infty}\left(\frac{\tilde{\Delta}}{i}\right)^m G_m(\mathcal{Y},z). \tag{D.12}$$

We substitute this modified ansatz and expansion into the NS equations. At leading order,

$$\tilde{\alpha}^2+\tilde{\xi}(\partial_z\tilde{\xi})^2=\tilde{k}^2. \tag{D.13}$$

Equation (D.13) is analogous to the Eikonal equation obtained using the WKBJ ansatz, and its solution can be expressed as

$$\frac{2}{3}\tilde{\xi}^{3/2}=-\int_{z_c}^{z}\left(\tilde{k}^2(t)-\tilde{\alpha}^2\right)^{1/2}dt \quad z<z_c, \tag{D.14}$$

$$\frac{2}{3}(-\tilde{\xi})^{3/2}=\int_{z_c}^{z}\left(\tilde{\alpha}^2-\tilde{k}^2(t)\right)^{1/2}dt \quad z>z_c, \tag{D.15}$$

where z_c is the spanwise location of the caustic. Next, we collect terms at like orders in $\tilde{\Delta}$ to obtain

$$\begin{aligned}
-\hat{\mathcal{P}}_3\partial_{\mathcal{Y}}^2 F_m &- 2\partial_{\mathcal{Y}}\hat{\mathcal{P}}_3\partial_{\mathcal{Y}}F_m + 2\left(\frac{\partial_{\mathcal{Y}}\overline{\mathcal{U}}_0}{\overline{\mathcal{U}}_0 - c}\right)\partial_{\mathcal{Y}}F_m - 2\left(\frac{\partial_z\overline{\mathcal{U}}_0}{\overline{\mathcal{U}}_0 - c}\right)\left[\partial_z(\hat{\mathcal{P}}_3 F_{m-2}) + \hat{\mathcal{P}}_3\tilde{\xi}\partial_z\tilde{\xi}G_{m-1}\right] \\
&+ \left[\partial_z^2(\hat{\mathcal{P}}_3 F_{m-2}) + \partial_z(\hat{\mathcal{P}}_3 G_{m-1})\tilde{\xi}\partial_z\tilde{\xi} + \partial_z(\hat{\mathcal{P}}_3 G_{m-1}\tilde{\xi}\partial_z\tilde{\xi})\right] = 0, \qquad \text{(D.16)} \\
-\hat{\mathcal{P}}_3\partial_{\mathcal{Y}}^2 G_m &- 2\partial_{\mathcal{Y}}\hat{\mathcal{P}}_3\partial_{\mathcal{Y}}G_m + 2\left(\frac{\partial_{\mathcal{Y}}\overline{\mathcal{U}}_0}{\overline{\mathcal{U}}_0 - c}\right)\hat{\mathcal{P}}_3\partial_{\mathcal{Y}}G_m - 2\left(\frac{\partial_z\overline{\mathcal{U}}_0}{\overline{\mathcal{U}}_0 - c}\right)\left[\partial_z(\hat{\mathcal{P}}_3 G_{m-2}) + \hat{\mathcal{P}}_3\partial_z\tilde{\xi}F_{m-1}\right] \\
&+ \left[\partial_z^2(\hat{\mathcal{P}}_3 G_{m-2}) + \partial_z(\hat{\mathcal{P}}_3 F_{m-1})\partial_z\tilde{\xi} + \partial_z(\hat{\mathcal{P}}_3 F_{m-1}\partial_z\tilde{\xi})\right] = 0, \qquad \text{(D.17)}
\end{aligned}$$

for each $m = 1, 2, 3\ldots$. Equations (D.16)–(D.17) are the so-called *transport equations*.

The equations for (F, G) reduce to

$$\begin{aligned}
&\hat{\mathcal{P}}_3\partial_{\mathcal{Y}}^2 F_1 + 2\partial_{\mathcal{Y}}\hat{\mathcal{P}}_3\partial_{\mathcal{Y}}F_1 - 2\left(\frac{\partial_{\mathcal{Y}}\overline{\mathcal{U}}_0}{\overline{\mathcal{U}}_0 - c}\right)\partial_{\mathcal{Y}}F_1 = \\
&\qquad \partial_z(\hat{\mathcal{P}}_3 G_0)\tilde{\xi}\partial_z\tilde{\xi} + \partial_z(\hat{\mathcal{P}}_3 G_0\tilde{\xi}\partial_z\tilde{\xi}) - 2\left(\frac{\partial_z\overline{\mathcal{U}}_0}{\overline{\mathcal{U}}_0 - c}\right)\hat{\mathcal{P}}_3\tilde{\xi}\partial_z\tilde{\xi}G_0, \qquad \text{(D.18)} \\
&\hat{\mathcal{P}}_3\partial_{\mathcal{Y}}^2 G_1 + 2\partial_{\mathcal{Y}}\hat{\mathcal{P}}_3\partial_{\mathcal{Y}}G_1 - 2\left(\frac{\partial_{\mathcal{Y}}\overline{\mathcal{U}}_0}{\overline{\mathcal{U}}_0 - c}\right)\partial_{\mathcal{Y}}G_1 = \\
&\qquad \partial_z(\hat{\mathcal{P}}_3 F_0)\partial_z\tilde{\xi} + \partial_z(\hat{\mathcal{P}}_3 F_0\partial_z\tilde{\xi}) - 2\left(\frac{\partial_z\overline{\mathcal{U}}_0}{\overline{\mathcal{U}}_0 - c}\right)\hat{\mathcal{P}}_3\partial_z\tilde{\xi}F_0. \qquad \text{(D.19)}
\end{aligned}$$

Considering (D.18), the Fredholm Alternative theorem requires

$$\begin{aligned}
0 = (\mathcal{L}F_1, \Phi^\dagger) &= \int_{0^+}^{\infty}\left(\hat{\mathcal{P}}_3\partial_{\mathcal{Y}}^2 F_1 + 2\partial_{\mathcal{Y}}\hat{\mathcal{P}}_3\partial_{\mathcal{Y}}F_1 - 2\frac{\partial_{\mathcal{Y}}\overline{\mathcal{U}}_0}{\overline{\mathcal{U}}_0 - c}\partial_{\mathcal{Y}}F_1\right)\Phi^{\dagger *}d\mathcal{Y} \\
&= \int_{0^+}^{\infty}\partial_{\mathcal{Y}}\left(\partial_{\mathcal{Y}}\left[\frac{\Phi^{\dagger *}(\overline{\mathcal{U}}_0 - c)^2}{\hat{\mathcal{P}}_3}\right]\frac{\hat{\mathcal{P}}_3^2}{(\overline{\mathcal{U}}_0 - c)^2}\right)F_1 d\mathcal{Y},
\end{aligned} \qquad \text{(D.20)}$$

where here, the linear operator $\mathcal{L} = \hat{\mathcal{P}}_3\partial_{\mathcal{Y}}^2 + 2\partial_{\mathcal{Y}}\hat{\mathcal{P}}_3\partial_{\mathcal{Y}} - 2\frac{\partial_{\mathcal{Y}}\overline{\mathcal{U}}_0}{\overline{\mathcal{U}}_0 - c}\partial_{\mathcal{Y}}$. $\Phi^\dagger$ is the adjoint eigenfunction, i.e. satisfying $\mathcal{L}^\dagger\Phi^\dagger = 0$, where the adjoint linear operator

$$\begin{aligned}
\mathcal{L}^\dagger =&(\overline{\mathcal{U}}_0 - c)\partial_{\mathcal{Y}}^2 + \left[\partial_{\mathcal{Y}}\left(\frac{(\overline{\mathcal{U}}_0 - c)^2}{\hat{\mathcal{P}}_3}\right)\frac{\hat{\mathcal{P}}_3}{(\overline{\mathcal{U}}_0 - c)} + \partial_{\mathcal{Y}}\overline{\mathcal{U}}_0 + (\overline{\mathcal{U}}_0 - c)\right]\partial_{\mathcal{Y}} \\
&+ \left[\partial_{\mathcal{Y}}\left(\frac{\hat{\mathcal{P}}_3}{(\overline{\mathcal{U}}_0 - c)}\partial_{\mathcal{Y}}\left(\frac{(\overline{\mathcal{U}}_0 - c)^2}{\hat{\mathcal{P}}_3}\right)\right) + \partial_{\mathcal{Y}}\left(\frac{(\overline{\mathcal{U}}_0 - c)^2}{\hat{\mathcal{P}}_3}\right)\partial_{\mathcal{Y}}\left(\frac{\hat{\mathcal{P}}_3}{(\overline{\mathcal{U}}_0 - c)}\right)\right].
\end{aligned} \qquad \text{(D.21)}$$

More compactly, for $\mathcal{L}^\dagger\Phi^\dagger = 0$,

$$\partial_{\mathcal{Y}}\left[\frac{\Phi^{\dagger *}(\overline{\mathcal{U}}_0 - c)^2}{\hat{\mathcal{P}}_3}\right]\frac{\hat{\mathcal{P}}_3^2}{(\overline{\mathcal{U}}_0 - c)^2} = 0, \qquad \text{(D.22)}$$

which has the solution $\Phi^\dagger = \frac{\hat{\mathcal{P}}_3}{(\overline{\mathcal{U}}_0 - c)^2}$. We next enforce $(\mathcal{L}f, \Phi^\dagger) = 0$, using (D.18):

$$⨍_{-\infty}^{\infty} \left[\partial_z(\hat{\mathcal{P}}_3 G_0)\tilde{\xi}\partial_z\tilde{\xi} + \partial_z(\hat{\mathcal{P}}_3 G_0 \tilde{\xi}\partial_z\tilde{\xi}) - 2\left(\frac{\partial_z \overline{\mathcal{U}}_0}{\overline{\mathcal{U}}_0 - c}\right)\hat{\mathcal{P}}_3 G_0 \tilde{\xi}\partial_z\tilde{\xi} \right] \Phi^{\dagger *} d\mathcal{Y} = 0. \tag{D.23}$$

However, $\hat{\mathcal{P}}_3$ is real, so $\Phi^{\dagger *} = \Phi^\dagger$. This condition can be simplified to

$$\partial_z\left(G_0(\tilde{\xi}\partial_z\tilde{\xi})^{1/2}\right) ⨍_{-\infty}^{\infty} \left(\frac{\hat{\mathcal{P}}_3}{\overline{\mathcal{U}}_0 - c}\right)^2 d\mathcal{Y} + G_0(\tilde{\xi}\partial_z\tilde{\xi})^{1/2} ⨍_{-\infty}^{\infty} \left(\frac{\hat{\mathcal{P}}_3}{\overline{\mathcal{U}}_0 - c}\right)\partial_z\left(\frac{\hat{\mathcal{P}}_3}{\overline{\mathcal{U}}_0 - c}\right) d\mathcal{Y} = 0. \tag{D.24}$$

Dividing through by $G_0(\tilde{\xi}\partial_z\tilde{\xi})^{1/2}$ then yields

$$\frac{\partial_z\left(G_0(\tilde{\xi}\partial_z\tilde{\xi})^{1/2}\right)}{G_0(\tilde{\xi}\partial_z\tilde{\xi})^{1/2}} ⨍_{-\infty}^{\infty} \left(\frac{\hat{\mathcal{P}}_3}{\overline{\mathcal{U}}_0 - c}\right)^2 d\mathcal{Y} + ⨍_{-\infty}^{\infty} \left(\frac{\hat{\mathcal{P}}_3}{\overline{\mathcal{U}}_0 - c}\right)\partial_z\left(\frac{\hat{\mathcal{P}}_3}{\overline{\mathcal{U}}_0 - c}\right) d\mathcal{Y} = 0. \tag{D.25}$$

We break up the integral such that

$$\begin{aligned} 0 = \lim_{y^*\to 0^+} \Bigg[& \frac{\partial_z\left(G_0(\tilde{\xi}\partial_z\tilde{\xi})^{1/2}\right)}{G_0(\tilde{\xi}\partial_z\tilde{\xi})^{1/2}} \Bigg(\int_{-\infty}^{-y^*} \left(\frac{\hat{\mathcal{P}}_3}{\overline{\mathcal{U}}_0 - c}\right)^2 d\mathcal{Y} + \int_{-y^*}^{y^*} \left(\frac{\hat{\mathcal{P}}_3}{\overline{\mathcal{U}}_0 - c}\right)^2 d\mathcal{Y} \\ & + \int_{y^*}^{\infty} \left(\frac{\hat{\mathcal{P}}_3}{\overline{\mathcal{U}}_0 - c}\right)^2 d\mathcal{Y} \Bigg) + \int_{-\infty}^{-y^*} \left(\frac{\hat{\mathcal{P}}_3}{\overline{\mathcal{U}}_0 - c}\right)\partial_z\left(\frac{\hat{\mathcal{P}}_3}{\overline{\mathcal{U}}_0 - c}\right) 2d\mathcal{Y} \\ & + \int_{-y^*}^{y^*} \left(\frac{\hat{\mathcal{P}}_3}{\overline{\mathcal{U}}_0 - c}\right)\partial_z\left(\frac{\hat{\mathcal{P}}_3}{\overline{\mathcal{U}}_0 - c}\right) d\mathcal{Y} + \int_{y^*}^{\infty} \left(\frac{\hat{\mathcal{P}}_3}{\overline{\mathcal{U}}_0 - c}\right)\partial_z\left(\frac{\hat{\mathcal{P}}_3}{\overline{\mathcal{U}}_0 - c}\right) d\mathcal{Y} \Bigg]. \end{aligned} \tag{D.26}$$

Asymptotically, (D.26) is dominated by the integrals centered on the CL, so the leading order equation becomes

$$0 = \lim_{y^*\to 0^+} \left[\frac{\partial_z\left(G_0(\tilde{\xi}\partial_z\tilde{\xi})^{1/2}\right)}{G_0(\tilde{\xi}\partial_z\tilde{\xi})^{1/2}} \int_{-y^*}^{y^*} \left(\frac{\hat{\mathcal{P}}_3}{\overline{\mathcal{U}}_0 - c}\right)^2 d\mathcal{Y} + \int_{-y^*}^{y^*} \frac{\hat{\mathcal{P}}_3}{\overline{\mathcal{U}}_0 - c}\partial_z\left(\frac{\hat{\mathcal{P}}_3}{\overline{\mathcal{U}}_0 - c}\right) d\mathcal{Y} \right]. \tag{D.27}$$

In section 2.4, it is shown that, within the critical layer, $\hat{\mathcal{P}}_3 = \hat{\mathcal{P}}_3(z)$ and $(\overline{\mathcal{U}}_0 - c) = \tilde{\lambda}\mathcal{Y}$. Substituting these results into (D.27) and factoring yields

$$0 = \lim_{y^*\to 0^+} \left[\frac{\partial_z\left(G_0(\tilde{\xi}\partial_z\tilde{\xi})^{1/2}\right)}{G_0(\tilde{\xi}\partial_z\tilde{\xi})^{1/2}} \left(\frac{\hat{\mathcal{P}}_3}{\tilde{\lambda}}\right)^2 \Bigg|_{\mathcal{Y}=0} \int_{-y^*}^{y^*} \frac{1}{\mathcal{Y}^2} d\mathcal{Y} + \frac{\hat{\mathcal{P}}_3}{\tilde{\lambda}}\partial_z\left(\frac{\hat{\mathcal{P}}_3}{\tilde{\lambda}}\right)\Bigg|_{\mathcal{Y}=0} \int_{-y^*}^{y^*} \left(\frac{1}{\mathcal{Y}^2}\right)^2 d\mathcal{Y} \right]. \tag{D.28}$$

The integral can now be factored out so the equation becomes

$$0 = \left(\frac{\partial_z\left(G_0(\tilde{\xi}\partial_z\tilde{\xi})^{1/2}\right)}{G_0(\tilde{\xi}\partial_z\tilde{\xi})^{1/2}} \frac{\hat{\mathcal{P}}_3}{\tilde{\lambda}}\Bigg|_{\mathcal{Y}=0} + \partial_z\left(\frac{\hat{\mathcal{P}}_3}{\tilde{\lambda}}\right)\Bigg|_{\mathcal{Y}=0} \right) \lim_{y^*\to 0} \left[\int_{-y^*}^{y^*} \left(\frac{1}{\mathcal{Y}^2}\right)^2 d\mathcal{Y} \right]. \tag{D.29}$$

Consequently, the term in parentheses must vanish, enabling G_0 to be determined:

$$\begin{aligned}
\frac{\partial_z\left(G_0(\tilde{\xi}\partial_z\tilde{\xi})^{1/2}\right)}{G_0(\tilde{\xi}\partial_z\tilde{\xi})^{1/2}} &= -\frac{\partial_z\left(\frac{\hat{\mathcal{P}}_3}{\tilde{\lambda}}\right)}{\frac{\hat{\mathcal{P}}_3}{\tilde{\lambda}}}\bigg|_{\mathcal{Y}=0}; \\
\ln\left(G_0(\tilde{\xi}\partial_z\tilde{\xi})^{1/2}\right) &= -\ln\left(\frac{\hat{\mathcal{P}}_3|_{\mathcal{Y}=0}}{\tilde{\lambda}}\right) + \text{constant}; \\
G_0(\tilde{\xi}\partial_z\tilde{\xi})^{1/2} &= \gamma_g\frac{\tilde{\lambda}}{\hat{\mathcal{P}}_3|_{\mathcal{Y}=0}}.
\end{aligned} \tag{D.30}$$

A similar procedure can be used to determine F_0. Collecting results, we find

$$\begin{aligned}
F_0(z) &= \frac{\gamma_f\tilde{\lambda}}{\hat{\mathcal{P}}_3|_{\mathcal{Y}=0}(\partial_z\tilde{\xi})^{1/2}}, \\
G_0(z) &= \frac{\gamma_g\tilde{\lambda}}{\hat{\mathcal{P}}_3|_{\mathcal{Y}=0}(\tilde{\xi}\partial_z\tilde{\xi})^{1/2}}.
\end{aligned} \tag{D.31}$$

Here, the coefficients γ_f and γ_g are constants of integration that are determinable by matching with the WKBJ solution away form the caustic. It can be shown that $(\tilde{k}^2 - \tilde{\alpha}^2)$ has a simple zero at $z = z_c$. Consequently, in the region where $(z - z_c)$ is small, $\tilde{\xi}$ scales like $-(z - z_c)$. To avoid singular growth near the caustic we choose $\gamma_g = 0$. Then the leading asymptotic expansion in the area where $\tilde{\xi}(z)/\tilde{\Delta}^{2/3} = O(1)$ is

$$\mathcal{P}' \sim \frac{\tilde{\Delta}^{17/6}\gamma_f\hat{\mathcal{P}}_3\tilde{\lambda}}{\hat{\mathcal{P}}_3|_{\mathcal{Y}=0}(\partial_z\tilde{\xi})^{1/2}}\text{Ai}\left(-\frac{\tilde{\xi}(z)}{\tilde{\Delta}^{2/3}}\right)e^{i(\tilde{\alpha}/\tilde{\Delta})(x-ct)} + c.c. \tag{D.32}$$

In the illuminated region away from the caustic, the Airy function can be replaced by its asymptotic expansion for large negative argument to give

$$\begin{aligned}
\mathcal{P}' \;\sim\; -i\frac{\tilde{\Delta}^3\gamma_f\hat{\mathcal{P}}_3\tilde{\lambda}}{2\sqrt{\pi}\hat{\mathcal{P}}_3|_{\mathcal{Y}=0}(\tilde{k}^2-\tilde{\alpha}^2)^{1/4}}&\left[e^{i\left(\frac{1}{\tilde{\Delta}}\int_z^0(\tilde{k}^2-\tilde{\alpha}^2)^{1/2}dz+\pi/4\right)} + e^{i\left(-\frac{1}{\tilde{\Delta}}\int_z^0(\tilde{k}^2-\tilde{\alpha}^2)^{1/2}dz+3\pi/4\right)}\right] \\
&\times\; e^{i(\tilde{\alpha}/\tilde{\Delta})(x-ct)} + c.c.
\end{aligned} \tag{D.33}$$

for $z < z_c$ and $z_c > 0$. This approximation shows that the 'incident' instability mode is reflected at the caustic. Moreover, the spanwise fluctuation velocity is suppressed at the caustic since the spanwise fluctuation pressure gradient is weak there relative to its magnitude in the illuminated region, enabling the incident Rayleigh mode to two-dimensionalize prior to being reflected. The reflected mode has the same amplitude as the incident mode but experiences a $\pi/2$ shift in relative phase upon entering the illuminated region. In contrast, for $z > z_c$ and $z_c > 0$, the asymptotic approximation of $\mathcal{P}'$ for $|\tilde{\xi}(z)/\tilde{\Delta}^{2/3}| \gg 1$ is

$$\mathcal{P}' \sim \frac{\tilde{\Delta}^3\gamma_f\hat{\mathcal{P}}_3\tilde{\lambda}}{2\sqrt{\pi}\hat{\mathcal{P}}_3|_{\mathcal{Y}=0}(\tilde{\alpha}^2-\tilde{k}^2)^{1/4}}e^{-\frac{1}{\tilde{\Delta}}\int_z^0(\tilde{\alpha}^2-\tilde{k}^2)^{1/2}dz}e^{i(\tilde{\alpha}/\tilde{\Delta})(x-ct)} + c.c., \tag{D.34}$$

which rapidly decays to zero in the shadow zone beyond the caustic. Analogous results hold for the caustic at $z = z_c$ and $z_c < 0$.

The caustics are asymptotically thin (relative to the scale of the rolls) but the amplitude of the instability mode is asymptotically large there relative to its value in the illuminated region. Accordingly, we next estimate the contributions to the energy-budget integral on the left-hand side of (2.134), which is used to compute $\bar{\Omega}_c$, made by the Rayleigh mode in the caustic regions. First, however, we must determine the jump in mean streamwise vorticity across the CL in the vicinity of the caustic.

Within the CL (at $y = 0$, say), the governing fluctuation spanwise momentum equation (2.94) reduces to

$$\overline{U}_1 \partial_x W_2' = -\partial_z P_3' + \bar{\Omega}_c \partial_Y^2 W_2'. \tag{D.35}$$

Near the caustic, the fluctuation spanwise pressure gradient is

$$\partial_z P_3' = \tilde{\Delta}^{17/6} \hat{P}_3 \Delta^{-2/3} \partial_z \tilde{\xi} F_0 \mathrm{Ai}' e^{i(\tilde{\alpha}/\tilde{\Delta})(x-ct)}, \tag{D.36}$$

using $\partial_z P \approx 0$. Consequently, the fluctuation spanwise pressure gradient is (relatively) weaker near the caustic, where $\tilde{\beta} \to 0$, and W' is not forced. In fact, near the caustic, the instability mode two-dimensionalizes in the non-rotated x–z plane, with both ∂_z and W' becoming weaker than in the illuminated region. Kinematically, this is plausible since the instability mode must two-dimensionalize at the caustic before reflecting into the illuminated region. Thus,

$$W' \sim \tilde{\Delta}^{13/6} \hat{W}_2 F_0 \mathrm{Ai}\, \mathrm{e}^{i\left[\alpha(x-ct)+\theta(z/\tilde{\Delta})\right]} + c.c. \tag{D.37}$$

By substituting this ansatz into (D.35) we find

$$\left(i\tilde{\alpha}\tilde{\lambda}Y\right) \hat{W}_2 F_0 \mathrm{Ai} = -\hat{\mathcal{P}}_3|_{\mathcal{Y}=0} \partial_z \tilde{\xi} F_0 \mathrm{Ai}' + \overline{\Omega}_c \partial_Y^2 \hat{W}_2 F_0 \mathrm{Ai}, \tag{D.38}$$

where the notation Ai' signifies an $O(1)$ derivative of Ai with respect to its complete argument. Rearranging then yields

$$\partial_Y^2 \hat{W}_2 F_0 - i\frac{\tilde{\alpha}\tilde{\lambda}}{\overline{\Omega}_c} Y \hat{W}_2 = \frac{\partial_z \tilde{\xi}}{\overline{\Omega}_c} \frac{\mathrm{Ai}'}{\mathrm{Ai}} \hat{\mathcal{P}}_3|_{\mathcal{Y}=0}. \tag{D.39}$$

The solution to (D.39) can be expressed as

$$\hat{W}_2 = -\overline{\Omega}_c^{-1/3} (\tilde{\alpha}\tilde{\lambda})^{-2/3} \left(\frac{\partial_z \tilde{\xi} \mathrm{Ai}'}{\mathrm{Ai}} \hat{P}_3|_{\mathcal{Y}=0} \right) \int_0^\infty e^{-i\left(\frac{\tilde{\alpha}\tilde{\lambda}}{\overline{\Omega}_c}\right)^{1/3} Y\varphi - \varphi^3/3} d\varphi. \tag{D.40}$$

To determine the jump in $x-$mean shear across the CL, note that

$$\overline{(W'W')} \sim \tilde{\Delta}^4 \overline{(W_2' W_2')} \sim 4\tilde{\Delta}^4 \tilde{\Delta}^{1/3} F_0^2 \hat{W}_2^+ \hat{W}_2^{+*} \mathrm{Ai}^2, \tag{D.41}$$

where the overbar here (i.e. in the neighborhood of the caustic) refers to an average in x. Substituting into (2.89) we obtain

$$\left[\partial_{\mathcal{Y}} \tilde{\mathcal{W}}_3\right]_-^+ = 4\tilde{\Delta}^{1/3} \overline{\Omega}_c^{-2} \int_{-\infty}^{\infty} \partial_z (F_0^2 \hat{W}_2 \hat{W}_2^* \mathrm{Ai}^2) dY. \tag{D.42}$$

Next, substituting for $\hat{W}_2$ gives

$$\begin{aligned} \left[\partial_{\mathcal{Y}} \tilde{\mathcal{W}}_3\right]_-^+ = 4\tilde{\Delta}^{1/3} \overline{\Omega}_c^{-2} \int_{-\infty}^{\infty} \partial_z \Bigg(& \overline{\Omega}_c^{-2/3} F_0^2 (\tilde{\alpha}\tilde{\lambda})^{-4/3} \mathrm{Ai}'^2 \left| \hat{\mathcal{P}}_3|_{\mathcal{Y}=0} \right|^2 \partial_z \tilde{\xi}^2 \\ & \int_0^\infty e^{-i\left(\frac{(\tilde{\alpha}\tilde{\lambda})}{\overline{\Omega}_c}\right)^{1/3} Y\varphi - \varphi^3/3} d\varphi \int_0^\infty e^{i\left(\frac{(\tilde{\alpha}\tilde{\lambda})}{\overline{\Omega}_c}\right)^{1/3} Y\varphi - \varphi^3/3} d\varphi \Bigg) dY. \end{aligned} \tag{D.43}$$

Defining $\hat{Y} = \left(\frac{(\tilde{\alpha}\tilde{\lambda})}{\overline{\Omega}_c}\right)^{1/3} Y$ and recalling $F_0 = \frac{\gamma_f \tilde{\lambda}}{\sqrt{\partial_z \tilde{\xi} \hat{\mathcal{P}}_3|_{\mathcal{Y}=0}}}$,

$$\begin{aligned}\left[\partial_{\mathcal{Y}}\tilde{\mathcal{W}}_3\right]_-^+ &= 4\frac{\tilde{\Delta}^{1/3}\gamma_f^2}{\overline{\Omega}_c^2}\int_{-\infty}^{\infty}\partial_z\left(\overline{\Omega}_c^{-1/3}(\tilde{\alpha}\tilde{\lambda})^{-5/3}\partial_z\tilde{\xi}\,\mathrm{Ai}'^2\tilde{\lambda}^2\int_0^{\infty}e^{-i\hat{Y}\varphi-\varphi^3/3}d\varphi\int_0^{\infty}e^{i\hat{Y}\varphi-\varphi^3/3}d\varphi\right)d\hat{Y}\\ &= 4\frac{\tilde{\Delta}^{1/3}\gamma_f^2}{\overline{\Omega}_c^{7/3}\tilde{\alpha}^{5/3}}\partial_z\left(\partial_z\tilde{\xi}\,\mathrm{Ai}'^2\tilde{\lambda}^{1/3}\int_{-\infty}^{\infty}\left[\int_0^{\infty}e^{-i\hat{Y}\varphi-\varphi^3/3}d\varphi\int_0^{\infty}e^{i\hat{Y}\varphi-\varphi^3/3}d\varphi\right]d\hat{Y}\right).\end{aligned} \tag{D.44}$$

To simplify this result, we exploit the fact that if arbitrary functions f and g are integrable functions then the integral of their convolution on the whole space is simply obtained as the product of their integrals; see appendix E. Thus,

$$\begin{aligned}\left[\partial_{\mathcal{Y}}\tilde{\mathcal{W}}_3\right]_-^+ &= 4\frac{\tilde{\Delta}^{1/3}\gamma_f^2}{\overline{\Omega}_c^{7/3}\tilde{\alpha}^{5/3}}\partial_z\left(\partial_z\tilde{\xi}\,\mathrm{Ai}'^2\tilde{\lambda}^{1/3}\int_{-\infty}^{\infty}\left[\int_0^{\infty}\frac{\sqrt{\pi}}{\sqrt{\varphi}}e^{-\frac{\hat{Y}^2}{\varphi}-\varphi^3/12}d\varphi\right]d\hat{Y}\right)\\ &= 4\frac{\tilde{\Delta}^{1/3}\gamma_f^2\pi}{\overline{\Omega}_c^{7/3}\tilde{\alpha}^{5/3}}\partial_z\left(\partial_z\tilde{\xi}\,\mathrm{Ai}'^2\tilde{\lambda}^{1/3}\int_0^{\infty}\left[e^{-\varphi^3/12}\int_{-\infty}^{\infty}\frac{1}{\sqrt{\pi\varphi}}e^{-\frac{\hat{Y}^2}{\varphi}}d\hat{Y}\right]d\varphi\right).\end{aligned} \tag{D.45}$$

Recognizing that the $\hat{Y}$ integral inside the brackets is an error function, (D.45) can be further simplified:

$$\left[\partial_{\mathcal{Y}}\tilde{\mathcal{W}}_3\right]_-^+ = 4\frac{\tilde{\Delta}^{1/3}\gamma_f^2\pi}{\overline{\Omega}_c^{7/3}\tilde{\alpha}^{5/3}}\partial_z\left(\partial_z\tilde{\xi}\,\mathrm{Ai}'^2\tilde{\lambda}^{1/3}\int_0^{\infty}e^{-\varphi^3/12}d\varphi\right). \tag{D.46}$$

The remaining integral can be evaluated analytically in terms of gamma functions. The mean stress jump across the CL near the caustic is therefore given by

$$\left[\partial_{\mathcal{Y}}\tilde{\mathcal{W}}_3\right]_-^+ = 4\frac{\tilde{\Delta}^{1/3}\gamma_f^2\pi\left(\frac{2}{3}\right)^{2/3}\Gamma\left(\frac{1}{3}\right)}{\overline{\Omega}_c^{7/3}\tilde{\alpha}^{5/3}}\partial_z\left(\partial_z\tilde{\xi}\,\mathrm{Ai}'^2\tilde{\lambda}^{1/3}\right). \tag{D.47}$$

Finally, for brevity of notation, let $n_0 = 2\pi(2/3)^{2/3}\Gamma(1/3)$. Equation (D.47) then reduces to

$$[\partial_{\mathcal{Y}}\tilde{\mathcal{W}}_3]_-^+ = \tilde{\Delta}^{1/3}\frac{2n_0\gamma_f^2}{\bar{\Omega}_c^{7/3}\tilde{\alpha}^{5/3}}\partial_z\left(\tilde{\lambda}^{1/3}\partial_z\tilde{\xi}\,\mathrm{Ai}'^2\right). \tag{D.48}$$

To isolate the various contributions, the integral in (2.134), we split the integral into three parts:

$$\begin{aligned}\int_0^{L_z/2}\tilde{w}_2|_{y=0}\partial_{\mathcal{Y}}\tilde{\mathcal{W}}_3|_{\mathcal{Y}=0^+}dz &= \int_0^{z_c^-}\tilde{w}_2|_{y=0}\partial_{\mathcal{Y}}\tilde{\mathcal{W}}_3|_{\mathcal{Y}=0^+}dz + \int_{z_c^-}^{z_c^+}\tilde{w}_2|_{y=0}\partial_{\mathcal{Y}}\tilde{\mathcal{W}}_3|_{\mathcal{Y}=0^+}dz\\ &+ \int_{z_c^+}^{L_z/2}\tilde{w}_2|_{y=0}\partial_{\mathcal{Y}}\tilde{\mathcal{W}}_3|_{\mathcal{Y}=0^+}dz.\end{aligned} \tag{D.49}$$

The amplitude $A(z)$ in the shadow region is exponentially small, so the integral from z_c^+ to $L_z/2$ vanishes.

Upon using (D.48) to evaluate the second integral on the right-hand side of (D.49), we note that the z derivative is large, $O(\tilde{\Delta}^{-2/3})$, since the argument of Ai is $\tilde{\Delta}^{-2/3}\tilde{\xi}(z)$. (In contrast, the notation Ai$'$ signifies an $O(1)$ derivative of Ai with respect to its complete argument.) This amplification, however, is offset by the small [i.e. $O(\tilde{\Delta}^{2/3})$] integration range. Consequently, the second integral in (D.49) is asymptotically smaller than the first owing to the $\tilde{\Delta}^{1/3}$ factor in (D.48).

APPENDIX E

CONVOLUTION

This appendix shows how to take the convolution needed for the derivation of the stress jump across the critical layer. To calculate the convolution, we begin with

$$\int_{-\infty}^{\infty} e^{-\frac{\psi^3}{3}+i\hat{Y}\psi}d\psi \int_{-\infty}^{\infty} e^{-\frac{\varphi^3}{3}-i\hat{Y}\varphi}d\varphi.$$

By definition, this equivalent to

$$\int_{-\infty}^{\infty}\left[\int_{-\infty}^{\infty} e^{-\frac{\psi^3}{3}-i\hat{Y}\psi}e^{-\frac{(\varphi-\psi)^3}{3}-i\hat{Y}(\varphi-\psi)}d\psi\right]d\varphi.$$

Factoring out φ from integral and expanding the cubic polynomial yields

$$\int_{-\infty}^{\infty}\left[e^{-\frac{\varphi^3}{3}+i\hat{Y}\varphi}\int_{-\infty}^{\infty} e^{\varphi^2 t-\varphi\psi^2-2i\hat{Y}\psi}d\psi\right]d\varphi.$$

Completing the square and again factoring out φ terms gives

$$\int_{-\infty}^{\infty}\left[e^{-\frac{\varphi^3}{3}+i\hat{Y}\varphi}e^{\frac{(\varphi^2-2i\hat{Y})^2}{4\varphi}}\int_{-\infty}^{\infty} e^{-(\sqrt{\varphi}\psi-\frac{\varphi^2\psi-2i\hat{Y}\psi}{2\sqrt{\varphi}})^2}d\psi\right]d\varphi.$$

Finally, integrating and expanding the remaining exponential yields

$$\int_{-\infty}^{\infty}\left[e^{-\frac{\varphi^3}{3}+i\hat{Y}\varphi}e^{\frac{\varphi^3}{4}-i\hat{Y}\varphi-\frac{\hat{Y}^2}{\varphi}}\frac{2\sqrt{\pi}}{\sqrt{\varphi}}\right]d\varphi,$$

which simplifies to

$$\int_{-\infty}^{\infty}\frac{2\sqrt{\pi}}{\sqrt{\varphi}}e^{-\frac{\varphi^3}{12}-\frac{\hat{Y}^2}{\varphi}}d\varphi.$$

APPENDIX F

ECS SOLUTION ALGORITHM

To compute the ECS, the following algorithm is employed.

1. The renormalized roll velocity field ($\tilde{v}_2(y,z)$,$\tilde{w}_2(y,z)$) is obtained by dividing (2.11)–(2.12) by the (as yet) unknown $\bar{\Omega}_c$.

2. $\overline{u}_0(y,z)$ is obtained by numerically solving (2.19) using a Fourier–Chebyshev pseudospectral scheme on the domain $0 \leq y \leq 1$, $-L_z/2 \leq z \leq L_z/2$ subject to the symmetry conditions $\overline{u}_0(0,z) = 0$ and $\overline{u}(1,z) = 1$ and periodic boundary conditions in z.

3. The fluctuation fields within the VF are obtained by collapsing (2.42)–(2.44) into Rayleigh's equation and then numerically solving the resulting 1D differential eigenvalue problem (treating the total horizontal wavenumber $k(z)$ as the eigenvalue) on the domain $-\infty < \mathcal{Y} < \infty$ using a Chebyshev collocation method, with a $\mathcal{Y}$-coordinate mapping, for a discrete set of z ranging from $-L_z/2$ to $L_z/2$.

4. The coefficients a_z and a_0 in the amplitude equation (2.77) are obtained by numerical quadrature using the expressions given in (2.75)–(2.76), and the fluctuation amplitude function $A(z)$ is then obtained from (2.78).

5. The homogenized roll vorticity $\bar{\Omega}_c$ is computed via numerical quadrature using (2.137).

6. Transformations (2.46) are utilized to obtain the fluctuation fields in the original (i.e. non-rotated) coordinates.

Note that the fluctuation fields within the CL need not be evaluated, but if desired, they can be reconstructed using (2.98) and (2.91)–(2.92).

APPENDIX G

TABLE OF ACRONYMS

This appendix includes a list of acronyms used in the dissertation.

UNH - University of New Hampshire

FPF - Flow Physics Facility

LSM - Large Scale Motions

VLSM - Very Large Scale Motions

POD - Proper Orthogonal Decomposition

MI - Mean Inertia

TI - Turbulent Inertia

MV - Mean Viscous Force

PG - Pressure Gradient

MMB - Mean Momentum Balance

2D - Two-Dimensional

3D - Three-Dimensional

NS - Navier Stokes

TBL - Turbulent Boundary Layer

UMZ - Uniform Momentum Zone

VF - Vortical Fissure

CL - Critical Layer

VWI - Vortex-Wave Interaction

SSP - Self-Sustaining Process

ECS - Exact Coherent States

DNS- Direct Numeric Simulations

WKBJ - Wentzel-Kramers-Brillouin-Jeffreys

E.S.T. - Exponentially Small Terms

H.O.T. - Higher Order Terms

c.c. - Complex Conjugate